COMPUTATIONAL FLUID DYNAMICS MODEL OF TWO-PHASE HEAVY OIL AND AIR FLOW IN A HORIZONTAL PIPE

By

Nicholas E. Sanders

A Project Submitted in Partial Fulfilment of the Requirements

For the Degree of

Master of Science

in

Petroleum Engineering

University of Alaska Fairbanks

May 2020

APPROVED:

Dr. Mohabbat Ahmadi, Committee Chair

Dr. Obadara Awoleke, Committee Co-Chair

Dr. Abhijit Dandekar, Chair

Department of Petroleum Engineering

ABSTRACT

The production of heavy oil resources is becoming more prevalent as the conventional resources of the world continue to deplete. These heavy oil resources are being produced from horizontal wells and need to be transported in pipeline to processing facilities as a two-phase flow. Two-phase flow is important to the oil industry with the general focus being placed on light oil or water and gas flows. With little work having been done on two-phase heavy oil flow this study will examine these two-phase flows by recreating experimental data generated for heavy oil and air flow in a 1.5-inch diameter pipe and expand this data to include larger 2.875-inch and 3.5-inch pipes.

A computational fluid dynamics model was generated to mimic the 1.5-inch diameter pipe used in the experiments. This model was validated for laminar and turbulent flow by using the same heavy oil properties from the original experiment and air respectively. The model was then run to simulate the given two-phase oil-air flows provided from the experimental data for the flow velocities that had pressure drop and liquid holdup data available. The two-phase results were compared to both the experimental data and the Beggs and Brill values for both pressure drop and liquid holdup. A 2.875-inch and 3.5-inch model were generated and the same process was followed for laminar and turbulent validation and then with a subset of four two-phase flow velocities. Without the availability of experimental data for the two larger size pipes the two-phase results were only compared to the Beggs and Brill values.

Overall the results showed a good correlation to the laminar and turbulent flow in all three models with the turbulent flow showing the largest error for the pressure drop when the flow was in the laminar to turbulent transition zone for Reynolds numbers. The two-phase results showed to be in between the experimental and Beggs and Brill method values for the original 1.5-inch model and showed that as the gas flow velocity increased in the system the error grew for all three models. Given that the Beggs and Brill method values were generated based on experiments for water-air flow in a 1.0-inch pipe the values for the pressure drop in the 2.875-inch pipe and the 3.5-inch pipe were not unexpected and seemed to match well with an extrapolation of the experimental values.

This study shows that a model can be generated to examine the two-phase flow behavior in horizontal sections of well and in pipelines on a computational basis. While these models are time consuming to generate and run with the increase in computing capacity available easily they can become more suitable than generating experimental setups for finding the same information. There will need to be more work done on heavy oil two-phase flow and additional experiments run for larger size pipes and two-phase flow to help tune these models but they do show promise for the future.

TABLE OF CONTENTS

LIST OF FIGURES

LIST OF TABLES

ACKNOWLEDGEMENTS

I would like to thank Dr. Mohabbat Ahmadi for his guidance through the many years it took me to accomplish completing my degree and never giving up on me when this project provided its many frustrations. I am grateful to Dr. Obadara Awoleke for his pointing me in the direction of this work and his teaching on two-phase flow. Thank you Dr. Abhijit Dandekar for his guidance through the graduate school process and for the many different classes I was able to take from him

A Very special thank you to my wife Leah Glasscock-Sanders for all of her support throughout the long years of me working toward my degree. Without you I would never have made it to the end.

I would like to thank my employer, Halliburton Energy Services, for their financial support in the form of tuition reimbursement and for the use of their computers for the initial modeling runs.

This work was supported in part by the high-performance computing and data storage resources operated by the Research Computing Systems Group at the University of Alaska Fairbanks Geophysical Institute.

1 CHAPTER ONE: INTRODUCTION

1.1 Overview

Heavy oil and bitumen is estimated to make up 70% of the oil resources in the world, with heavy oil being defined as any oil less than 22° API (Meyer and Attanasi 2003). As the conventional resources start to deplete around the world these heavy oils will need to start being produced in order to keep up with demand. Figure 1.1 shows the location of the world's heavy oil resources along with a little bit of history of the production of heavy oil.

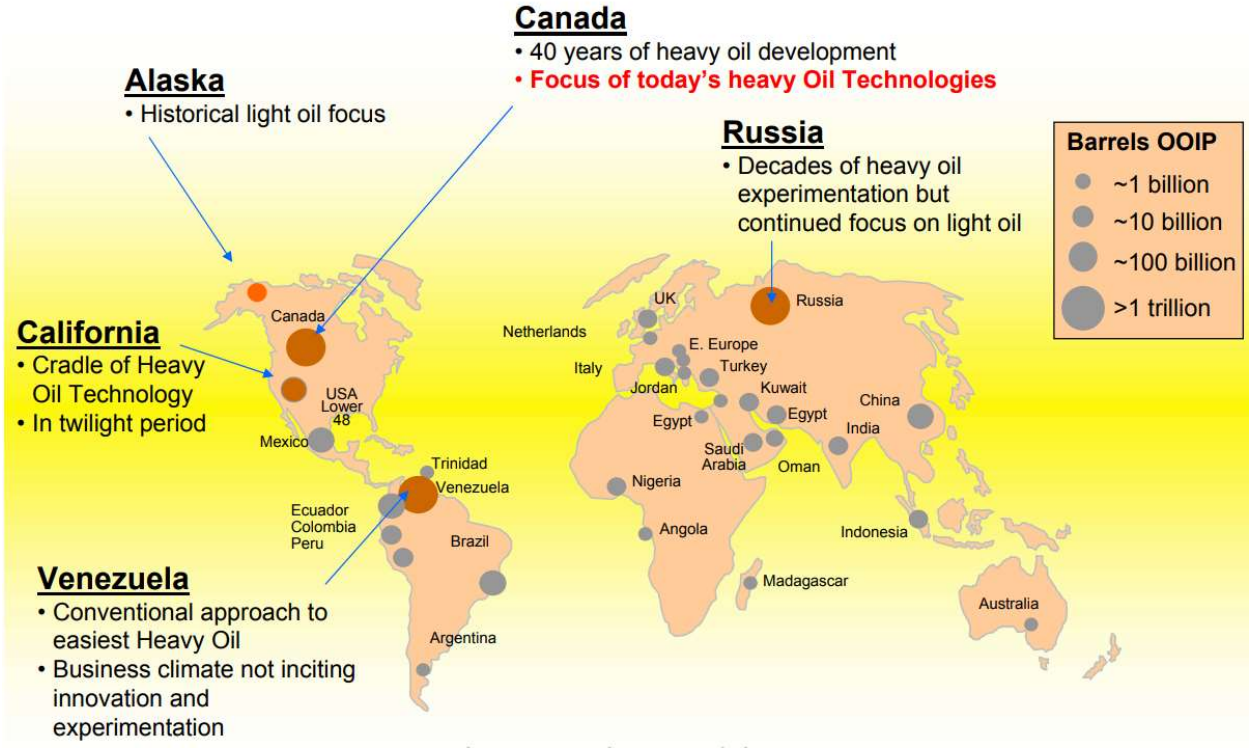

Figure 1.1 World heavy oil resources (BP-Alaska 2011)

California has historically had a large amount of their total oil production coming from heavy oil resources and has pioneered numerous ways to extract its heavy oil, mostly by using steam. The Canadians have started to produce heavy oil and bitumen over the last decade since only 2.5% of their total reserves are in conventional reservoirs. In 2018 the oil sands, Canada's unconventional resources, accounted for 64% of their total oil production with 19% coming from mining of bitumen and 81% coming from in situ methods (Canada 2019). These in situ methods include steam assisted gravity drainage (SAGD) where two horizontal wells are drilled in close proximity to each other. One well is used to inject steam into the formation at a higher point in the reservoir while the other well is used to produce the resulting oil from a lower point in the reservoir. This steam injection causes the oil in the formation to warm up and becomes more mobile, allowing it to flow downward in the reservoir to the producing well.

In Alaska the heavy oils on the North Slope have been produced from vertical wells for several decades. New multilateral wells have been drilled and electrical submersible pumps have been used to produce the heavy oil in the West Sak reservoir. A recent trial at the Milne Point field for the cold heavy oil

production with sand (CHOPS) process, showed promise in producing heavy oil, gas, and sand from the reservoir to allow for higher recovery.

Studies related to multi-phase flow in pipes have been performed for over a century. The experimental measurements have mostly consisted of flow loops to observe the pressure drop, liquid holdup, and flow pattern. These studies typically use water and air phases and rely on a small diameter pipe for the experiments. Recently with the development of higher speed computers and computer clusters, numerical modeling has become more prevalent and allows for computer simulations of all aspects of fluid dynamics including two-phase flow studies. These computational fluid dynamics (CFD) models are typically used for air flow over airplanes or cars to examine the aerodynamic properties of the object being studied but have also been used for studies on boats through water, water flow in channels and pipes, and two-phase flow in pipes for nuclear reactors and the oil industry. These two-phase studies in the oil industry have been for air-water systems or for light oil-gas systems.

1.2 Objective

This work studies the two-phase heavy oil-air flow inside a horizontal pipe using numerical CFD techniques. With unconventional resources becoming more prevalent due to the declining production of conventional resources, heavy oils are being produced on a larger scale. These heavy oils are being produced from horizontal laterals drilled in new and existing wells to maximize the production from one wellhead. In some situations, in situ gas is produced with the oil and disassociated as the pressure from the reservoir starts to dissipate. Previous heavy oil studies related to multi-phase in the pipe have been mostly experimental. This study will move those experimental setups into a computer simulation by:

1. Build a three dimensional numerical model of two-phase heavy oil-air flow inside a 1.5-inch diameter pipe based on the experimental work performed by Hulsurkar (2017)
2. Validate the numerical model for both laminar and turbulent flows to show that the CFD software is generating correct results
3. Calculate pressure drop and liquid holdup values using CFD models and compare them to the experimental work and predicted values from mechanistic models
4. Expanding the experimental 1.5-inch model to larger pipe sizes of 2.875-inch and 3.5-inch and compare to Beggs and Brill method pressure drop and liquid holdup values

2 CHAPTER TWO: LITERATURE REVIEW

2.1 Heavy oil

Oil is typically characterized by its API gravity as given in Equation 2.1. The specific gravity of oil is the ratio of the density of the oil divided by density of water; therefore, as the oil gets heavier its density approaches the density of water. Equation 2.1 shows that as the oil specific gravity increases the API gravity decreases and a heavier oil will have a lower API gravity.

$$API\ gravity = \frac{141.5}{SG} - 131.5 \qquad 2.1$$

Figure 2.1 shows the relationship of the viscosity of dead oil as a function of temperature based on the work of Beal in 1945 (Beal 1945). Beal used 753 values for dead oil viscosity to develop the graph and showed that as the API gravity of the oil decreases, the viscosity of the oil increases. Viscosity is defined as the internal resistance of a fluid to flow so a higher number would indicate more resistance to flow. For this reason, heavier liquids will not flow as easy as a lighter liquid and this can be shown by examining the flow of motor oils where a heavier 30 weight motor oil will not flow as easily as a lighter 10 or even zero weight oil. The USGS defines light oil as having a API gravity of at least 22° and a viscosity of less than 100 centipoise, a heavy oil as having an API gravity of less than 22° and a viscosity of greater than 100 centipoise, and extra heavy oil as having an API gravity of less than 10° (Meyer and Attanasi 2003).

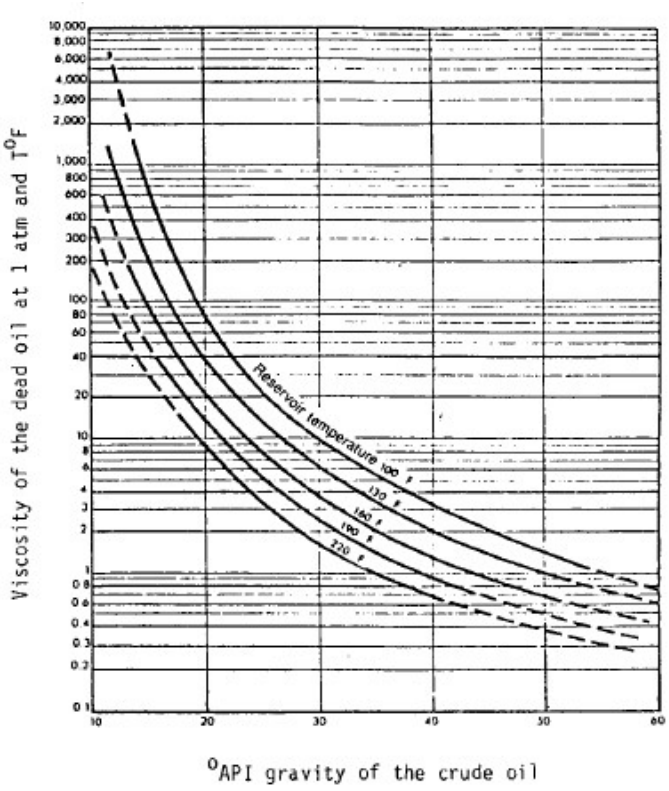

Figure 2.1 API gravity as a function of viscosity (Beal 1945)

In 2003 the USGS listed a total of 434 billion barrels of technically recoverable heavy oil in the world with 35.3 billion barrels of oil being in North America. This number is narrowed down further as 21 billion barrels located in Canada, with the remaining 14 billion barrels of it located in the United States, split as 7 billion on the North Slope of Alaska and 7 billion in the lower 48 states (Meyer and Attanasi 2003). These recoverable heavy oil resources numbers have since been revised to be higher as shown in Figure 2.2 (Bata et al. 2019). The heavy oil reserves in Alaska are spread across several larger fields that have been producing since the early 1990s with much success. These reserves are mainly produced from three larger fields, the Schrader Bluff, West Sak and Ugnu with their locations shown in Figure 2.2 (Bata et al. 2019).

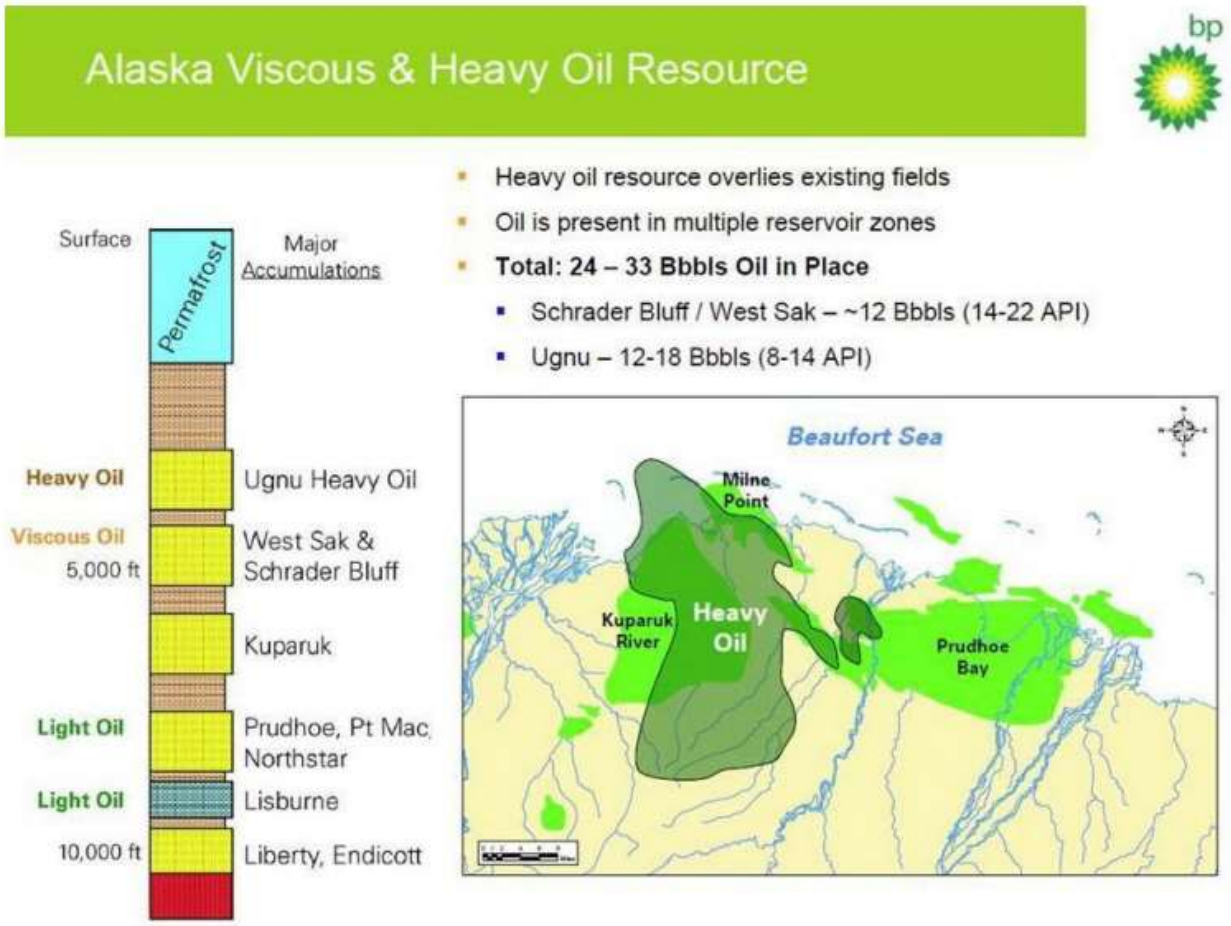

Figure 2.2 Distribution of Alaska heavy oil (Bata et al. 2019)

The Schrader Bluff and West Sak pool are a 14° – 22° API oil with a viscosity in the range of 50-5,000 centipoise whereas the Ugnu pool is an 8° - 14° API oil with a viscosity in the range of 1,000 to 1,000,0000 centipoise (Mathur et al. 2017; Bata et al. 2019). While the Schrader Bluff and West Sak oil pools have been producing since the early 1990s the Ugnu oil pool was not produced due to the heavier nature of the oil. In 2011 a pilot program was initiated in the Milne Point field to produce the oil from the Ugnu oil pool by a method known as Cold Heavy Oil Production with Sand (CHOPS). This CHOPS process allows the oil to be produced along with some of the sand from the formation and has been in use in Alberta and Saskatchewan Canada since the 1980s (Minish and Yule 2012). The wells are completed with larger perforations and no screens to keep the unconsolidated sand from entering the wellbore. This

movement of sand along with oil flow allows for better mobility of the viscous oil and over time will allow for a larger disturbed zone with a higher permeability around the wellbore (Desseault et al. 2000).

Like all live oils, these heavy oil reservoirs, with exception of surface oil mines, contain gas in solution and it has been shown in some CHOPS wells that this gas will disassociate from the oil in the reservoir. When the gas disassociates from the oil it will help to destabilize the sand and allow for better flow. Most of the CHOPS wells do not form this foamy oil phenomenon in the formation (Desseault et al. 2000). Regardless of if the gas is disassociated from the oil in the reservoir or not, there will be a multi-phase flow situation in the wellbore as the pressure drops and the oil is brought to surface. This three-phase flow would be made up of oil, gas, and sand with a possible fourth phase in water.

Hulsurkar (2017) worked on the flow of three phase heavy oil, gas, and sand in an experimental apparatus to monitor pressure gradients along a horizontal pipe, liquid holdup, and flow patterns. This work was carried out by allowing heavy oil and gas to flow through a 1.5-inch pipe at given flow velocities, the pressure drop was measured between the entrance of the pipe and the exit of the pipe as shown in Figure 2.3.

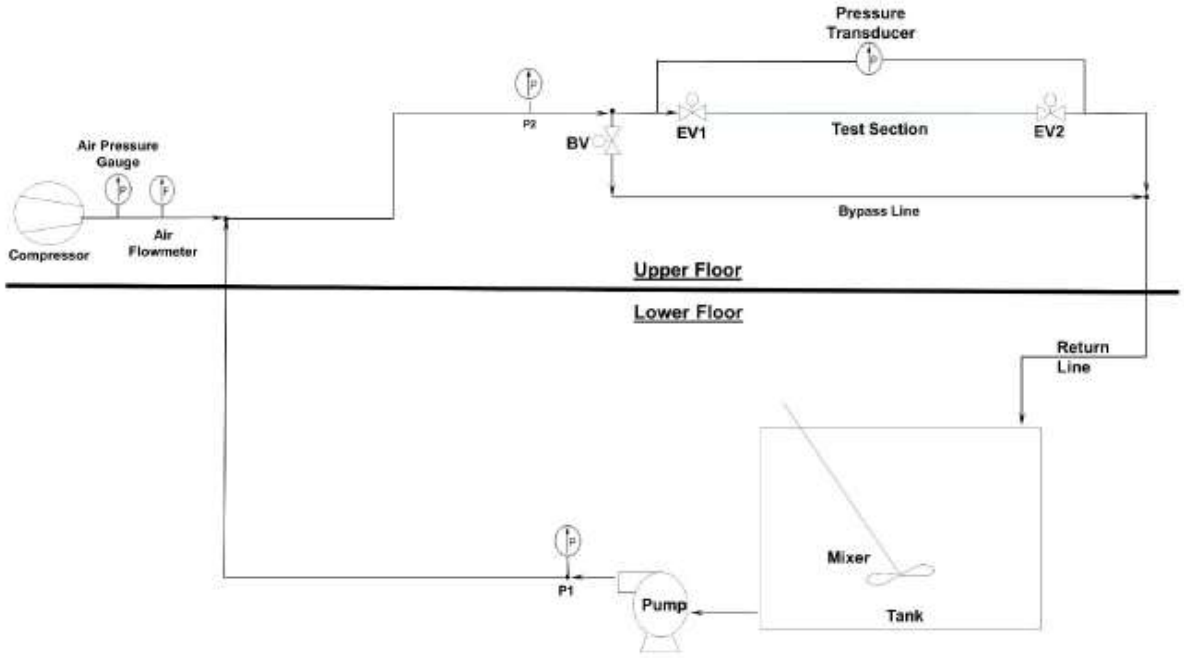

Figure 2.3 Experimental setup from Hulsurkar (2017)

Flow experiments were carried out with three different viscosity oils ranging from 149.8 to 217.5 centipoise. Pressure drop measurements were taken and different flow velocities for both the oil and the air. The measured pressure drop values were compared to both values from the Beggs and Brill correlation and values calculated by the PIPESIM software. The results from all three approaches showed that for the same flow velocity as the viscosity increased the pressure drop grew larger and as the fluid velocity/flowrate increased the pressure drop grew larger. The measured pressure gradients and liquid holdups were higher than both the Beggs and Brill and PIPESIM results. The PIPESIM software was used to generate a model that was identical to the experimental setup. This software was used to predict the pressure gradients using the Beggs and Brill Original method from 1973 and the Tulsa Unified Fluid Flow Model (TUFFP Unified) multiphase fluid flow models. Since the Beggs and Brill correlation is

based on water flowing in a 1-inch diameter pipe, this was not completely unexpected. The flow patterns matched up well with the predicted patterns.

A study was run and different sand volumes up to 3% were introduced to the fluid flow system and the pressure drop, liquid holdup, and flow patterns were measured. The study showed that as the sand volume increased the pressure drop along the pipe increased as well but not in a significant enough way to predict that it would allow for higher pressure gradients in all situations. The study also showed that a moving bed of sand can be expected at the bottom of the pipe for the range of flow velocities tested. The speed of the sand movement was not calculated. The flow patterns remained the same between the two-phase and three-phase flows but the flows that included sand did not show as sharp of edges on the elongated bubble flow and slug flows (Hulsurkar 2017).

2.2 CFD in the petroleum industry

Computational fluid dynamics CFD has found its way into the petroleum industry over the last decade in various different aspects. Longfellow and Green (2014) used CFD to model a plunger lift system in a horizontal well. Their work showed that the CFD model was within 8% for observed fall rates for plunger lift systems. They also examined different types of plungers to determine if one was more appropriate for a given application, as well as modeling some of the problems associated with plungers in horizontal wells including uneven wear and gas blow-by. The authors also showed that along with the positives, CFD encountered issues with working in unsteady multi-phased flow environments present in the horizontal tubing.

Zhou and Shah (2003) used CFD to model flow inside of coiled tubing. They modeled both Newtonian and non-Newtonian fluids inside coiled tubing. Largely concerned with the flow due to the curvature of the coil on the reel, the results compared well with previous theoretical and numerical studies. Newtonian fluids showed that in laminar flow the velocity profile in the curved tubing was more distinct than the parabolic one observed in straight tubing. In contrast the turbulent flow in curved tubing and straight tubing showed similar velocity profiles. The CFD modeling showed that as Reynolds numbers increased the secondary flow was confined to a thin boundary layer. The friction pressure from the turbulent Newtonian fluid experiments performed on coiled tubing reels agreed well with the CFD results.

Li et al. (2005) used CFD to model the flow characteristics around a subsurface safety valve (SSSV). SSSV's are used in a wellbore to close during an uncontrolled release of reservoir fluids to the surface. The pressure gradient across the valve will drop in an uncontrolled release and the valve will close due to this difference and seals off the wellbore below the surface. Li et al. (2005) were concerned with the possibility that high rate gas flow will prevent the SSSV from closure. The combination of CFD models and full scale physical tests has shown comparable results at different flow velocities and under different flow conditions for which the valve was designed to work.

CFD has been used not only to model flow around plunger lift systems or SSSV's but also has been used to model inflow performance from a wellbore. Byrne et al. (2009) compared how close CFD models were to actual inflow performance from laboratory studies on core samples. This was the first time that CFD was used to predict well performance based on high quality laboratory data. The authors combined laboratory testing with CFD methods to determine permeability for different zones including the undamaged reservoir, the invaded zone, and the mud cake. These models showed that impacts from formation damage were not significant for any of the muds tested. A reduction of the formation permeability by 95% was required to observe significant reduction in the flow velocity. This study has allowed for CFD to be used in the design of drilling systems during the well planning stages.

Jimenez and Chavez (2009) used CFD to model the inflow of single and multiple fractured wells in their study. They showed that CFD was a practical engineering tool that provided core information and enhances decision making processes for completions. They used CFD to simulate two different case studies, one a vertical well and the second, a deviated well. The first study showed a reservoir with five different layers of varying permeability.

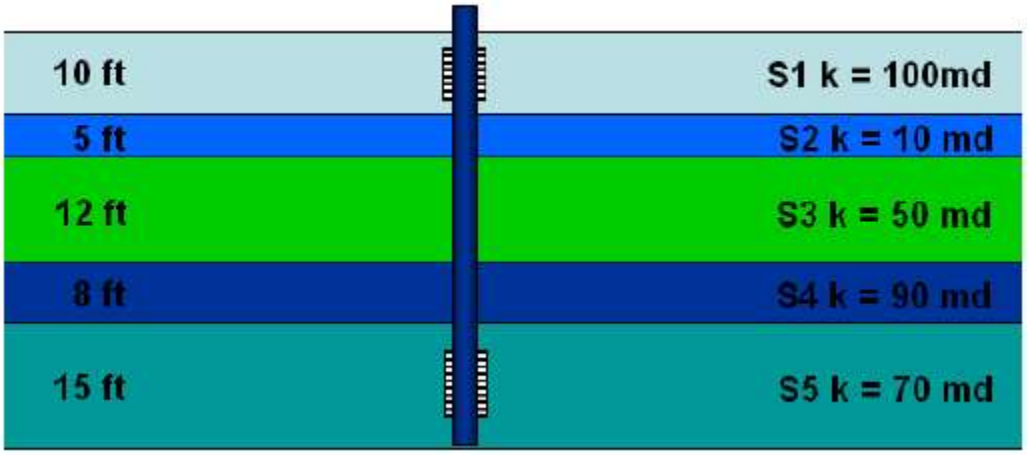

Figure 2.4 Vertical Well Setup (Jimenez and Chavez 2009)

The completion was planned in three stages. The middle layer, S3, was perforated as part of the first stage. After the first stage was allowed to produce the second stage was performed by fracturing the initial set of perforations in S3. The third stage was perforating the upper and lower layers S1 and S5, it was assumed that there was no interaction between the fractures and the perforation in intervals S1 and S5. This model showed that an incremental inflow capacity of greater than 60% was observed in the S3 zone when fractured as opposed to perforations.

The second model was a deviated well through the same reservoir setup as shown in Figure 2.5.

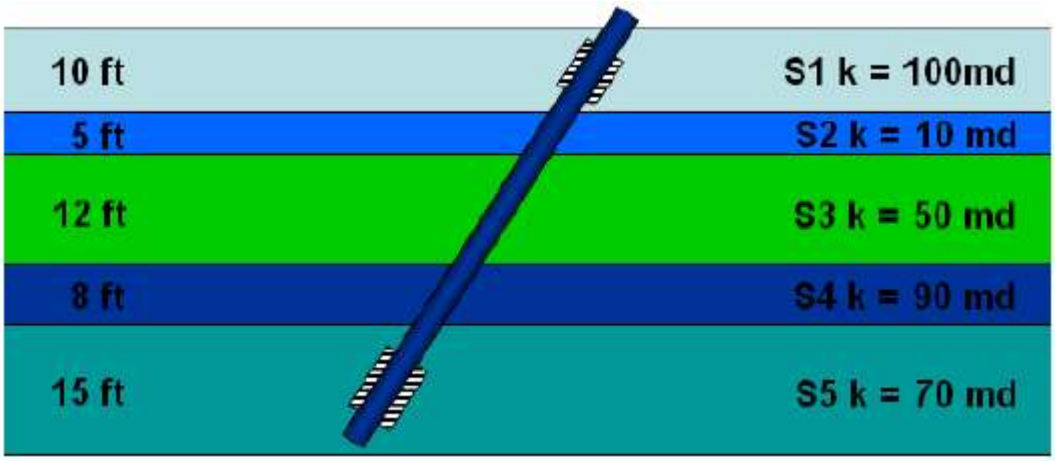

Figure 2.5 Deviated Well Setup (Jimenez and Chavez 2009)

This completion was done with similar steps to the vertical well model, perforating and fracturing S4, perforating and fracturing S2, and finally perforating S1 and S5 again the same as in the vertical model. This setup resulted in a reduction of production from the S3 layer over the same setup in the vertical

model. This model showed a 20% to 30% decrease in total production from the vertical model with a fracture in S3.

Byrne et al. (2010) using CFD examined fluid flow into a horizontal wellbore considering the invaded zone and mud cake. The first model studied the production from a horizontal well with formation damage due to invaded zone and a mud cake inside the wellbore. Different flowing pressures were assigned to different sectors along the well to better represent the drawdown from toe to heal as shown in Figure 2.6.

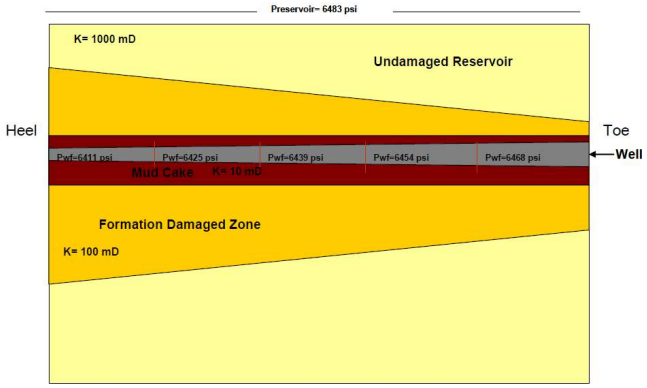

Figure 2.6 Setup for Case 1 (Byrne et al. 2010)

One of the benefits of the CFD modeling is that the velocity profiles can be examined in detail. By examining the velocity profile, this model showed that the velocity in the well was highest on the high side of the heel. A second model was run showing an open horizontal well without an invaded zone or mud cake, this model did not have the different pressure drawdown sectors preset. This model showed higher production at the heel than the model with mud cake. The pressure drawdown in the second model was consistent from heel to toe of the well whereas, due to the mud cake and invaded zone, the first model had higher drawdown shown.

A comparison of skin factors for perforated completions was performed by Sun et al (2011). A CFD model to compare skin factors between the CFD skin factor and the Karakas and Tariq model (1991) was performed. The Karakas and Tariq model shows substantially less skin factor than the CFD model under both crushed zone, the area of crushed rock surrounding the perforation tunnel, and permeability anisotropy. However, if the crushed zone is considered with isotropic permeability and the permeability damage ratio K_c/K_H is assumed with the maximum original permeability K_H in the denominator, the CFD simulations and the Karakas and Tariq model are in agreement. These results highlight the need for further study in the area of anisotropy in the perforation crushed zone. Under other cases with an isotropic formation with no damage the CFD model and the Karakas and Tariq model compare well with the CFD skin factor usually being higher. The only other area where these two models did not compare is in the case of no crushed zone in the tip of the perforation.

Theppornprapakorn (2013) used CFD to compare production from openhole sleeve completions and plug and perf completions in a hydraulic fractured horizontal well. This work used a horizontal well and gas as the fluid but started with a validation model using water as an incompressible fluid to prove the model. This validation model used a reservoir model shown in Figure 2.7 that had a horizontal well with a drainage radius of 300-feet and using a symmetry plane to only need to model half of the reservoir.

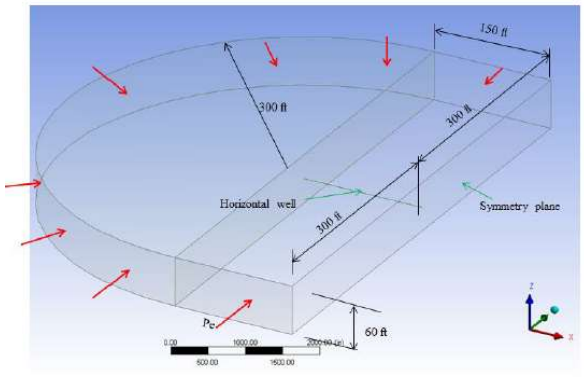

Figure 2.7 General Model Setup (Theppornprapakorn 2013)

The resulting production from the validation model compared within 0.2% to the IPR curve. The validation model was then run using a mixture of CH_4 and C_2H_6 gas. This model resulted in the CFD model producing slightly higher production, as much as 4.9% at lower drawdown pressure, than the IPR curve.

The model was then run with a single transverse fracture intersecting the plug in perf (P-n-P) completion. This model was built with two perforations 180 degrees apart from each other reaching 9 inches into the reservoir. Where there are no perforations the well is considered closed off to the reservoir. These perforations connect to a fracture body at their tip as is shown in Figure 2.8.

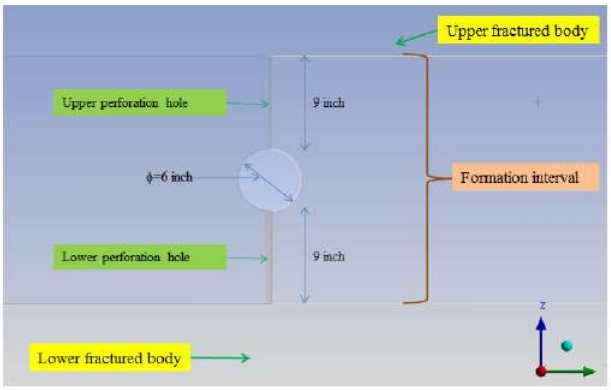

Figure 2.8 P-n-P Setup (Theppornprapakorn 2013)

This model was run with a base case using different fracture conductivities (15,000; 13,000; 11,000; 9,000;7,000; 5,000; 3,000;, 1,000; and 500 md-ft) using a fracture half-length of 150-feet and a flowing bottom hole pressure of 1000 psi. Three different cases were examined and compared to the base case. The objective was to check the effect of each of the three parameters separately. These three cases had 1) the fracture width from the base case of 0.01 inches to 0.1 or 0.3 inches, 2) changing the penetration ratio of the fracture from 150-feet to 200-feet and 250-feet, and 3) changing the vertical to horizontal permeability ratio from the base case of 0.1 to 0.5 and 1.0.

The openhole multistage completion model (OHMS) was designed in much the same way as the P-n-P model. In this model there are no perforations and the entire well is considered open to the wellbore. The fractures were connected to the wellbore down the full length of the well. This setup was then subjected to the same base model conditions and the same three cases as the P-n-P model.

The results show that for all the cases, the OHMS produced at a higher rate than the P-n-P completion. For the first case study models showed that for larger fracture propped width the flow velocity was higher although not much change was observed for each step. For the second case study the deeper the penetration of the fracture, correlated to a much larger increase in production from the reservoir for both the P-n-P and OHMS completions. This is to be expected because as the fractures run deeper into the reservoir the production will be higher since more of the reservoir is able to flow to the higher permeability inside the fracture. The third case showed the difference in the permeability ratio (k_v/k_h). This showed for both the P-n-P and OHMS model that the lower the k_v/k_h values the higher the production due to the reservoir losing the ability to drain itself from a vertical direction. These lower permeability ratios will show a larger effect on thicker reservoirs over thinner reservoirs.

Molina (2015) used CFD to compare the difference between a gravel pack completion and a frac-pack completion for a gas well. A verification case was the first case run just as was in the Theppornprapakorn (2013) work. This case was built as a round reservoir with radius of 3.5-feet, a wellbore radius of 0.125-feet, a height of 2-feet, viscosity of 0.89-cP, and permeability of 250-mD. These values were plugged into Equation 2.2 and resulted in the values presented in Table 2.1.

$$q = 0.00708\left(\frac{kh}{\mu}\right)\frac{\Delta P}{\ln\left(\frac{r_e}{r_w}\right)} \qquad [2.2]$$

Also present in Table 2.1 are the pressure values that were calculated using Fluent and the relative error. Molina (2015) showed that the Fluent program approximates the flow for the validation model with little error.

Table 2.1 Validation Model Results

Radial Distance (ft)	Predicted P(r) (psig)	Analytical P(r) (psig)	Relative Error (%)
0.125	800.36	800.00	0.05
0.263	889.15	888.58	0.06
0.538	975.34	974.09	0.13
0.745	1,014.37	1,012.84	0.15
1.020	1,052.24	1,050.36	0.18
1.227	1,074.26	1,072.35	0.19
1.503	1,098.62	1,096.50	0.20
1.778	1,118.85	1,116.58	0.22
2.054	1,136.20	1,133.76	0.22
2.260	1,147.76	1,145.19	0.22
2.536	1,161.46	1,158.90	0.22
2.742	1,170.87	1,168.24	0.22
3.018	1,182.31	1,176.66	0.22
3.224	1,190.21	1,187.56	0.22
3.500	1,200.03	1,197.33	0.23

Two simulations were set up, one for the gravel pack and one for the frac-pack completion. Figure 2.9 shows the gravel pack completion.

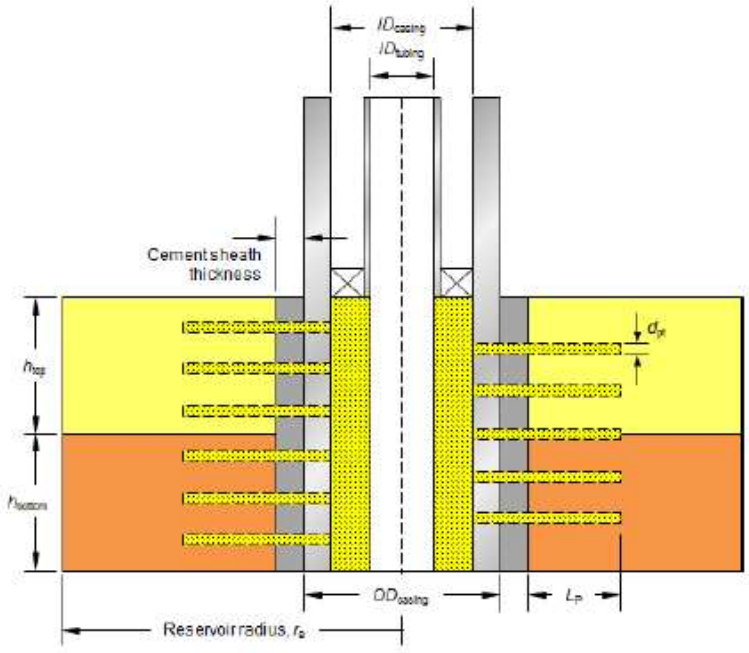

Figure 2.9 Gravel Pack Setup (Molina 2015)

The values used for the model are shown in Table 2.2.

Table 2.2 Near-Wellbore Geometry Dimensions

Top layer height	h_{top}	1	ft
Bottom layer height	h_{bottom}	1	ft
External reservoir radius	r_e	3.5	ft
Wellbore radius	r_w	0.5	ft
Production casing ID	d_i	6	in
production casing OD	d_o	6 5/8	in
cement sheath thickness	--	1 3/16	in
Production tubing string ID	--	3	in

These simulations were set up to run a series of models starting with the gravel pack completion. The length of the perforations was varied in the gravel pack completion to determine the best length for optimal production from the two-layer reservoir. The first case was set up with perforations 0.5-feet in length into the reservoir and the second case with perforations with a length of 1.0-feet into the reservoir. Between these two setups the case with a perforation length of 1.0-feet produced more than the case with a perforation length of 0.5-feet. Molina (2015) showed the pressure drawdowns for each of these cases and the streamlines for flow from the reservoir into the perforations. Figure 2.10 shows the streamlines going more into the tip of the perforations than along the length.

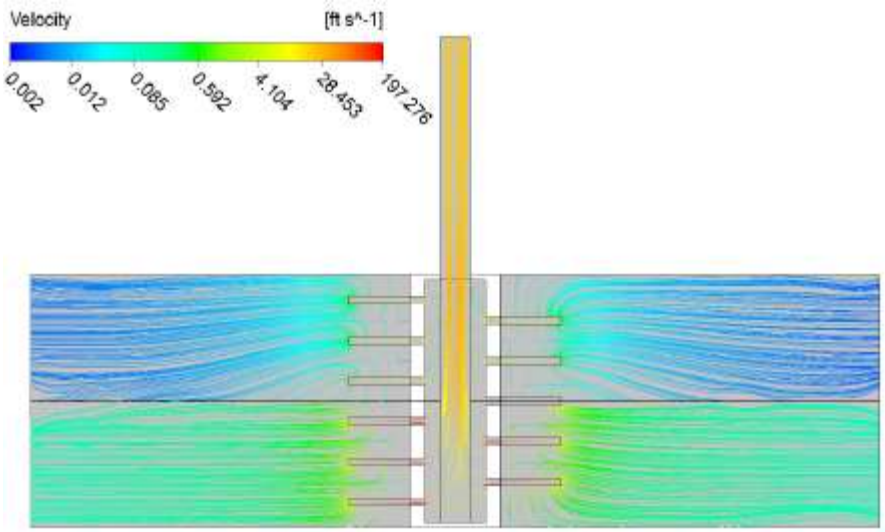

Figure 2.10 Cross-sectional flow pattern (Molina 2015)

The frac-pack completion setup is similar to the gravel pack completion and is shown in Figure 2.11.

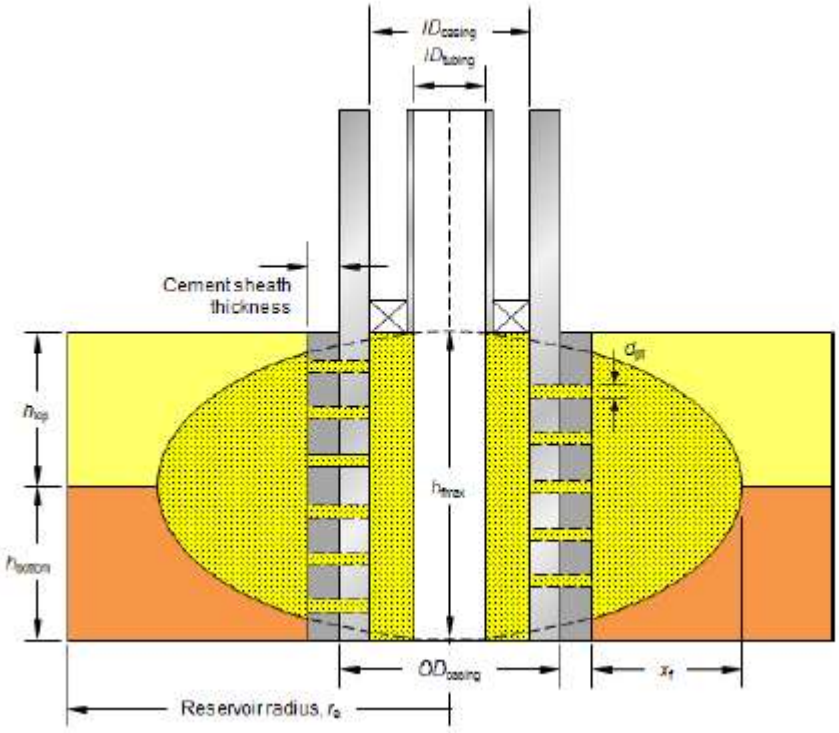

Figure 2.11 Frac-Pack Setup (Molina 2015)

This case was different than the gravel pack completion due to the bi-wing fracture that was modeled emanating from the perforations. The frac-pack completion showed a 73.56% and 52.58% increase in production rate over the two case studies for the gravel pack completion.

$$\frac{\partial p}{\partial x} = -\frac{u}{k}q \qquad [2.3]$$

Forchheimer (1901) used Darcy's equation, shown in Equation 2.3, and discovered that for substantially high Reynolds numbers in the porous media, Darcy's equation was not producing the correct results. He was able to develop a term for the inertial effects and applied it to Darcy's equation creating Equation 2.4.

$$\frac{\partial p}{\partial x} = -\frac{u}{k}q - \beta\rho q^2 \qquad [2.4]$$

The frac-pack model was first run with a value of $\beta = 0$ and showed that at high flow velocities there could be as much as a 96.65% overestimation of gas production. The frac-pack model was then run with a $\beta > 0$ value and calculated values closer to the expected values from the Darcy and Forchheimer equations. Again pressure drawdown plots were presented for each drawdown pressure.

2.3 CFD and multiphase flow

Harreras and Izarra (2013) using the OpenFOAM software, examined the flow of air and water in both an open channel environment and a pipe flow environment. The use of the open channel models was for validation of the two-phase flow model. These open channel models showed that the velocity was the highest at the top of the fluid and the velocity drop to zero at the pipe walls. The graphs of the velocity profiles showed a turbulent flow but did not show any waves forming on the surface of the flow. At the velocities modeled a wave was expected to form at the top of the flow. Harreras and Izarra (2013) postulated that the model did not have a high enough resolution to properly show the waves forming on the surface of the flow.

Harreras and Izarra (2013) showed the results from the models for the pipe flow. These turbulent pipe flows matched well with the Taitel-Dukler map for flow regime. Harreras and Izarra (2013) used the superficial velocities as the inlet velocities for ease of interpretation. Depending on the flow velocities, flow patterns from bubbly flow to annular flow was observed and the effects of gravity could were evident in the stratified flows. The inclined flow in the closed channels did not show useful results. The authors stated that the domain would drain of all fluid and no cause could be determined as to why. This would cause the model to run as complete gas flow and not produce the desired results. Due to the low resolution of the models and high computational costs the velocity profiles were not as developed as they should be and it was difficult to compare them to the theoretical values.

In 2006 there were two different works generated that used CFD for pipe flow simulations. In the first one Shuard et al. (2018) modeled two-phase pipe flow in OpenFOAM. They modeled the two-phase air-water pipe flow to plot the velocity profiles and pressure gradients along the length of the pipe. The mesh for the model was generated using the square core with inflation layers to allow for full resolution of the boundary layers. Shuard et al. used only a half-pipe mesh and showed that there was little if any lateral flow in the pipe so a full-pipe was not needed for the computations which allowed for fewer nodes and thus less computation time. The longitudinal mesh size was not listed but from the image shown of the mesh, Figure 2.12**Error! Reference source not found.**, and the total number of cells, 352,628, in the 4-meter long pipe it is safe to assume it was a rather large step for each slice. They found that a finer mesh would be needed in the longitudinal direction to be able to properly model dispersed bubble and froth flows. Shuard et al. listed the boundary conditions for each of the different values that the OpenFOAM software needs to calculate the solution and the K-ω SST model was used for the turbulence modeling. Overall this work showed that two-phase flow models in OpenFOAM for air-water systems had a good correlation with the theoretical values for holdup and an up to 30% difference with the pressure drop correlations. The authors pointed out that higher velocity liquid flows result in more accurate pressure drop calculations than did higher velocity gas flows.

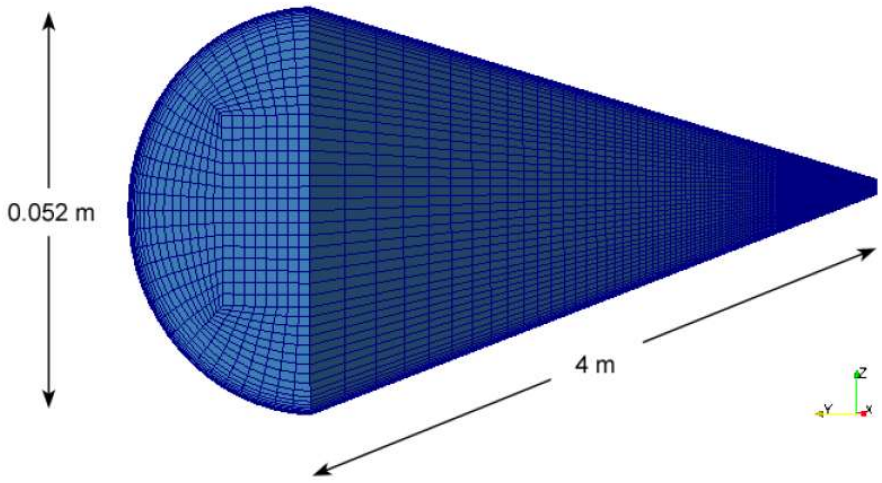

Figure 2.12 Mesh from Shuard et al. (2018)

The second work presented in 2016 was done by Peters (Peters 2016) and was a comparison of solvers for multi-phase flow in pipes. Peters used a T-junction model to test the interFoam and multiPhaseEulerFoam solvers available in OpenFOAM. The mesh for the T-junction model was generated using a similar square core with an inflation layer setup as Shuard et al. except for the layers on the outside of the pipe were not set up for a full resolution approach. Peters did not study pressure drop along the length of the pipe since it was a T-junction style pipe, but the liquid holdup was compared between the two different solvers. It was found that each of the solvers performed well with both having their advantages and disadvantages. The interFoam solver was less oscillatory than was the multiPhaseEulerFoam solver for both liquid holdup and pressure. Both solvers performed similarly but the multiPhaseEulerFoam solver operates at 115 to 152% increase in computational time. Peters recommends the use of the interFoam solver for multiphase pipe flow. Peters also pointed out that a finer mesh should be used to correctly model the flow regime in the pipe.

3 CHAPTER THREE: COMPUTATIONAL FLUID DYNAMICS OVERVIEW

3.1 Introduction to Computational Fluid Dynamics

The study of fluid dynamics started in the seventeenth century with the creation of experimental techniques and progressed in the eighteenth and nineteenth centuries with more theoretical aspects. Until the mid-twentieth century, experimental and theoretical techniques were the two components that made up fluid dynamics. With the computer revolution in the twentieth century came a new third dimension, CFD (Anderson 1995). CFD has become common place in many industries including aerospace, automotive, biomedical engineering, and electrical and electronic engineering. CFD is based on fluid flows being controlled by three governing laws, conservation of mass, Newton's second law, and conservation of energy. These three equations, in their original form, are either partial differential equations or integral equations and CFD is used to replace these equations with discrete algebraic equations (Anderson 1995).

CFD simulation models can be separated into three aspects for solving: pre-processing, solver, and post-processing. In the pre-processing stage a model is designed based on the desired problem to solve. This will include building a geometrical model, generating the grid, selection of the physical process to be modeled, definition of fluid properties, and boundary condition selection. In the solver section the integration of all the governing equations is performed over the control volumes, discretization is performed, and the algebraic equations are solved in an iterative process. In the post-processing stage the domain geometry and grid is displayed, vector plots can be generated, and 2D and 3D plots based on the solution. Post-processing is used to display the final solution to the problem and interoperate the results from the algebraic equations (Versteeg and Malalasekera 2007).

The pre-processor step is used to specify the boundary of the system. A computer-aided design (CAD) model, in either 2D or 3D, is built to describe the model. This CAD model is then sent through a meshing program to divide the model up into a finite number of nodes. Each of these nodes will have the governing equations solved specifically for it, thus a larger number of nodes requires a longer processing time to for the solution to be generated. The nodes are generally not all the same size or shape as there are large open areas to cover and smaller intricate areas that require more detail. Generally, the fluid properties are known for the problem being posed. For example, air if it is an aerodynamic problem, water for shipping hydraulic models, and oil for the petroleum industry. Over half the time of building the CFD model will be spent in defining these steps. The more effort that is put into the geometry design process and meshing, the less troubleshooting will occur when running the model.

The solver step will require the most processing time and power as this is where the actual calculations will be performed. Each node will have the governing equations solved for it during each of the iterations. CFD problems can be solved with either a pressure based or density based setup. The pressure based solver uses an algorithm which belongs to a general class of methods called the projection method (Chorin 1968). In this method the pressure equation is derived from the continuity and momentum equations in a way that the velocity field satisfies continuity. There are two different types of pressure based solvers, segregated algorithm and coupled algorithm. The pressure based segregated algorithm solves the governing equations segmentally. The pressure based-coupled algorithm solves a coupled system of equations including the momentum and pressure-based continuity equations. This coupled algorithm uses 1.5-2 times the computer memory as the segregated algorithm but converges at a much faster rate. Figure 3.1 shows a flow chart for these two different pressure-based algorithms. The density based solver solves the continuity, momentum, energy, and species equations simultaneously much like the coupled pressure-based solver (ANSYS 2013).

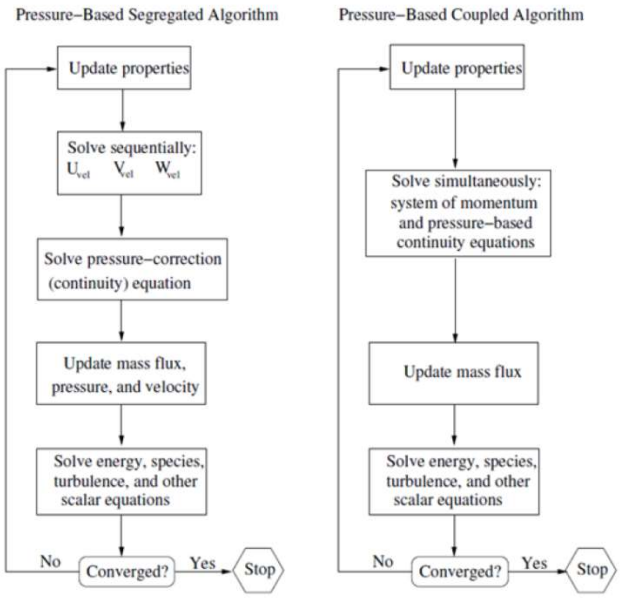

Figure 3.1 Pressure-Based Solver Algorithms (ANSYS 2013)

Post-processing is the step in which the solution is examined and different 2D and 3D diagrams can be produced. In this step, the results are analyzed to make sure they fit the criteria set aside for proper solving of the problem. With the advancement of computers in recent years, these results have started to include visual representations of the results including animations.

3.2 Computational Fluid Dynamics Governing Equations

The solver step of the process sets out to solve a system of equations that include the momentum and mass equations. The three governing equations that control fluid flow are the conservation of mass, Newton's second law, and the conservation of energy. Since the questions being posed in this study are for incompressible fluids and the system is isothermic, the conservation of energy can be ignored. This leaves the conservation of mass and Newton's second law that need to be solved for each node in the system.

The conservation of mass is a simple concept; mass is neither created nor destroyed in the system. In this case, this means that the same amount of fluid that comes into a pipe at the inlet leaves the pipe at the outlet.

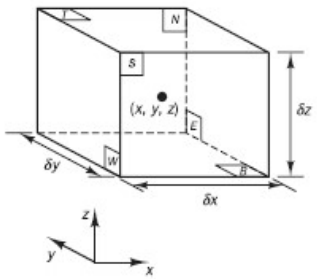

Figure 3.2 Fluid Element for Conservation Laws (Versteeg and Malalasekera 2007)

Figure 3.2 shows a single node for model with sides δx, δy, and δz and will be used to derive the conservation of mass and momentum equation that will be used by the solver. The conservation of mass states that the mass into the element is the same as the mass out of the element therefore, the rate of

increase of mass in the fluid element is equal to the rate of flow of mass into the element as given by Equation 3.1.

$$\frac{\partial}{\partial t}(\rho\delta x\delta y\delta z) = \frac{\partial \rho}{\partial t}\delta x\delta y\delta z \quad [3.1]$$

The mass flow rate across the face of the element can be defined where flow into the box is given a positive sign and flow out of the box is given a negative sign. Figure 3.3 shows the net rate in flow of mass across each interface.

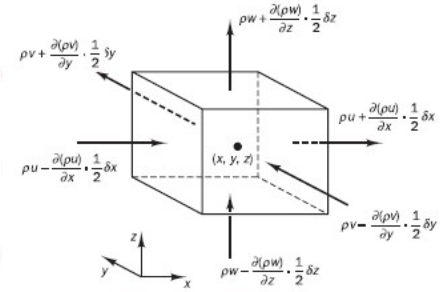

Figure 3.3 Mass flow in and out of a fluid element (Versteeg and Malalasekera 2007)

Equation 3.2 shows the net rate of flow of mass across each interface mathematically

$$\begin{aligned}\left(\rho u - \frac{\partial(\rho u)}{\partial x}\frac{1}{2}\partial x\right)\partial y\partial z - \left(\rho u - \frac{\partial(\rho u)}{\partial x}\frac{1}{2}\partial x\right)\partial y\partial z + \left(\rho v - \frac{\partial(\rho v)}{\partial y}\frac{1}{2}\partial y\right)\partial x\partial z \\ - \left(\rho v - \frac{\partial(\rho v)}{\partial y}\frac{1}{2}\partial y\right)\partial x\partial z + \left(\rho w - \frac{\partial(\rho w)}{\partial z}\frac{1}{2}\partial z\right)\partial x\partial y \\ - \left(\rho w - \frac{\partial(\rho w)}{\partial z}\frac{1}{2}\partial z\right)\partial x\partial y\end{aligned} \quad [3.2]$$

which simplifies to.

$$\frac{\partial \rho}{\partial t} + \nabla(\rho u) = 0 \quad [3.3]$$

Since the fluid is considered incompressible the density is constant and Equation 3.3 becomes

$$\nabla u = 0 \quad [3.4]$$

Newton's second law states that the force on an object is equal to the object's mass times it's acceleration. In the case of a moving fluid the rate of increase of momentum is equal to the sum of the forces acting on the fluid. Equation 3.5 gives the rate of increase of the x-, y-, and z-momentum per unit volume as.

$$x - momentum = \rho\frac{Du}{Dt} \quad [3.5a]$$

$$y - momentum = \rho\frac{Dv}{Dt} \quad [3.5b]$$

$$z - momentum = \rho \frac{Dw}{Dt} \quad \textbf{[3.5c]}$$

The total force per unit volume is given by Equation 3.6.

$$x - force\ per\ unit\ volume = \frac{\partial(-p + \tau_{xx})}{\partial x} + \frac{\tau_{yx}}{\partial y} + \frac{\tau_{zx}}{\partial z} \quad \textbf{[3.6a]}$$

$$y - force\ per\ unit\ volume = \frac{\tau_{xy}}{\partial x} + \frac{\partial(-p + \tau_{xy})}{\partial y} + \frac{\tau_{zy}}{\partial z} \quad \textbf{[3.6b]}$$

$$z - force\ per\ unit\ volume = \frac{\tau_{xz}}{\partial x} + \frac{\tau_{yz}}{\partial y} + \frac{\partial(-p + \tau_{zz})}{\partial z} \quad \textbf{[3.6c]}$$

Setting Equation 3.5 equal to Equation 3.6 results in the component of momentum equation in the x, y, or z direction respectively where τ is the stress component and $S_{Mx,y,z}$ are the source terms including contributions due to body forces only, for example gravity would be modelled by $S_{Mx} = 0$, $S_{My} = 0$, and $S_{Mz} = -\rho g$.

$$\rho \frac{Du}{Dt} = \frac{\partial(-p + \tau_{xx})}{\partial x} + \frac{\tau_{yx}}{\partial y} + \frac{\tau_{zx}}{\partial z} + S_{Mx} \quad \textbf{[3.7a]}$$

$$\rho \frac{Du}{Dt} = \frac{\tau_{xy}}{\partial x} + \frac{\partial(-p + \tau_{yy})}{\partial y} + \frac{\tau_{zy}}{\partial z} + S_{My} \quad \textbf{[3.7b]}$$

$$\rho \frac{Du}{Dt} = \frac{\tau_{xz}}{\partial x} + \frac{\tau_{yz}}{\partial y} + \frac{\partial(-p + \tau_{zz})}{\partial z} + S_{Mx} \quad \textbf{[3.7c]}$$

The momentum equation can also be written in the following form given by Equation 3.8

$$\frac{\partial}{\partial y}(\rho \boldsymbol{v}) + \nabla \cdot (\rho \boldsymbol{v}\boldsymbol{v}) = -\nabla p + \nabla \cdot (\tau) + \rho \boldsymbol{g} + \boldsymbol{F} \quad \textbf{[3.8]}$$

where τ is

$$\tau = \mu \left[(\nabla \boldsymbol{v} + \nabla \boldsymbol{v}^T) - \frac{2}{3} \nabla \cdot \boldsymbol{v} I \right] \quad \textbf{[3.9]}$$

Discretization is the practice of transforming continuous differential equations into discrete difference equations that can be solved numerically. There are three common methods for discretization: finite difference, finite element, and finite volume methods. Of these three methods, OpenFOAM uses the finite volume method. This method is used to divide the problem into a finite number of nodes called meshing. The differential equations given are then integrated over the nodes which results in a unique set of algebraic equations for each node.

3.3 Turbulence Modeling

3.3.1 Laminar and Turbulent Flow

Fluid flow regimes used in engineering calculations can take one of two forms, laminar or turbulent. Laminar flow is characterized by flow in layers that are adjacent to each other. These layers slide past

each other smoothly in an orderly fashion. When The Navier Stokes equations, Equations 3.7a,b, and c, are combined with the continuity equation, as shown in Equation 3.3, they can fully describe simple laminar flows. Turbulent flow is characterized by random chaotic movement of the particles making the mathematical description of the flow difficult. Unlike laminar flow, turbulent flow always has a three-dimensional spatial characteristic with rotational eddies dominating the flow (Versteeg and Malalasekera 2007).

Flow in pipes is a special case for both laminar and turbulent flow regimes. Turbulent pipe flow is both laminar and turbulent at the same time with the area nearest the wall being laminar and the area in the middle of the pipe being turbulent. Inertial forces dominate the flow further away from the wall with viscous effects dominating at the near wall region. At the wall a thin layer of fluid known as the viscous sub-layer is stationary. Beyond the viscous layer there is a layer where both viscous and turbulent flows are important, known as the log-law layer. The next layer out from the pipe is called the viscosity-deflect law layer or the law of the wake. This layer can overlap with the log-law layer but the two layers have to be equal (Tennekes and Lumley 1972). These layers are split into two groups, the inner region and the outer region. The inner region is made up of the viscous sub-layer, a buffer layer, and the log-law layer and makes up 10-20% of the total thickness. The outer region is made up of the law of the wake layer and is dominated by inertial flows free from viscous effects (Versteeg and Malalasekera 2007). For this study a Reynolds number of 2100 will be used to differentiate between laminar and turbulent flow.

3.3.2 Turbulence Flow Models

Turbulence models can be split into three categories, Reynolds-averaged Navier-Stokes (RANS) equations, large eddy simulations, and direct numerical simulations. A few of the more popular RANS models will be discussed, for information about large eddy simulations and direct numerical simulations refer to Versteeg and Malalasekera (2007). The majority of turbulent flow in engineering calculations is done using RANS model. These calculations require a turbulence model to be developed for the Reynolds stress and scalar transport terms as well as close the system of mean flow equations, Equation 3.3, Equation 3.7a-c, and the scalar transport equation that is not used in this work as it applies to temperature differences.

3.3.2.1 Mixing Length Model

The mixing length model attempts to describe the stress as a simple algebraic formula for the viscosity μ. This model works well for simple two-dimensional turbulent flows, is easy to implement, requires little computing power, and has good predictions for thin shear layers (Versteeg and Malalasekera 2007). Some of the disadvantages include it being completely incapable of describing flows with separation and recirculation as well as only calculating the mean flow properties and turbulent shear stress.

The kinematic turbulent viscosity is given by Equation 3.10 and the dynamic turbulent viscosity is given by Equation 3.11. Where C is a dimensionless constant of proportionality, v is the turbulent velocity, ρ is the density, and l is the turbulent length scale.

$$v_t = C\vartheta l \quad \textbf{[3.10]}$$

$$\mu_t = C\rho\vartheta l \quad \textbf{[3.11]}$$

For simple two-dimensional flows it can be shown that

$$\vartheta = cl\left|\frac{\partial U}{\partial y}\right| \quad \textbf{[3.12]}$$

Combining Equation 3.10 and Equation 3.12, the Prandtl's mixing length model is formed in Equation 3.13

$$v_t = l_m^2 \left|\frac{\partial U}{\partial y}\right| \quad \textbf{[3.13]}$$

With the turbulent Reynolds stress described as

$$\tau_{xy} = \tau_{yx} = -\rho\overline{u'v'} = \rho l_m^2 \left|\frac{\partial U}{\partial y}\right| \frac{\partial U}{\partial y} \quad \textbf{[3.14]}$$

The mixing length model is not itself used in many CFD applications but will be combined into other models describing near wall flow.

3.3.2.2 The k-ε Model

The k-ε model is concerned with the mechanisms that affect kinetic turbulent energy. This model is the most widely used and validated turbulence model (Versteeg and Malalasekera 2007). It is used in calculating thin shear layer and recirculating flows in a wide range of industrial applications. The k-ε model is more difficult to implement than the mixing length model in the terms of computing time as there are more equations to solve. The k-ε model is poor at predicting rotating flows, flows driven by anisotropy of Reynolds stresses, and flows with large extra strains (Versteeg and Malalasekera 2007).

The equations for the k-ε model are given by Equation 3.15 and Equation 3.16.

$$\frac{\partial(\rho k)}{\partial t} + div(\rho k \boldsymbol{U}) = div\left[\frac{\mu_t}{\sigma_k} grad\ k\right] + 2\mu_t S_{ij} \cdot S_{ij} - \rho\varepsilon \quad \textbf{[3.15]}$$

$$\frac{\partial(\rho \epsilon)}{\partial t} + div(\rho \epsilon \boldsymbol{U}) = div\left[\frac{\mu_t}{\sigma_\epsilon} grad\ \epsilon\right] + C_{1\epsilon}\frac{\epsilon}{k} 2\mu_t S_{ij} \cdot S_{ij} - C_{2\epsilon}\rho\frac{\epsilon^2}{k} \quad \textbf{[3.16]}$$

Where μ_t is the eddy viscosity given by Equation 3.16.

$$\mu_t = \rho C_u \frac{k^2}{\varepsilon} \quad \textbf{[3.17]}$$

The left hand side of the equation can be read as the rate of change of k or ε plus the transport of k or ε by convection. Whereas the right hand side of the equation states the transport of k or ε by diffusion plus the rate of production of k or ε minus the rate of destruction of k or ε. The adjustable constants in the equation are given by $C_\mu = 0.09$, $\sigma_k = 1.00$, $\sigma_\varepsilon = 1.30$, $C_{1\varepsilon} = 1.44$ ad $C_{2\varepsilon} = 1.92$ with the constants arrived at by data fitting of a wide range of turbulent flows (Versteeg and Malalasekera 2007).

The realizable model is different from the standard k-ε model in two important ways, an alternate formulation for turbulent viscosity and a modified transport equation for the dissipation rate. The term realizable means that the model satisfies certain mathematical constraints on the Reynolds stress that neither the standard k-ε model nor the RNG k-ε model satisfies (Versteeg and Malalasekera 2007).

3.3.2.3 The k-ω Model

The most popular alternative to the k- ε model is the k-ω model. In this model, the turbulent frequency ω= ε/k is used as the second variable. This model first attracted attention since the near wall area of the

flow does not require a wall-damping function at low Reynolds numbers. The turbulence kinetic energy k is set to zero at the wall and ω tends to infinity at the wall. This model is best when used in general purpose CFD and external aerodynamics applications, and best for flow over a backward facing step (Versteeg and Malalasekera 2007).

The flow equations for k and ω are given in Equation 3.17 and Equation 3.18 respectively.

$$\frac{\partial(\rho k)}{\partial t} + div(\rho k \boldsymbol{U}) = div\left[\left(\mu + \frac{\mu_t}{\sigma_k}\right) grad\ k\right] + \left(2\mu_t S_{ij} \cdot S_{ij} - \frac{2}{3}\rho k \frac{\partial U_i}{\partial x_j}\delta_{ij}\right) - \beta^* \rho\omega \qquad \textbf{[3.17]}$$

$$\frac{\partial(\rho \omega)}{\partial t} + div(\rho \omega \boldsymbol{U}) = div\left[\left(\mu + \frac{\mu_t}{\sigma_\omega}\right) grad\ \omega\right] + \gamma_1\left(2\rho S_{ij} \cdot S_{ij} - \frac{2}{3}\rho\omega \frac{\partial U_i}{\partial x_j}\delta_{ij}\right) - \beta_1 \rho\omega^2 \qquad \textbf{[3.18]}$$

The left hand side of the equations is read as the rate of change of k or ω plus the transport of k or ω by convection. Whereas the right hand side of the equations is read as the transport of k or ω by turbulent diffusion plus the rate of production of k or ω minus the rate of dissipation of k or ω. The values of the constants for Equation 3.17 and Equation 3.18 are given by $\sigma_k = 2.0$, $\sigma_\omega = 2.0$, $\gamma_1 = 0.533$, $\beta_1 = 0.075$, and $\beta^* = 0.09$ (Versteeg and Malalasekera 2007). These equations are similar to those given by the k-ε model with the largest difference being in the terms for production and dissipation of k and ω.

4 CHAPTER FOUR: METHODOLOGY

4.1 Model Construction

The first phase used experimental data gathered by Hulsurkar (2017) at the University of Alaska Fairbanks. In order to move from the experimental setup of Hulsurkar (2017) to the world of CFD, a comparable CAD model needed to be constructed. Hulsurkar (2017) used a 1.5-inch diameter schedule 80 PVC pipe (Hulsurkar 2017), which has an internal diameter of 1.5-inches and an external diameter of 1.9-inches. The test section of the pipe was 24-feet long to allow for adequate visualization of the flow inside the pipe. Figure 2.3 shows the experimental setup from the work performed by Hulsurkar (2017) in the lab.

The OpenFOAM CFD software only works in SI units so the diameter of the model was determined to be 0.0381-meters (1.5-inches). Since the fluid is only flowing inside the pipe, there was no need for modeling the outside wall of the pipe so a diameter of 0.0381-meters was used for the outer wall of the model. There was no need to model more than the test section of the original experimental setup because all that this study is concerned with is matching pressure gradients based on velocities and examining liquid holdup values compared to what the original experiment observed. Since the length of the model greatly affects the computational time it was important to keep the model as short but accurate as possible.

The hydrodynamic entry length of a given fluid is the length that it takes for a fluid entering a pipe to develop its given flow pattern (Cengel and Cimbala 2006). This region of the pipe is affected by different physics than the area of the pipe where the flow pattern is developed and thus should not be used for calculations or observations. The length from the pipe entrance to where the flow reaches 2-percent of the wall shear stress for fully developed flow, the hydrodynamic entry length, is given by Equation 4.1 for laminar flow and Equation 4.2 for turbulent flow where Re is the Reynolds number as given in Equation 4.3 and D is the diameter of the pipe (Cengel and Cimbala 2006).

$$L_h = 0.05ReD \tag{4.1}$$

$$L_h = 1.359DRe_D^{1/4} \tag{4.2}$$

Equation 4.3 shows how the Reynolds number is calculated and shows that the dynamic viscosity μ is inversely proportional to the Reynolds number and the characteristic linear dimension, the diameter D, is directly proportional. This means that the least viscous fluid in the largest pipe will have the largest Reynolds number and thus the highest hydrodynamic entry length. Reynolds number is defined as where ρ is the density and V is the fluid velocity.

$$Re = \frac{\rho VD}{\mu} \tag{4.3}$$

Hulsurkar (2017) used three different oil mixtures in his experimental work along with air as the gas phase. Table 4.1 gives the density and dynamic viscosity of each of these mixtures. Hulsurkar (2017) stated that the data for mix1 showed anomalously high differential pressures due to logging errors and due to this was not considered for this study.

Table 4.1 Fluid properties (Hulsurkar 2017)

Fluid	Density [kg/m3]	Dynamic Viscosity [kg/ms]
Air	1.225	1.789E-05
Mix1 Oil	824	0.150
Mix2 Oil	830	0.197
Mix 3Oil	837	0.218

Using the 3.5-inch pipe with an internal diameter of 2.992-inches, 0.0759-meters, and since mix 2 is less viscous than mix 3 it was used to determine the longest hydrodynamic entry length. Performing the calculations for this highest flow velocity of the mix 2 fluid in laminar flow results in a value of 0.535-meters for the hydrodynamic entry length for a flow velocity of 0.44-m/s. Since the hydrodynamic entry length for the turbulent flow is calculated by Equation 4.2 it is easy to see that the 3.5-inch model will have the longest length of all of the models at 1.252-meters. The CAD model was built as a cylinder of 4-meters in length with a diameters as given in Table 4.2 for each case.

Table 4.2 CAD Model Diameters

Case	Model Diameter [in]	Model Diameter [m]
Base	1.5	0.0381
2.875	2.441	0.0620
3.5	2.992	0.0760

Although there was the option to model the pipe as a half section and use a symmetry plane similar to Shuard et al. (2016) the decision was made to model the pipe as a full section in order to eliminate any uncertainty that may arise. The finalized CAD model is shown in Figure 4.1.

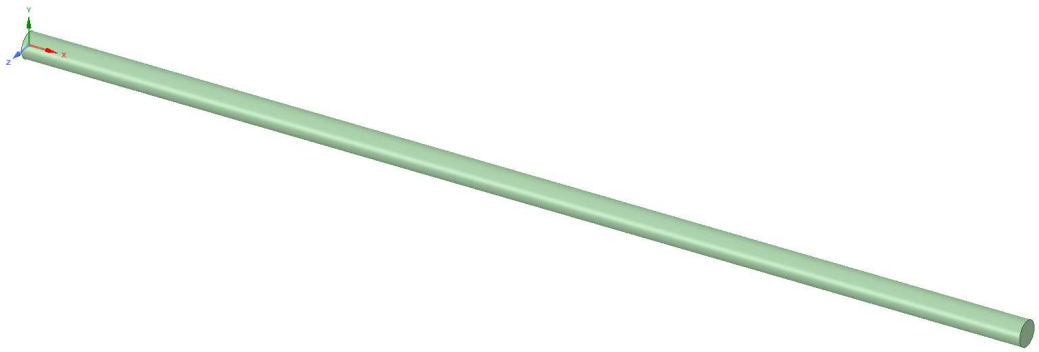

Figure 4.1 Final CAD model

4.2 Meshing

4.2.1 Structured vs. Unstructured

The governing partial differential equations defined in chapter 3 need to be discretized in order to be solved numerically. This discretization process involved applying a mesh over the problem geometry that divides the domain into a set of non-overlapping discrete elements called grid elements or grid nodes (Moukalled et al. 2016). There are several steps involved in generating the mesh and getting the model ready to be run. The first of these processes is to determine what type of mesh would be best for the given domain. Generally speaking there are only two types of mesh grids employed in CFD simulations, structured and unstructured (Feszty and Jakubik). As the names imply the structured mesh will resemble a more planned out mesh that follows a given pattern or organization. The unstructured mesh is a haphazard arrangement of cells that allow for covering the geometry. Structured meshes are better for geometries that are not as complex and do not require as much local refinement, meshing a building or an open channel. Unstructured meshes are used for problems that have complex geometries, meshing a Formula One car or a fighter jet. Unstructured meshing can also be used for local refinement of smaller objects inside a given domain. Structured meshes are less computationally intensive due to the shape of the cells in the mesh, whereas unstructured mesh will generally require more computational time due to the complexities in the cell shapes.

Once the type of meshing is determined then the cell shape needs to be determined. For a two-dimensional model there would be two basic cell shapes that would be formed by both the structured and unstructured mesh, a triangle and a square. Higher order polygons (pentagon, hexagon, etc.) are allowed and are commonly used in meshing but higher order polygons need more computational time. Circular shapes could not be used due to the nature of the discretization scheme used in CFD equations. Since a circle is a polygon with infinite sides an infinite number of equations would need to be generated to describe the flow across each edge. Translating the triangle and square into a three dimensional models would results in cells shaped as tetrahedrons, pyramids, triangular prisms, and hexahedrons. A structured grid lends itself to being discretized by the rectangular or hexahedral shapes whereas an unstructured grid lends itself to being discretized by the triangular or tetrahedron type shapes (Henshaw 1996). Triangular or tetrahedral shaped meshes require more cells per area compared with rectangular or hexahedral shaped meshes. Triangular or tetrahedral shaped meshes require more processing time as there are more vertex points and more cell centers for the software to resolve the partial differential equations into numerical solutions (Henshaw 1996).

For the meshing of the model that was built for this study a structured grid was selected with hexahedral cells because it is a simple pipe shape. The mesh was generated with a simple core shape and the outer portion being made up of inflation layers. The mesh can be made of the simple core shape all the way to the edge of the model but it will not allow for the description of the boundary layer effects at the wall of the pipe. This type of mesh is used extensively in pipe flow CFD models (Ghorai and Nigam 2005; Herreras and Izarra 2013; Peters 2016; Shuard et al. 2016; Tocci et al. 2017; Chinello et al. 2018) as shown in Figure 4.2, this type of mesh can be referred to as an O-grid (Tu et al. 2013).

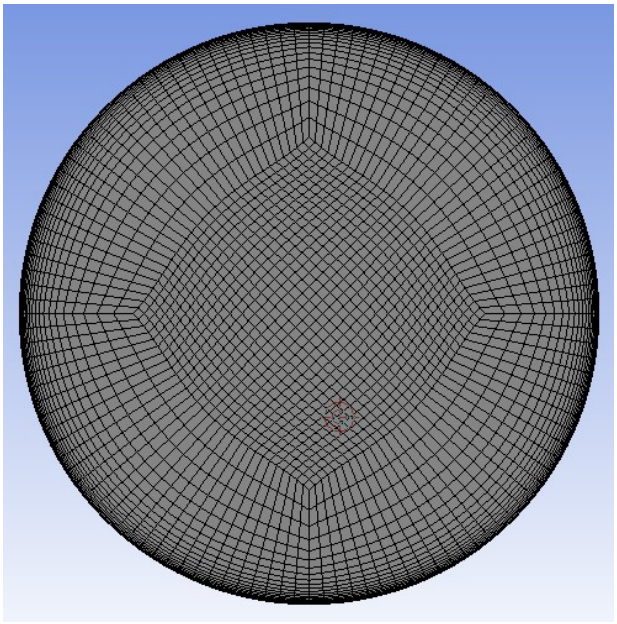

Figure 4.2 O-grid type mesh

4.2.2 First cell height y^+

There are two options for modeling near wall turbulence; either the boundary layer region is resolved, meaning inflation layers are used to model the wall region of the pipe, or it is not resolved, meaning wall functions must be specified in the model (Kalitzin et al. 2005). If the boundary layer region is not resolved, then wall functions must be used while running the model so that the CFD software can properly determine the flow conditions near the wall. If the enhanced wall treatment option is selected then it is required to have a finer mesh in the area of the wall to properly resolve the boundary layer region, with at least 10 cells being required in this region (ANSYS 2006).

In the previous section it was stated that the circular O-grid core was surrounded by a set of inflation layers. These inflation layers are a set of cells that start a smaller size and grow by a set factor for each new layer that is added. The model was built with a total of twenty inflation layers with a growth rate of 120-percent. The total number of layers needed is arbitrary but needs to cover the near wall region of the model so that the turbulence is correctly modeled at the wall.

To determine the correct size for the first cell at the wall, the calculation of the y^+ value will need to be made. This y^+ value is a dimensionless-distance from the wall and can be calculated using Equations 4.4 through 4.7 (CFD-Online 2011).

$$C_f = [2\log_{10}(Re) - 0.65]^{-2.3} \quad \textbf{4.4}$$

$$\tau_w = C_f \frac{1}{2}\rho U_{free}^2 \quad \textbf{4.5}$$

$$u_* = \sqrt{\frac{\tau_w}{\rho}} \quad \textbf{4.6}$$

$$y^+ = \frac{y\rho u_*}{\mu} \quad \textbf{4.7}$$

Three different layers make up the inner region of turbulent flow including the viscous sub-layer, the buffer layer, and the overlap or log layer. There is a single layer that makes up the outer region of the boundary layer called the wake. Both the inner region and outer region are shown in Figure 4.3 along with their respective y^+ cutoffs per region. The viscous sub-layer is a laminar region of flow that is near the wall, $y^+ < 5$. The velocity profile in this region follows the law of the wall as is given in Equation 4.8 and gets thinner as the velocity increases (Cengel and Cimbala 2006).

$$\frac{u}{u_*} = \frac{yu_*}{v} \quad \textbf{4.8}$$

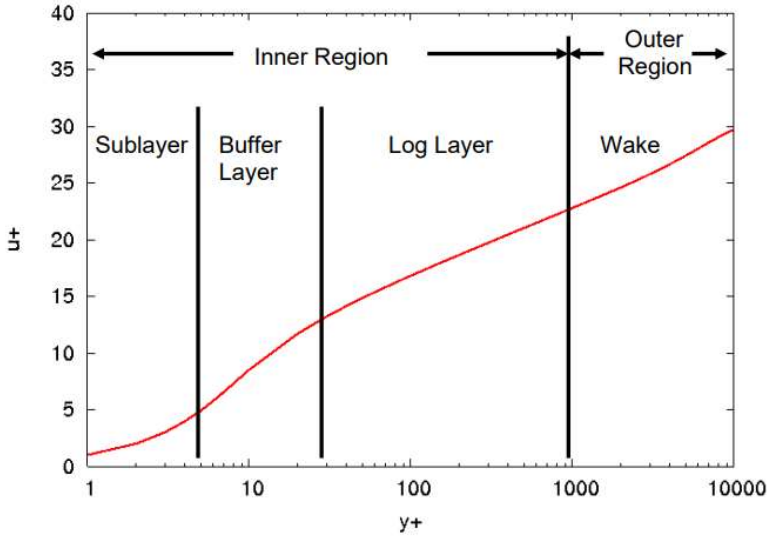

Figure 4.3 Near wall turbulent boundary regions (Nichols)

The overlap, or log layer, is the region where $30 < y^+ < 1000$ and does not follow the law of the wall for the velocity profile. Experiments have confirmed that this region is proportional to the logarithm of the distance from the wall (Cengel and Cimbala 2006) and can be expressed as in Equation 4.9 which is known as the logarithmic law. The buffer layer, $5 < y^+ < 30$, does not follow either of these two laws and is a transition zone from the sublayer to the log layer. When $y^+ > 1000$ then the flow is in the outer region and starts to conform to the known equations for the velocity profile of a turbulent flow. For this reason, it is important that the inflation layers extend out to at least a y^+ value of 1000 before transitioning to the center O-grid of the model.

$$\frac{u}{u_*} = \frac{1}{k}\ln\frac{yu_*}{v} + B \quad \textbf{4.9}$$

The initial model with 1.5-inch diameter was meshed based on this information. A y^+ value was calculated for each of the given flow velocities so that an average y^+ value for the model could be

obtained. **Error! Reference source not found.** shows the values of y^+ for each of the flow velocities. A first cell size of 4.0E-05-meters was picked for the model based on the characteristics of air for density and viscosity. This value allows for a velocity of 5.38 m/s to be at a y^+ value of 1.0 with any velocity slower than that to be a lower value and any velocity faster than that to be a higher value. Due to the pipe size, the entire flow takes place within the three inner regions since a y^+ of 1000 results in a distance greater than a full diameter of the pipe. For this reason, a maximum of twenty cells was selected for the boundary layer. As the model was up scaled, the first layer thickness was kept the same for each model since the small changes in the size did not result in appreciable changes in the y^+ values.

Table 4.3 Calculated y^+ values

Velocity [m/s]	y^+
0.04	0.02
0.10	0.04
0.31	0.09
0.41	0.11
0.50	0.13
0.83	0.20
1.24	0.29
1.66	0.37
2.48	0.51
3.31	0.66
4.14	0.80
4.56	0.87
5.38	1.00
5.80	1.07
6.83	1.24
7.45	1.33
8.28	1.46
9.11	1.59

4.2.3 Mesh Generation

Once the initial O-grid was set up with the boundary layers at the correct distance for the given y^+ value the mesh was generated using a multi-zone technique. This multi-zone technique is a simple setup that allows the software to generate a repeating mesh based on the initial setup at a known distance. It was important to have enough cells that the model was properly resolved but not to have so many that there was excessive computation time for each model. Initially a sweep element size of 5-centimeters was selected for each of the multi-zone slices but upon running the models the results were not as expected as will be explained in the sensitivity analysis section. For this reason, a sweep element size of 5-milimeters was chosen for each of the multi-zone slices.

The ANSYS Meshing utility was used to generate the mesh for each of the models and it was translated into a format that OpenFOAM could read via the OpenFOAM software. The process of meshing is not exceptionally processor intensive for this simple model but throughout the many mesh files generated for this study it was obvious that a small increase in complexity results in a large increase in computational

time. It is best to do some research ahead of time as to what all needs to be done with the mesh so that it is generate properly the first time. Figure 4.4 shows the final meshed surface of the model.

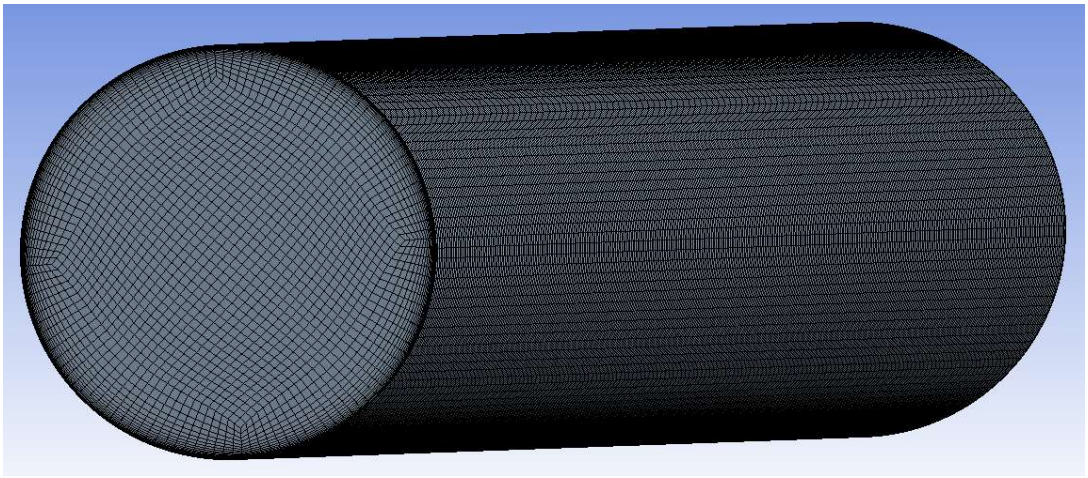

Figure 4.4 Final meshed model

4.3 Boundary Conditions

In order for the OpenFOAM solver to properly find a solution it will need to know what to do at the boundaries of the model. Boundary conditions in CFD are the same as initial and boundary conditions that are needed to solve any differential or partial differential equation. Since the purpose of the CFD model is to find a solution to the Navier-Stokes and continuity equations, it makes sense that a boundary condition would be required as the starting point for the modeling process. There are three boundaries to consider for this simple model the inlet, the outlet, and the wall. Each of these boundaries will have a unique setup for all of the variables that will be calculated by the solver. The boundary conditions will be similar for the laminar and turbulent case but not identical.

4.3.1 Laminar Cases

Starting with the easiest model boundary to define, the outlet, there are two initial boundary conditions that need to be specified, the pressure and the velocity. These boundary conditions will remain set for the duration of the simulation. For the pressure boundary condition a fixed pressure of zero was set to make the calculation of the pressure gradients easier. Fixing this value to zero also allows for the pressure in the system to build as it moves toward the inlet. The pressure is given as the kinematic pressure with the dimensions of m^2/s^2. In order to arrive at a pressure in units of Pascal for the system this kinematic pressure needs to be multiplied by the density. The velocity term for the outlet boundary of the model is give a zero gradient boundary condition. The zero gradient boundary condition is a Neumann condition (Jakobsen 2019) where the gradient along the face of the outlet boundary is set to zero, also known as fully developed flow (Versteeg and Malalasekera 2007). In this case the gradient between the cell immediately next to the boundary and the boundary is zero so the velocity is the same just before and just after crossing the boundary.

The inlet boundary for the laminar case is the next boundary that would need to be defined. Again for the laminar case this boundary condition will only require the pressure and velocity to be specified. The pressure at the inlet of the pipe is defined as a zero gradient boundary. This implies that the pressure gradient at this point is fully formed and does not change across the inlet boundary, the pressure gradient on one side of the inlet boundary is the same as the pressure gradient on the other side. The pressure will change along the length of the pipe but using this condition at the boundary just allows the pressure to grow to any value based on the flow conditions inside the model. The velocity boundary condition is set

to a fixed value that is uniform along the length of the boundary. The value can be specified in the x, y, and z direction but for this case, one dimensional flow in pipe, it is set only in the x direction, lengthwise along the pipe. A value equal to the desired flow velocity is set for each case.

The wall of the pipe is the last boundary to define for the laminar case. The pressure boundary is defined as a zero gradient boundary. The velocity boundary condition is set as a no slip boundary condition. This no slip boundary condition fixes the velocity along the boundary. Since the fluid is viscous it will stick to the wall at the boundary and thus have no velocity (Munson et al. 2009). Table 4.4 gives the boundary conditions for each boundary for the laminar cases.

Table 4.4 Laminar boundary conditions

Boundary	Pressure	Velocity
Inlet	Zero Gradient	Fixed Value
Outlet	Fixed Value	Zero Gradient
Wall	Zero Gradient	No Slip

4.3.2 Turbulent Cases

The three different boundaries for the model, starting with the outlet, show that both the pressure and velocity terms are the same as in the laminar flow. The difference is that initial conditions for the turbulent kinetic energy k, turbulent dissipation rate ω, and the turbulent kinematic viscosity ν_t. The boundary condition for the turbulent kinetic energy is set to zero gradient as the flow is expected to be fully developed at the outlet of the pipe. The turbulent dissipation rate is set to zero gradient at the outlet of the pipe as well due to the expected fully developed flow. The turbulent kinematic viscosity is set to a calculated value and given an initial value of zero. This calculated value boundary condition tells the solver that the value can be calculated from other known values at the boundary. Equation 4.10 shows how the turbulent kinematic viscosity is calculated.

$$\nu_t = C\frac{k^2}{\epsilon} \tag{4.10}$$

At the inlet, the pressure and velocity boundary conditions are again set the same as in the laminar case. A fixed value for the inlet velocity being assigned in the x direction based on the flow velocity that is desired. The turbulent kinetic energy is set to a fixed initial value based on the calculated value for the desired flow velocity based on Equation 4.11 where U is the velocity being simulated.

$$k = \frac{3}{2}(UI)^2 \tag{4.11}$$

$$I = 0.16Re^{-\frac{1}{8}} \tag{4.12}$$

The turbulent dissipation rate is given a boundary condition of a fixed initial condition as well with the value assigned calculated by Equation 4.13 for the desired flow velocity to be modeled.

$$\omega = \frac{\sqrt{k}}{l} \tag{4.13}$$

$$l = 0.0388D \tag{4.14}$$

The turbulent kinematic viscosity is again set to a calculated value based on Equation 4.10.

The boundary conditions get a little more complicated for the wall boundary. The pressure and velocity are set the same as in the laminar case. The turbulent kinetic energy is set to a fixed value of zero meaning that there is no velocity at the wall therefore zero kinetic energy at the wall. The turbulent dissipation rate is set to a boundary condition of omega wall functions. This omega wall function sets a constraint on the turbulence specific dissipation and is calculated by Equation 4.15 where ω_{vis} is the ω in the viscous region and ω_{log} is the ω in the logarithmic region (NEXTfoam 2017). The turbulent dissipation rate is given an initial condition the same as the inlet condition. This wall function is used even though the model was meshed to allow for a y^+ value of one. The omega wall function allows for the switching between the viscous and log-law region value based on the y^+ value for that cell.

$$\omega = \sqrt{\omega_{vis}^2 + \omega_{log}^2} \qquad \textbf{4.15}$$

The turbulent kinematic viscosity is set with a boundary condition of ν_t low Reynolds number wall function. This wall function assigns the turbulent kinematic viscosity a value of zero and allows access to a function to calculate y^+ (NEXTfoam 2017). Table 4.5 gives the boundary conditions for all of the boundaries in the turbulent cases.

Table 4.5 Turbulent boundary conditions

Boundary	Pressure	Velocity	Turbulent Kinetic Energy	Turbulent Dissipation Rate	Turbulent Kinematic Viscosity
Inlet	Zero Gradient	Fixed Value	Fixed Value	Fixed Value	Calculated
Outlet	Fixed Value	Zero Gradient	Zero Gradient	Zero Gradient	Calculated
Wall	Zero Gradient	Fixed Value	Fixed Value	Omega Wall Function	ν_t Low Re Wall Function

4.3.3 Two-Phase Cases

Similar to the laminar and turbulent cases the two-phase case will need to set boundary conditions for each of the variables calculated by the OpenFOAM solver. The variables remain mostly the same as the turbulent case with two changes: 1) the pressure variable becomes p_rgh which is the pressure minus the hydrostatic component and 2) there is an addition of a fluid fraction variable alpha. Starting at the outlet again the pressure is given a boundary condition of p_rgh pressure which is the same as the fixed value in the laminar and turbulent cases, this value is given an initial condition of zero. Instead of the value being set to zero for all time steps it is calculated based on Equation 4.16 (NEXTfoam 2017).

$$p_r gh = p - \rho g(h - hRef) \qquad \textbf{4.16}$$

The velocity boundary condition becomes a pressure inlet outlet velocity. This pressure inlet outlet velocity condition allows for two different boundary conditions based on the direction of flow. If the flow is out of the domain, a zero gradient boundary condition is imposed and if it is into the domain then the velocity is obtained from the patch-face normal component of the internal-cell value (NEXTfoam 2017). Since the flow at the outlet in this model is always out of the domain a zero gradient condition is applied. Both the turbulent kinetic energy and turbulent dissipation rate are given a zero gradient boundary condition. The turbulent kinematic viscosity is given a calculated boundary condition the same as the turbulent case. At the outlet the fluid volume fraction term, alpha, is given an inlet outlet boundary

condition. This inlet outlet condition allows for a generic outflow condition with inflow allowed for the case of return flow (NEXTfoam 2017). An inlet value for reversed flow is required and is set to a value of zero, this condition sets flow back into the domain as 0.0% oil and 100.0% air allowing for easy identification of and backflow at the start of the model.

The inlet p-rgh variable is set with a fixed flux pressure boundary condition, this condition sets the pressure gradient so that the flux on the boundary is defined by the velocity boundary condition (NEXTfoam 2017) and is given an initial condition of zero. The inlet turbulent kinetic energy and turbulent dissipation rate are given a fixed value boundary condition and set to an initial condition of one instead of the calculated values from the turbulent case since the pipe is initially filled with oil. The inlet turbulent kinematic viscosity is set with a boundary condition of calculated similar to the turbulent cases.

Since the model is only for the test area of the original experiment then the flow as it enters into the model needs to already be in a two-phase flow regime. In order for this to happen the air and the oil mixture needs to be separated based on their holdup values at the inlet and the velocities need to be different for each phase. Holdup is the fraction of the cross-sectional area occupied by each phase. The first step in separating these two flow velocities is to calculate the area of the pipe based on the holdup value. Equation 4.17 was used to calculate the area of the pipe for each phase independently (M.O.R. 2011).

$$A = r^2 \cos^{-1}\left(\frac{r-h}{r}\right) - (r-h)\sqrt{2rh-h^2} \qquad \textbf{4.17}$$

In this case h is the liquid holdup value from the work that Hulsurkar (2017) performed. Since the origin of the model is based at the center of the pipe, heights above the center is positive along the y-axis and heights below the center is negative along the y-axis. The heights used in the boundary conditions are either positive or negative based on the actual liquid holdup, a holdup of 50-percent would result in a height of zero being the input for the boundary condition. Once the area of the pipe was known then the velocity of the fluid in that area could be calculated. The superficial velocity of a fluid in a multi-phase flow environment is given as the volumetric flow rate divided by the area that the fluid takes up (Shoham 2006). Since Hulsurkar (2017) had different inlets for the oil mixture and the air the velocities that were measured would be the velocity of the fluid in a full size pipe. Using this velocity and multiplying it by the area of the full pipe will result in the volumetric flow rate. Dividing the volumetric flow rate by the area calculated from Equation 4.17 would result of in the superficial velocity of the fluid in the test area based on the holdup reported. These calculated velocities were used as the inlet velocity for both the oil mixture and the air into the system.

There are no built in boundary conditions in the OpenFOAM software that allow for two different fluids to flow though one inlet at two different velocities. Since the OpenFOAM software is open source a developer had programed an add-in function that will allow for this feature. The groovy boundary condition is a mixed boundary condition where the value, gradient, and value function is specified as an expression instead of a field (OPENFoam-Wiki 2015). The groovy boundary condition requires a value expression as is shown in Figure 4.5.

```
boundaryField
{
    inlet
    {
        type            groovyBC;
        valueExpression "(pos().y < -0.0035492) ? vector(0.78517, 0, 0) : vector(1.34322, 0, 0)";
    }
```

Figure 4.5 Groovy boundary condition syntax

The first item in the expression is a function that is predefined in the code as pos().y < -0.0035492. This part of the expression states that when the position along the y-axis is less than -0.0035492 then perform the next step in the expression which is to set the velocity to the vector (0.78517, 0, 0) or apply an inlet velocity of the fluid to 0.78517-m/s along the x-axis. If the position is not less than the given value then the expression will set the velocity to a value given in the last statement, 1.34322-m/s along the x-axis. A similar expression is generated for the oil volume fraction however when the statement is true then the inlet volume fraction is set to one for 100.0% oil and when it is false the inlet volume fraction is set to zero for air which is 0.0% oil.

The wall boundary is set with similar boundary conditions to the turbulent case. The p-rgh variable is again set to a fixed flux pressure and the velocity variable is set to a fixed value of zero since there would be flow fluid velocity at the wall. The turbulent kinetic energy and turbulent dissipation rate are all set the same as in the turbulent case, with a fixed value of zero and omega wall functions respectively. The turbulent kinematic viscosity is set with a boundary condition of ν_t k wall function which provides a turbulent kinematic viscosity based on the turbulent kinetic energy (NEXTfoam 2017). The oil volume fraction variable, alpha, is set to a zero gradient boundary condition as the oil volume fraction should be similar from cell to cell. Table 4.6 gives the boundary conditions for all of the boundaries for the two-phase cases.

Table 4.6 Two-phase boundary conditions

Boundary	Pressure	Velocity	Turbulent Kinetic Energy	Turbulent Dissipation Rate	Turbulent Kinematic Viscosity	Fluid Volume Fraction
Inlet	Fixed Flux Pressure	groovyBC	Fixed Value	Fixed Value	Calculated	groovyBC
Outlet	prgh Pressure	Pressure Inlet Outlet Velocity	Zero Gradient	Zero Gradient	Calculated	Inlet Outlet
Wall	Fixed Flux Pressure	Fixed Value	Fixed Value	Omega Wall Function	ν_t k Wall Function	Zero Gradient

4.4 Sensitivity Analysis on Mesh Size

4.4.1 Laminar flow

After the CAD model was meshed properly and the boundary condition were defined and the models were ready to be run through the solver. The first step was to determine how fine of a mesh would be needed to capture the physics of the problem. Four different mesh files were generated each with an increasing number of cells per slice and the total number of cells per mesh is shown in Table 4.7.

Table 4.7 Mesh setup for sensitivity analysis

Mesh	Element Size [m]	Nodes Per Slice	Total Nodes
Rough	0.005	1,058	423,729
Coarse	0.0025	2,258	904,329
Medium	0.001	6,722	2,692,161
Fine	0.0005	17,042	6,825,321

The rough mesh was run first and it was determined that there were not enough nodes for a suitable model to be run on this mesh. Figure 4.6 shows a zoomed in portion of the nose of the velocity profile for the rough mesh. The steps for each of the nodes in the mesh are clearly visible in the velocity profile and for this reason the decision was made to drop the rough mesh from the options in the mesh analysis.

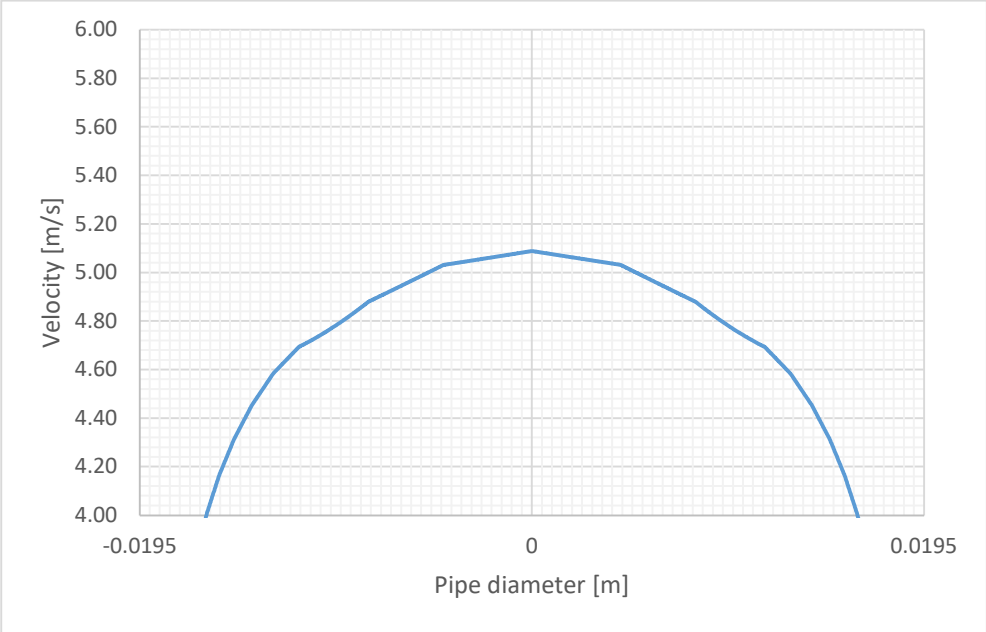

Figure 4.6 Rough velocity profile zoomed in

The laminar flow pressure gradients were accurate, regardless of the roughness of the mess. For the flow velocity of 0.21-m/s the analytical pressure drop was calculated using the Darcy-Weisbach equation for laminar flow, Equation 4.18. This pressure drop was compared to the pressure drop that were obtained from the simulation. Table 4.8 shows the tabulated results with the error percentage and Figure 4.7 shows an overlay of the three different mesh roughness and the analytical Darcy-Weisbach value. The results were well within any reasonable window for error.

$$\frac{\Delta P}{L} = \frac{128}{\pi}\frac{\mu Q}{D^4} \qquad 4.18$$

Table 4.8 Laminar pressure drop results from sensitivity analysis

Mesh	OpenFOAM Pressure Drop [Pa/m]	Analytical Pressure Drop [Pa/m]	% Error [%]
Coarse	1008.836	1009.197	0.04%
Medium	1008.418	1009.197	0.08%
Fine	1008.920	1009.197	0.03%

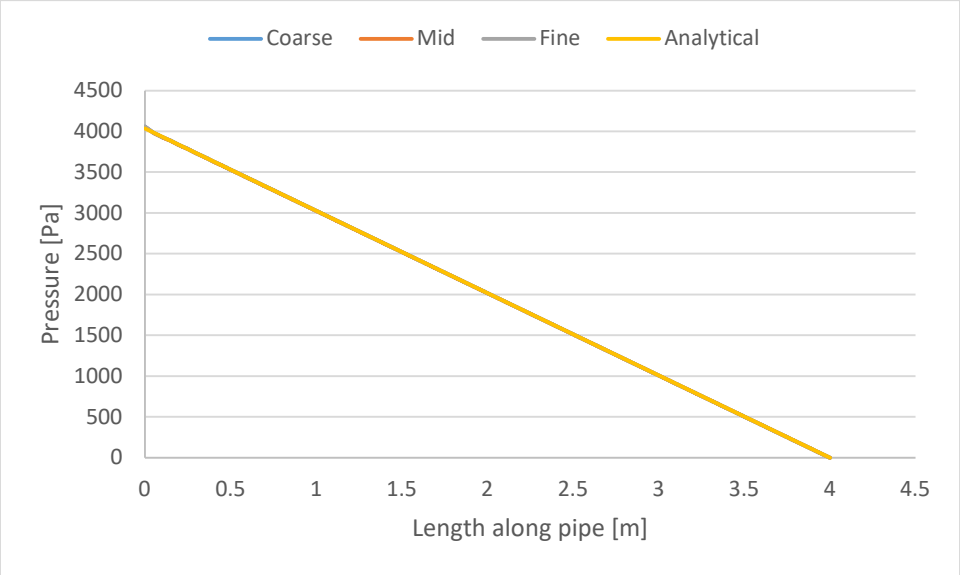

Figure 4.7 Laminar along pipe from sensitivity analysis

The velocity profile was also examined to determine if the roughness of the mesh affects the results. Equation 4.19 was used to calculate the analytical laminar velocity profile (Guo), where U_m is given as the centerline velocity and is twice the average velocity for the given model.

$$v = U_m\left(1 - \frac{r}{R}\right)^2 \qquad 4.19$$

The results are shown in Figure 4.8 and Table 4.9 for the mesh comparison and show all three of the mesh options as equally valid for use in the model.

Table 4.9 Laminar velocity profile results from sensitivity analysis

Mesh	OpenFOAM Centerline Velocity [m/s]	Analytical Centerline Velocity [m/s]	% Error [%]
Coarse	0.4200	0.4200	0.00%
Medium	0.4199	0.4200	0.03%
Fine	0.4194	0.4200	0.15%

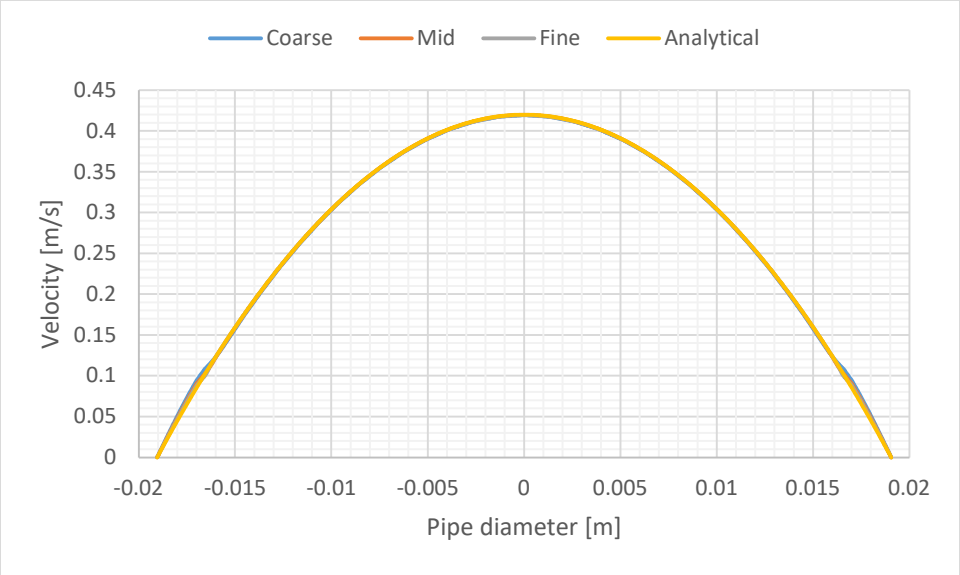

Figure 4.8 Laminar velocity profile results from sensitivity analysis

4.4.2 Turbulent

The same process was performed for the turbulent flow velocity of 4.4-m/s and the three mesh options for the sensitivity analysis. The Darcy-Weisbach equation for turbulent flow, Equation 4.20, was used to calculate the analytical pressure drop along the length of the pipe. Equation 4.21 show how the Blasius correlation for the friction factor was calculated.

$$\frac{\Delta P}{L} = f\frac{\rho}{2}\frac{u}{D} \tag{4.20}$$

$$f = 0.316Re^{-\frac{1}{4}} \tag{4.21}$$

Table 4.10 and Figure 4.9 show the results of the sensitivity analysis for the pressure drop calculations. As the mesh density increases the results get worse. For the finest mesh an almost 40.0% error was observed between the simulation value and the analytical value.

Table 4.10 Turbulent pressure drop results from sensitivity analysis based on $1*10^{-5}$ residuals

Mesh	OpenFOAM Pressure Drop [Pa/m]	Analytical Pressure Drop [Pa/m]	% Error [%]
Coarse	8.547	8.551	0.04%
Medium	7.658	8.551	10.43%
Fine	5.145	8.551	39.83%

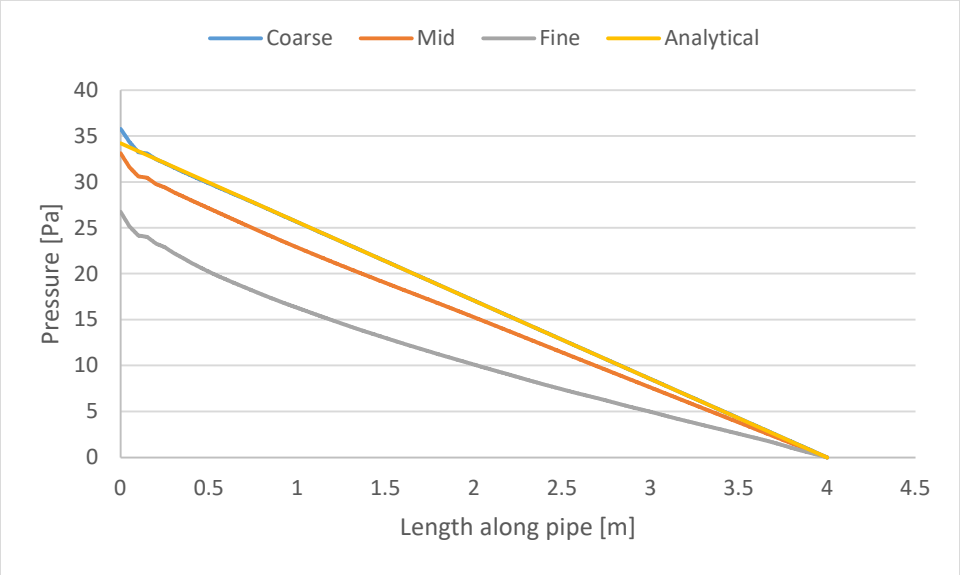

Figure 4.9 Turbulent along pipe from sensitivity analysis based on $1*10^{-5}$ residuals

This behavior goes against all logic in that the more refinement a model has the more accurate the results should be. Examining how the model is set up there are some options as to what could cause these results. The first aspect that should be questioned is the residual level that the equations are solved to. Residuals are the difference between the current solution for a given variable and the previous iteration solution. It can be thought of simply as if the initial solution at iteration one is given a value of 2 and the solution at iteration two is given a value of 1.5 then the residual between the two solutions would be 0.5. This is continued until a level is reached that is selected prior to starting the models.

The initial residuals that were selected for the sensitivity analysis were $1*10^{-5}$. The results suggests that this value was not refined enough for the medium and fine mesh. A second set of models was run with a residual level of $1*10^{-10}$ on all three models to determine if this was the cause of the error.

Table 4.11 and Figure 4.10 show the results of the second run with the new residual values.

Table 4.11 Mesh pressure drop results based on $1*10^{-10}$ residuals

Mesh	OpenFOAM Pressure Drop [Pa/m]	Analytical Pressure Drop [Pa/m]	% Error [%]
Coarse	8.379	8.551	2.0%
Medium	8.724	8.551	2.0%
Fine	8.728	8.551	2.1%

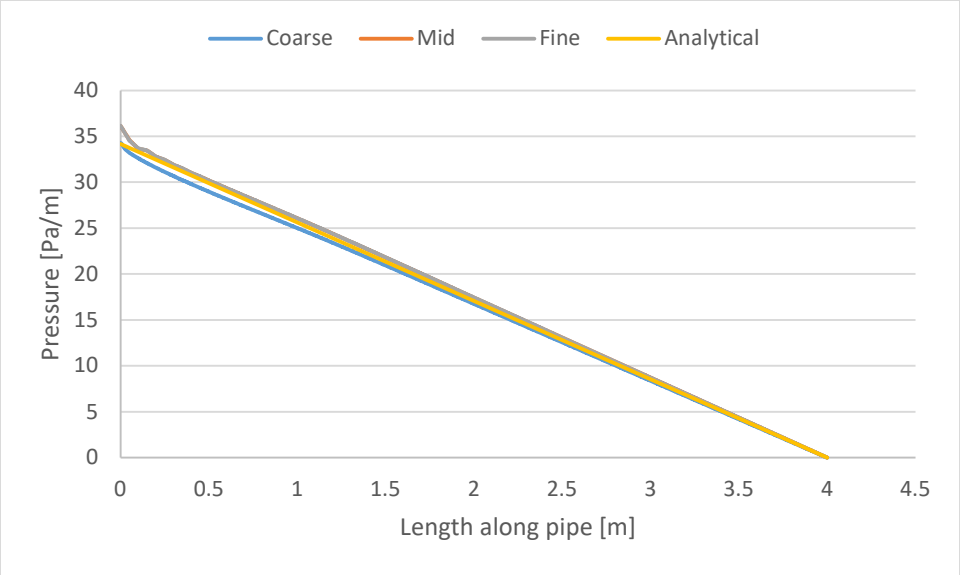

Figure 4.10 Turbulent along pipe based on 10^{-10} residuals

These values show that the mesh is adequate for the models being run as long as the residual levels are set to an appropriately small value. There is more to consider when running numerical models on computer simulations and one of the most important factor is the amount of CPU time that is required to run a given model.

Table 4.12 gives the results for the run time for the coarse, medium, and fine models for both residual levels.

Table 4.12 CPU hours per model

Model	Time [hours]	CPU's	CPU Hours
Coarse @ $1*10^{-5}$ residuals	0.086	48	0.002
Medium @ $1*10^{-5}$ residuals	0.271	48	0.006
Fine @ $1*10^{-5}$ residuals	1.730	48	0.036
Coarse @ $1*10^{-10}$ residuals	3.080	48	0.064
Medium @ $1*10^{-10}$ residuals	108.395	48	2.258
Fine @ $1*10^{-10}$ residuals	124.729	48	2.599

Table 4.12 shows that the more refinement a mesh has the more CPU time will be required for each run. Due to the long run times of the medium and fine mesh and the requirement of having a residual level of $1*10^{-10}$ to obtain results if the decision was to be made solely on the pressure drop results the coarse mesh would be used for the two-phase models.

The turbulent velocity profile is a little more problematic to examine due to the unexplained nature of turbulent flow. Turbulent flow is not fully explained by modern physics and for this reason there are numerous equations for the velocity profile inside of a pipe. The two correlations that are used most are the power law and the logarithmic velocity profile (Hinze 1975). The power law velocity profile is given by Equation 4.22 (Munson et al. 2009) where V_c is the centerline velocity and calculated by Equation 4.23.

$$\frac{\bar{u}}{V_c} = \left(1 - \frac{r}{R}\right)^{\frac{1}{n}} \quad \textbf{4.22}$$

$$V_c = u\left(1 + 1.326\sqrt{f}\right) \quad \textbf{4.23}$$

Figure 4.11 shows how the exponent, n, is derived based on the Reynolds number and is given by Equation 4.24 (Munson et al. 2009).

$$n = -1.7 + 1.8\log(Re) \quad \textbf{4.24}$$

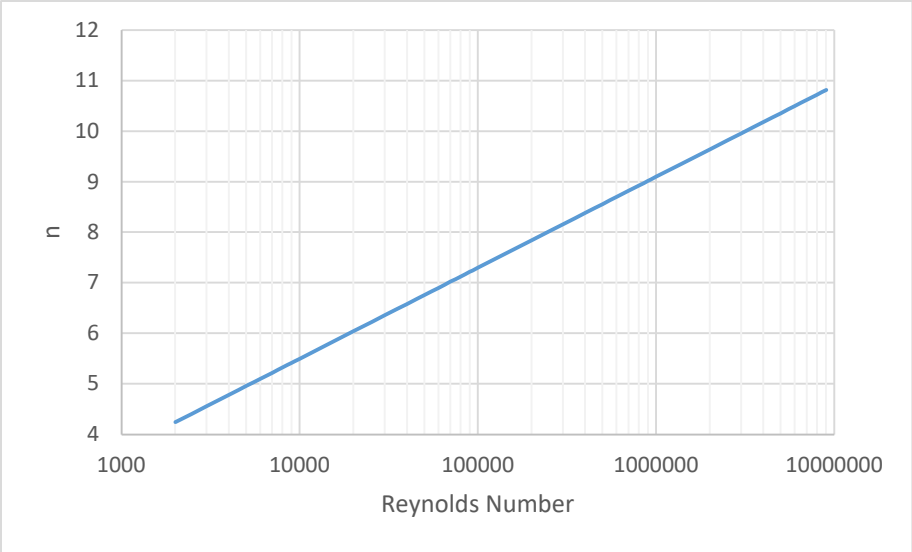

Figure 4.11 n-exponent as a function of Reynolds number (Munson et al. 2009)

Most turbulent flows are best described by an exponent value of 7 (Munson et al. 2009). The Reynolds number for the fluid velocity of 4.4-m/s is approximately 11500 and an exponent value of 5.608 is calculated based on Figure 4.11. The logarithmic approximation of the turbulent velocity profile is given by Equation 4.25 (Munson et al. 2009) where u^* is given by Equation 4.26.

$$\frac{\bar{u}}{u^*} = 2.5\ln\left(\frac{yu^*}{v}\right) + 5.0 \quad \textbf{4.25}$$

$$u^* = u\sqrt{\frac{f}{8}} \tag{4.26}$$

Figure 4.12 shows the comparison of the power law, logarithmic, and the simulation results based on the coarse mesh.

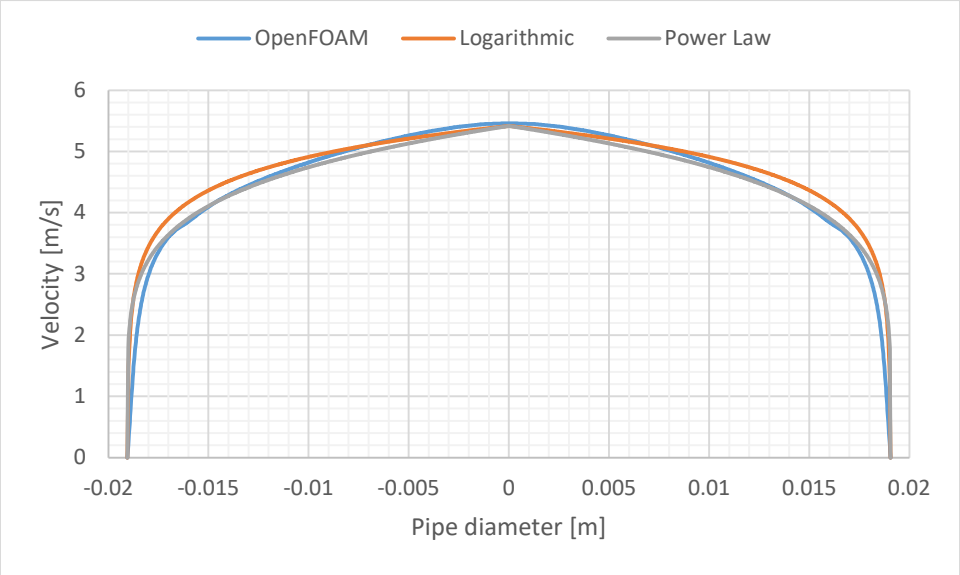

Figure 4.12 Turbulent velocity profile comparison with analytical values

Since both the power law and logarithmic approximations use the same equation for the centerline velocity, they converge at the centerline but throughout most of the pipe they are shown to be different. The power law profile better fits the simulated velocity profile for the majority of the velocity profile and fits well in the near wall region. Since the near wall region contributed the most to the velocity profile the power law profile was used in the comparison to determine the mesh roughness.

Figure 4.13 shows the velocity profiles using coarse, medium, and fine mesh compared to the power law velocity profile. **Error! Reference source not found.** shows the percentage of error from the centerline velocity as compared to the analytical calculated centerline velocity.

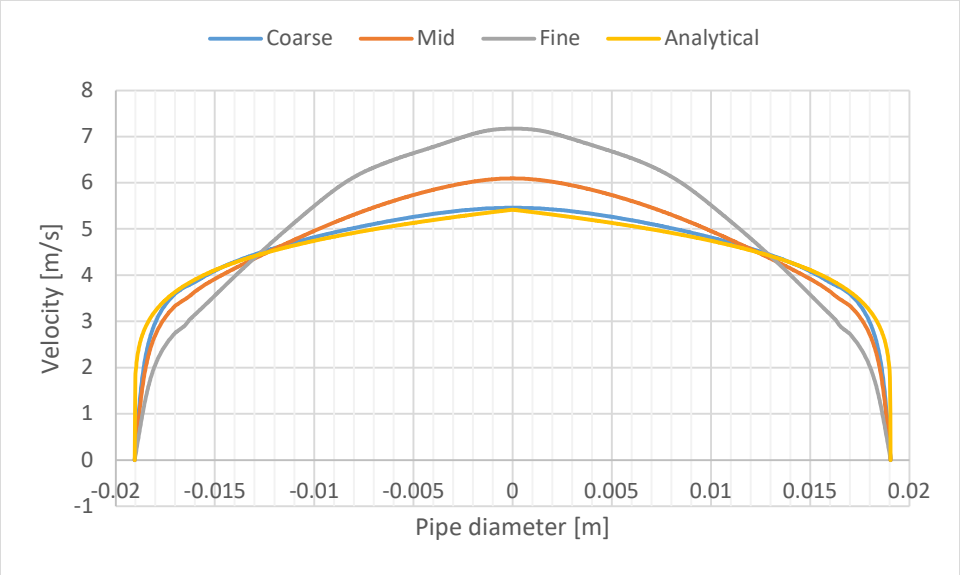

Figure 4.13 Turbulent velocity profile results from sensitivity analysis

Table 4.13 Turbulent velocity profile results from sensitivity analysis

Mesh	OpenFOAM Centerline Velocity [m/s]	Analytical Centerline Velocity [m/s]	% Error [%]
Coarse	5.4648	5.4303	0.63%
Medium	6.0981	5.4303	12.30%
Fine	7.1745	5.4303	32.12%

Similar to the pressure drop comparison, the coarse mesh has the best correlation to the analytical value and the least amount of error. The small variations in the calculated velocities in the nodes will grow quickly into larger errors between the simulated values and the analytical values as the total number of nodes increase. Since it has the best comparison to the pressure drop along the length of the pipe and the velocity profile in the pipe and because the laminar data did not show any disagreement, the coarse mesh was selected to run the two-phase models.

4.4.3 Two-phase

While the two-phase models were not run though the sensitivity analysis in the same way that the laminar and turbulent flow were it is important to note that the length wise step size of the mesh has some control over the results in the two-phase regime. Simulation results show that if the length wise step was too short then the flow pattern was not developed correctly in the pipe. Figure 4.14 shows what should be a slug type flow where the pipe is completely closed off by fluid during the slugs. The fluid level, shown in red, can be observed rising and falling in a wavy pattern but never fully closing off the pipe. Since these slugs were not forming, the pressure drop along the length of the pipe was not being calculated correctly. This model was run with a lengthwise step size of 0.05-meters.

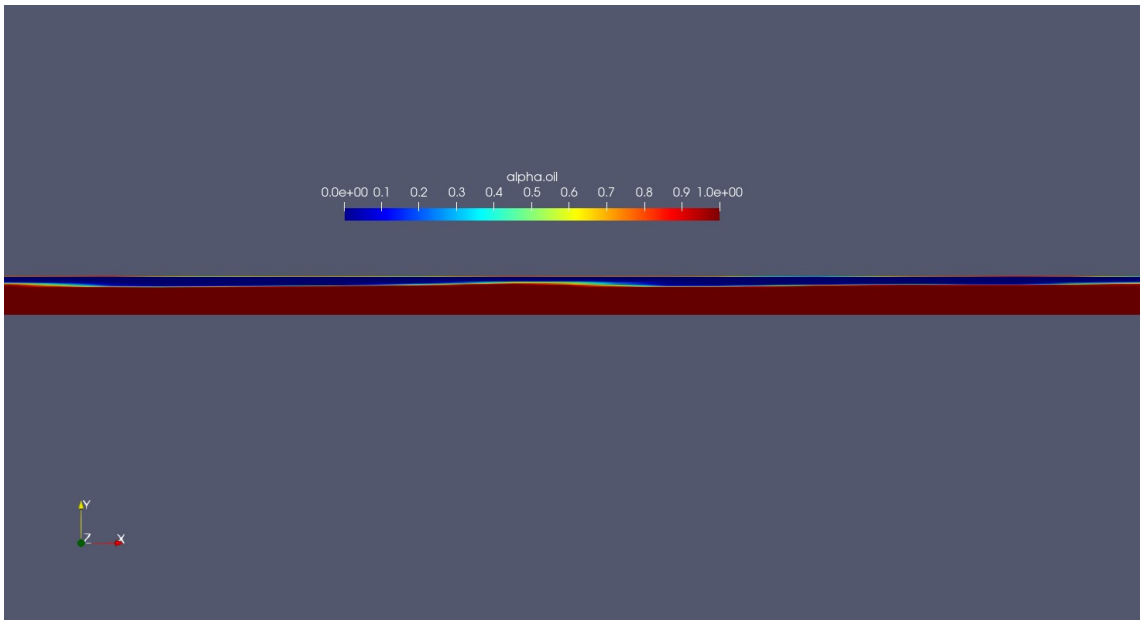

Figure 4.14 Two-phase erroneous slug flow results

The lengthwise step size was changed to 0.005-meters and the same flow velocities were run through the simulation. Figure 4.15 shows the results of this run and shows that the slugs are forming as they should in the pipe allowing for a more accurate pressure drop along the pipe.

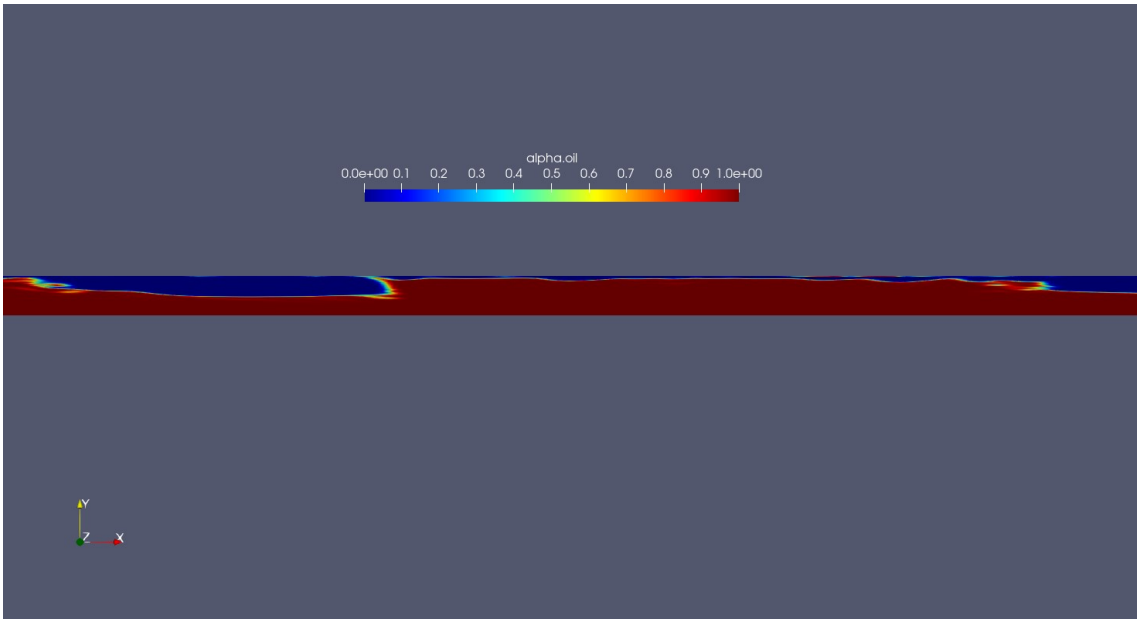

Figure 4.15 Two-phase corrected slug flow results

The increase of the length wise step in the mesh caused the models to have an increase in the total cells of ten times the original values. The total number of cells given in Table 4.7 are the correct values based on this 0.005-meter lengthwise step size. This ten times increase in node count led to a larger increase in the total run time of the models.

Fluid Properties

Since the original experimental work by Hulsurkar (2017) only showed the results for single phase oil flow of the mix2 and mix3 oils due to anomalously high differential pressure observations from mix1, it was determined that only the mix2 and mix3 oils would be used for this study and the mix1 data was not considered. The fluid properties used in this study are the same as Hulsurkar (2017) used in the experimental setup. Table 4.14 lists the pertinent fluid properties used in the simulations for air, the mix2 oil, and the mix3 oil. Analytical

Table 4.14 Simulated fluid properties

Fluid	Density [kg/m^3]	Dynamic Viscosity [kg/ms]	Kinematic Viscosity [m^2/s]
Air	1.225	1.789E-05	1.461E-05
Mix1 Oil	824	0.150	1.818E-04
Mix2 Oil	830	0.197	2.373E-04
Mix3 Oil	837	0.218	2.605E-04

5 CHAPTER FIVE: RESULTS AND DISCUSSION

5.1 1.5-inch Model

The initial model was based on the work of Hulsurkar (2017) and was built to be a 1.5-inch diameter pipe. Since the OpenFOAM software works in SI units a pipe of diameter 0.0381-meters was designed with a length of 4-meters as described in the methodology section. The course mesh was used to generate the model and a total of 2,258 nodes per slice for a total of 904,329 nodes to cover the whole length of the pipe. The pipe was represented by 400 slices. The model was first run with the heavy oil mix fluid at laminar flow velocities for a laminar validation and then run with air at turbulent rates for a turbulent validation. After the simulation model was validated the two-phase flow was run through the simulations to obtain the results and compared to experimental results from Hulsurkar (2017).

Hulsurkar (2017) provided 25 combinations of velocities for the mix2 oil and air two-phase flow that had liquid holdup values and from these rates a total of 13 experiments were picked for simulation in this study. The lowest velocity for the mix2 oil was given at 0.08-m/s and this velocity was dropped due to the distance from the median velocity of 0.43-m/s. Three two-phase combinations were dropped due to no flow regime being listed in the experimental data. This left 20 total two-phase combinations to pick from for the simulation. Of these remaining 20 two-phase combinations there were 14 unique mix2 oil velocities and 9 unique ail velocities. The lowest air velocity of 0.04-m/s was dropped due to its distance from the median air velocity of 3.31-m/s. Superficial fluid velocities are defined as the velocity that a single phase would flow if it was taking up the entire pipe (Shoham 2006). These velocities are designated with a subscript s along with L for liquid and g for gas, V_{sl} for liquid superficial velocity and V_{sg} for gas superficial velocity. Table 5.1 gives the 13 two-phase flow velocities that were selected for the mix2 oil-air combination for simulation.

Table 5.1 Mix2 flow combinations

Flow Velocity Combination	V_{sl} [m/s]	V_{sg} [m/s]
1	0.53	0.50
2	0.25	0.83
3	0.53	1.66
4	0.45	1.66
5	0.40	1.66
6	0.36	1.66
7	0.52	3.31
8	0.25	3.31
9	0.44	3.31
10	0.25	4.56
11	0.29	5.38
12	0.30	6.83
13	0.43	8.28

The same process was completed for the mix3 oil air two-phase flow combinations starting with the 16 velocity combinations that had liquid holdup values given. Since all of the oil and air flow velocities fall within in the same range as the mix2 oil-air flow velocities they were all selected in this study. Table 5.2 gives the values selected in this study.

Table 5.2 Mix3 flow combinations

Flow Velocity Combination	V_{sl} [m/s]	V_{sg} [m/s]
1	0.27	0.41
2	0.35	0.83
3	0.42	0.83
4	0.35	1.66
5	0.39	1.66
6	0.42	1.66
7	0.44	1.66
8	0.35	2.48
9	0.41	2.84
10	0.35	3.31
11	0.41	3.31
12	0.41	4.14
13	0.34	4.56
14	0.34	5.80
15	0.41	5.80
16	0.34	8.28

5.1.1 Laminar Validation

The results from the laminar validation of the model were performed with the mix3 oil flow velocities and showed an exceptional for both pressure drop and velocity profile. Figure 5.1 shows the pressure along the pipe for the median flow velocity of 0.24-m/s and shows an almost exact correlation to the analytical value. The other 12 flow velocities, listed in Table 5.3, showed a similar correlation to the analytical values. Figure 5.2 shows a comparison of the experimental and analytical pressure gradients. These values show that the OpenFOAM software, labeled as analytical on the charts, did an excellent job of matching the analytical solutions but was a little off of the experimental values. All of the value fall well within the 30% error tolerance.

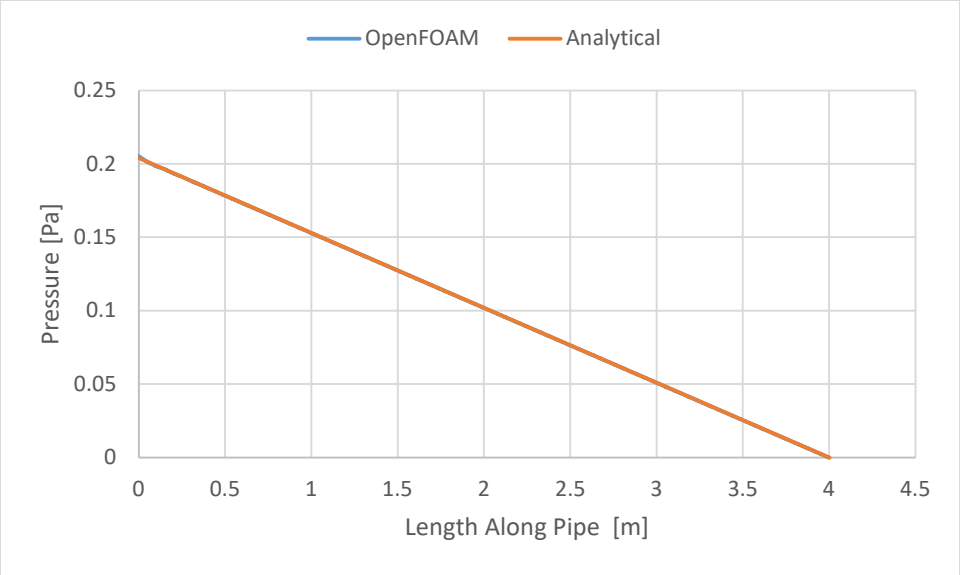

Figure 5.1 Pressure drop for laminar flow velocity #7

Table 5.3 Laminar flow velocity for 1.5-inch model mix3 fluid

Flow Velocity	Vl [m/s]
1	0.1
2	0.12
3	0.13
4	0.15
5	0.17
6	0.21
7	0.24
8	0.27
9	0.31
10	0.34
11	0.38
12	0.41
13	0.45

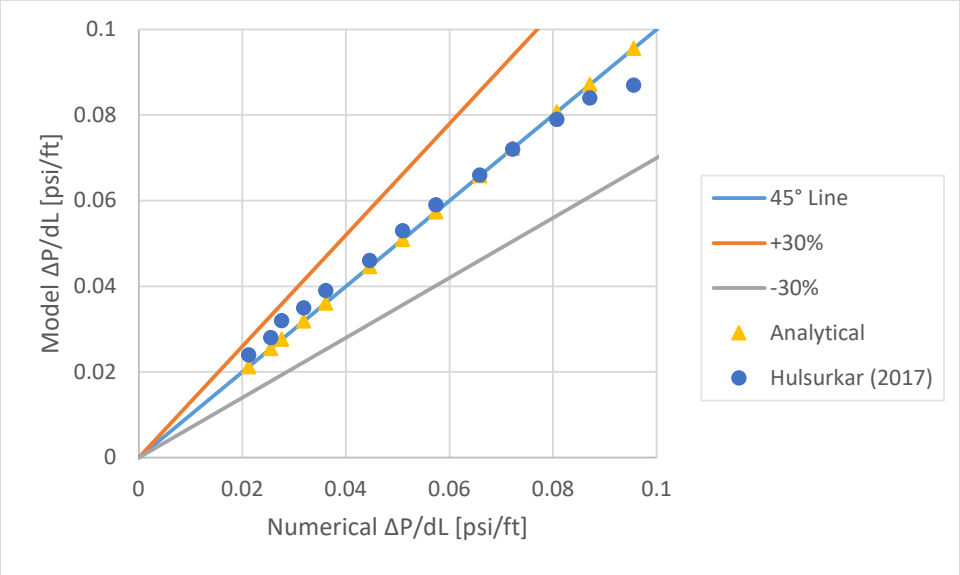

Figure 5.2 Experimental and analytical comparison of pressure drop for laminar mix3 fluid in 1.5-inch model

Figure 5.3 shows the velocity profile for the same 0.24-m/s flow velocity and shows a correlation to the analytical value with 0.04% error. The deviation that can is shown around 0.1-m/s is due to the inflation layers' transition to the center o-grid on the mesh. This small fluctuation is present on all of the velocity profiles and does not affect the pressure drop calculations so the mesh was not recalculated to attempt to eliminate it. The other 12 flow velocities showed a similar correlation to the analytical values for the velocity profile. Figure 5.4 shows the comparison between the analytical centerline velocity and the value produced by OpenFOAM. These value all fall along the 45° line and show little error similar to the pressure drop.

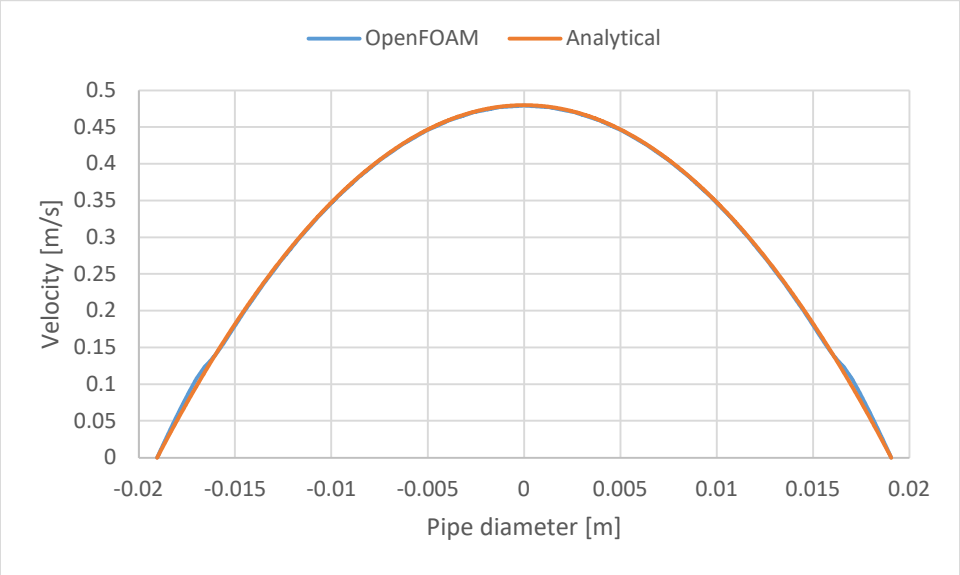

Figure 5.3 Laminar velocity profile for flow velocity #7

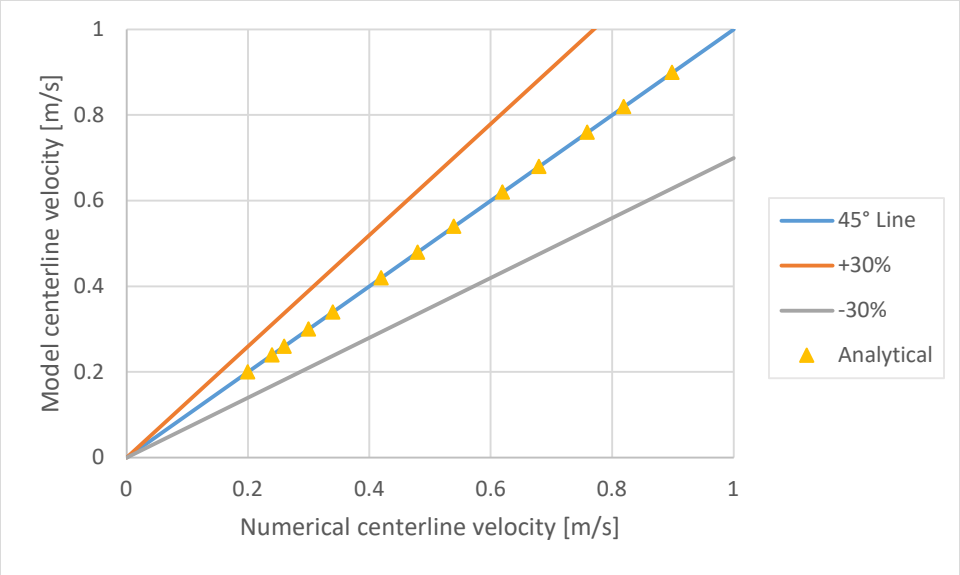

Figure 5.4 Analytical comparison of centerline velocities for laminar mix3 fluid in 1.5-inch model

The OpenFOAM software did an exceptional job of predicting the laminar flow patterns for all velocities. Since the laminar flow is so well understood from a theoretical aspect, it would be expected that any software would be able to produce the same results.

5.1.2 Turbulent Validation

From the flow velocity combinations from the mix3 oil, there were 10 unique velocities for the air in the system. Combining these 10 unique flow velocities with the two-phase mix2 air flow velocities and dropping the duplicated between the two results in 17 unique values to simulate for the turbulent validation and are shown in Table 5.4.

Table 5.4 Selected air velocities for turbulent flow validation

Flow Velocity	**1**	**2**	**3**	**4**	**5**	**6**	**7**	**8**	
Velocity [m/s]	0.04	0.10	0.31	0.41	0.05	0.83	1.24	1.66	
Flow Velocity	**9**	**10**	**11**	**12**	**13**	**14**	**15**	**16**	**17**
Velocity [m/s]	2.48	3.31	4.14	4.56	5.38	5.80	6.83	8.28	9.11

Not all of the air flow velocities are in the turbulent range, based on the pipe diameter and the viscosity of air. A Reynolds number of 2100 being the boundary between laminar and turbulent flow shows all values less than a velocity of 0.805-m/s would be in the range of laminar flow. There were 5 flow velocities from the group in this range and they were simulated using the laminar flow conditions. These 5 laminar flow velocities showed the same exceptional correlation as the oil flow velocities did as is shown in Figure 5.5 for the pressure drop and Figure 5.6 for the centerline flow velocities.

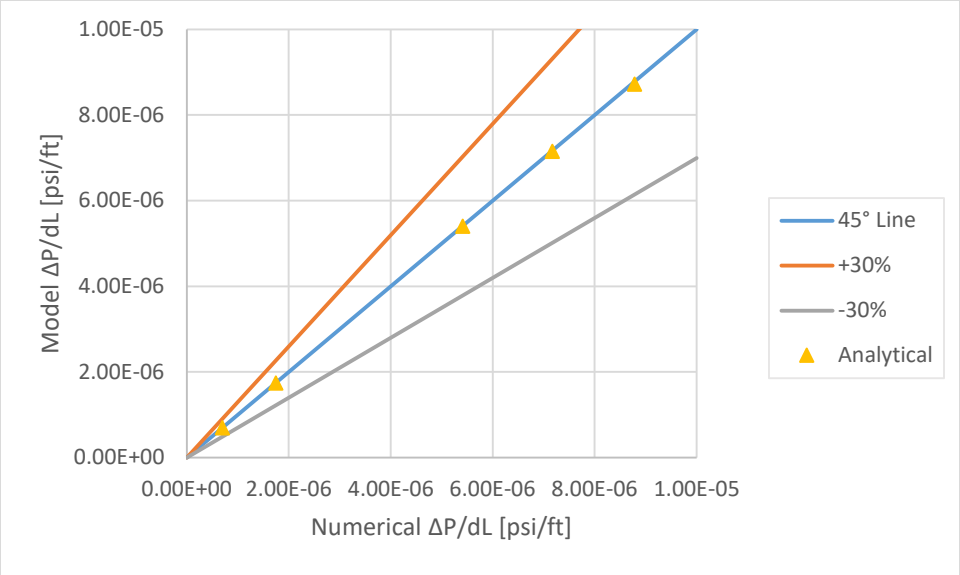

Figure 5.5 Analytical comparison of pressure drop for laminar air in 1.5-inch model

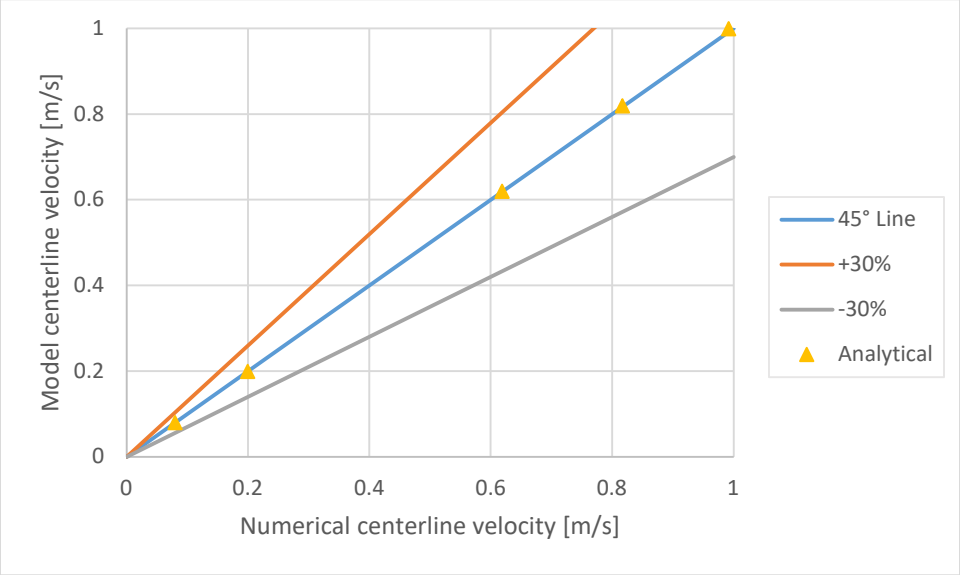

Figure 5.6 Analytical comparison of centerline velocities for laminar air in 1.5-inch model

The remaining 12 flow velocities were all simulated using the turbulent conditions laid out in the methodology section. As these flows became more turbulent the flow started to show a better correlation over the less turbulent flows. These less turbulent flows are in a region that is transitioning from laminar to turbulent flow. This region is generally described as Reynolds number between 2100 and 4000. Both the lower and upper range for the Reynolds number in this region is different depending on which source is examined. For this study it is fairly evident that any run for turbulent flow larger than a Reynolds number of 2100 and smaller than approximately 4400 falls within this range.

Figure 5.7 shows the velocity profile for flow velocity number 6 at 0.83-m/s. The velocity profile shows that the velocity is over predicted throughout the entire diameter of the pipe. A centerline velocity of 1.258-m/s is 17.88% higher than the predicted centerline velocity of 1.067-m/s. This velocity profile also shows a more parabolic shape than a turbulent profile should.

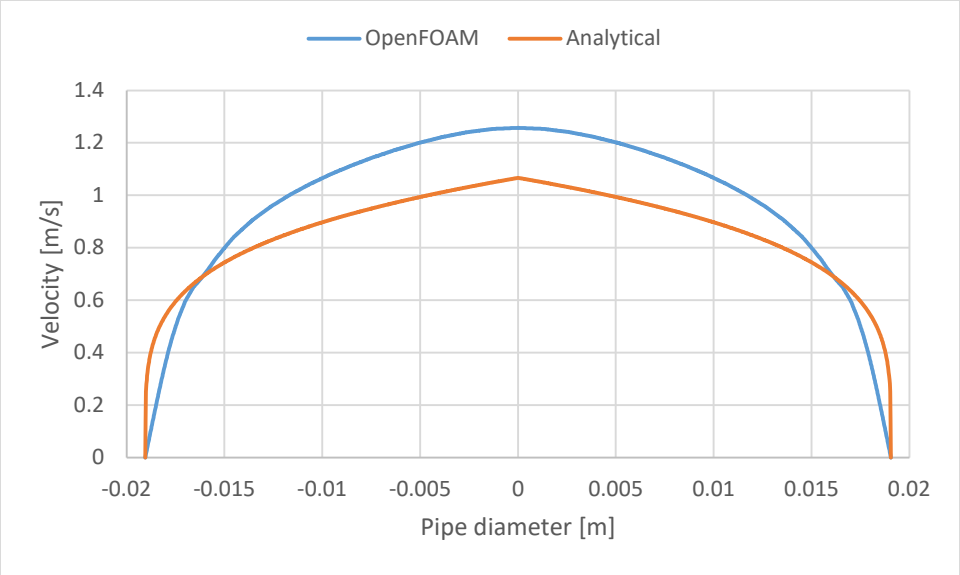

Figure 5.7 Turbulent velocity profile for turbulent flow velocity #6

The pressure drop along the pipe shows a 2.71e-05-psi/ft pressure drop along the length. This is 19.31% higher than the predicted pressure drop of 2.27e-05-psi/ft. It is possible to change the turbulent model used for the simulation or some of the properties of the k-ω flow model, however, the purpose of this study is to find a single model that can be used to simulate the heavy oil-air two-phase flow in different size pipes so changing the model based on a single flow velocity would defeat this purpose. The largest error in the pressure drop, 19.31% for the 0.83-m/s flow velocity, shows the difference in pressure drop over 10,000-ft of pipe is less than 0.05-psi and it was determined that these errors are acceptable.

These gas velocities are on the low side for what is considered normal for calculating pressure drop along a pipe and result in lower flow rates for the fluid. For this 1.5-inch diameter pipe and the velocity of 9.11-m/s it is calculated that there is a flow rate of 31,690-SCFD, which is extremely low for a throughput on a pipeline. These pressure drop values appear to be low but in reality due to the extremely low flow rates they are close to what would be expected. For example using a Weymouth equation (Ikoku 1992), Equation 5.1 where T_b is the base temperature, p_b is the base pressure, p_1 is the inlet pressure, p_2 is the outlet pressure, D is the diameter of the pipe, γ_g is the gas gravity, L is the length of the pipe, T is the average flowing temperature and z is the gas deviation factor, and the properties given in

Table 5.5 a throughput for a gas pipeline can be calculated.

$$q_h = 18.062 \frac{T_b}{p_b} \left[\frac{(p_1^2 - p_2^2) D^{16/3}}{\gamma_g \bar{T} L \bar{z}} \right]^{0.5} \quad \textbf{[5.1]}$$

Table 5.5 Input parameters for Weymouth equation

T_b	520 °R		γ_g	0.6
p_b	14.7 psi		T	520 °R
p_1	400 psi		L	100
p_2	200 psi		z	0.95
D	12.09 in			

The results for the inputs in

Table 5.5 give a throughput of 989,859-CFH for the given pipeline with a 200-psi drop over a 100-mile length. These pressure drop value narrowed down to psi/ft would results in 3.79e-04-psi/ft which are not that much larger than the pressure drop values that are being examined in a much smaller pipe in this study.

Figure 5.8 shows the pressure drop along the length of the pipe and the turbulent entry length can be observed clearly at the beginning of the pipe. The pressure profile from the simulation shows steady increase over the analytical value along the length of the pipe and there is no point where it jumps drastically, apart from the turbulent entry length area.

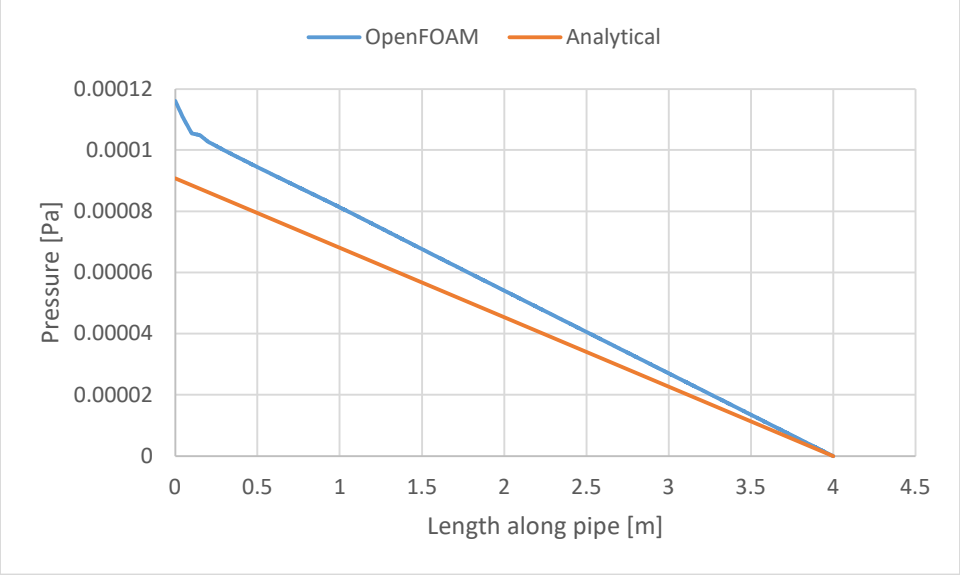

Figure 5.8 Pressure drop for turbulent flow velocity #6

Back calculating the average velocity from the centerline velocity of 1.258-m/s give an average velocity of 0.978-m/s. Using this value the pressure drop along the pipe can be calculated to be 3.02e-05-psi/ft. This value is 11.6% higher than the value that was determined by the simulation. This shows that the simulation is not predicting the velocity profile correctly. Since the velocity profile is not being calculated correctly, the pressure drop along the pipe is not being calculated correctly either.

Performing the same process for the other two flow velocities that are in the transition region shows that for the 1.24-m/s velocity the centerline velocity from the simulation was 31.3% higher than the analytical value. The pressure drop for this flow velocity was only 3.53% higher than the analytical value. For the 1.66-m/s velocity the centerline velocity was 2.977-m/s which is 42.13% higher than the predicted value of 2.094-m/s. The pressure drop for this flow velocity was 12.59% lower than the expected value.

The remaining 9 flow velocities all showed a good correlation with the pressure drop with a maximum error of 2.61% for the lowest velocity of 2.48-m/s. As the velocities start to increase the error between the simulated values and the calculated values decreases until the velocities start to reach the higher values simulated. These higher flow velocities are moving the fluid at a rate that is more than double the length of the pipe in less than one second. If the lateral mesh density is increased, then these values would fall into a lower percentage of error similar to the other values. The larger lateral density in the model would cause the two-phase models to run for longer and it was deemed unnecessary since the difference along 10,000-ft of pipe is around 0.25-psi. Figure 5.9 shows the comparison between the

OpenFOAM generated pressure and the analytical pressure drop for the flow velocities 6, 7, and 8 due to the scaling on the chart. These three pressure drop values show some fluctuation from the 45° line but are will within the 30% error limits.

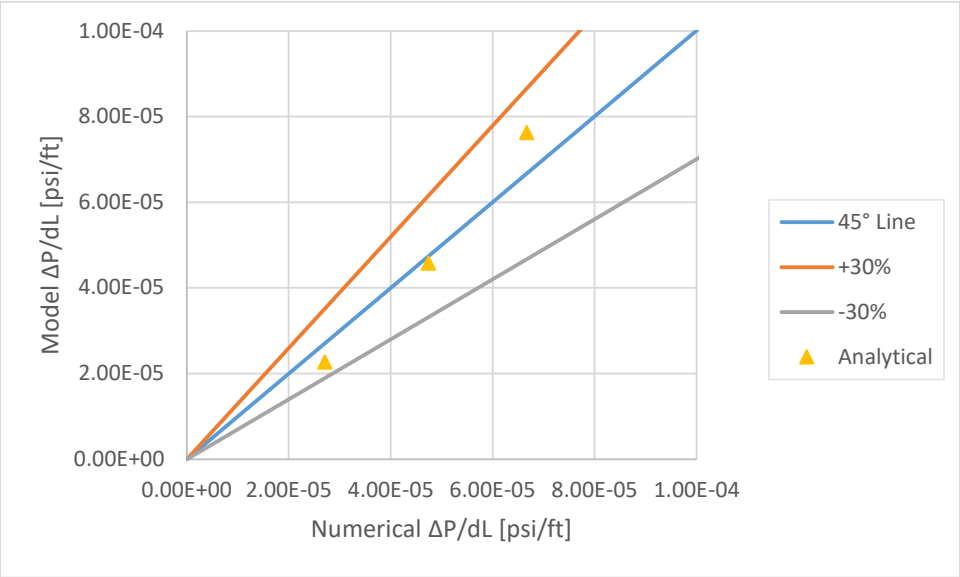

Figure 5.9 Analytical comparison of pressure drop for turbulent air flow velocities 6, 7, and 8 in 1.5-inch model

Figure 5.10 shows the comparison between the OpenFOAM generated values and the analytical pressure drop for the remaining turbulent flow velocities. These values show a good comparison and fall close to the 45° line.

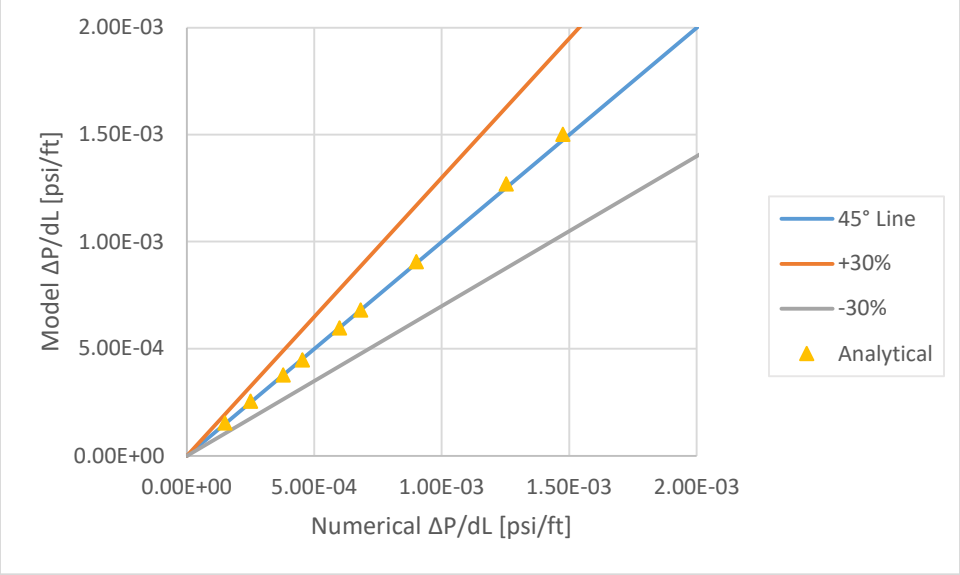

Figure 5.10 Analytical comparison of pressure drop for turbulent air in 1.5-inch model

The flow velocity centerline values are a better match in the higher 9 velocities in this study. The first two flow velocities after the transition zone, 2.48-m/s and 3.31-m/s, show a higher percentage error that is closer to the results from the transition zone even though the pressure drop values show a better correlation than do the three transition zone flow velocities. Figure 5.11 shows a comparison between the

OpenFOAM generated centerline velocities and the analytical centerline velocities. There is a strong correlation between the percentage of error in the centerline velocity and the percentage error in the resulting pressure drop.

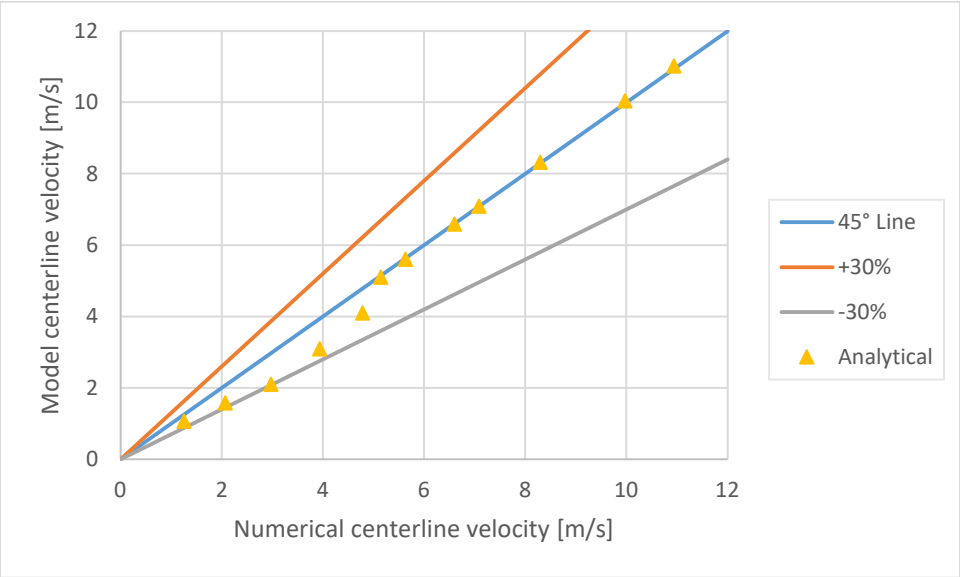

Figure 5.11 Analytical comparison of centerline velocities for turbulent air in 1.5-inch model

The results of the turbulent flow verification show the difficulty in predicting turbulent flow that still exists. Due to the low viscosity of the air being simulated these pressure drop values are not large and will cause the percentage of error to be larger with a smaller deviation in values. Since these values are not appreciable compared to the overall pressure drop in the system for the laminar oil flow they have been deemed acceptable. It would be possible with a more refined mesh and differing flow properties to better predict the pressure drop along the pipe for these turbulent flow velocities but that is not the intent of this study.

5.1.3 Two-phase Results

Once the laminar and turbulent validation was completed the two-phase flow simulations were started. These simulations were based on the flow velocity combinations picked from the original work performed by Hulsurkar (2017). As stated in in the laminar and turbulent validation sections these values were selected based on the availability of liquid holdup values and flow pattern identification. The pressure drop and liquid holdup values were examined for each of the two-phase scenarios. The original work done by Hulsurkar (2017) had calculated the expected Beggs and Brill pressure drop and liquid holdup values for each of these scenarios as well so this data will be compared to the values presented in his work as well as the values generated in his experiments.

5.1.3.1 Mix2 Results

The mix2 oil flow velocities were sorted by the gas velocity from lowest to highest and the simulations were run. Table 5.6 shows the flow velocity combinations along with the number assigned to each one for ease of description.

Table 5.6 Mix2 two-phase flow combinations

Flow Velocity Combination	V_{sl} [m/s]	V_{sg} [m/s]
1	0.53	0.50
2	0.25	0.83
3	0.53	1.66
4	0.45	1.66
5	0.40	1.66
6	0.36	1.66
7	0.52	3.31
8	0.25	3.31
9	0.44	3.31
10	0.25	4.56
11	0.29	5.38
12	0.30	6.83
14	0.43	8.28

Each simulation was run to a total of 10-seconds to allow for the flow of the two-phase mix to stabilize in the pipe and the data was exported every 0.5-seconds for analysis. Once the flow was determined to be fully through the pipe the data was examined to determine the pressure drop and liquid holdup. Figure 5.12 shows the pressure drop for one of these intervals for flow velocity combination number 7.

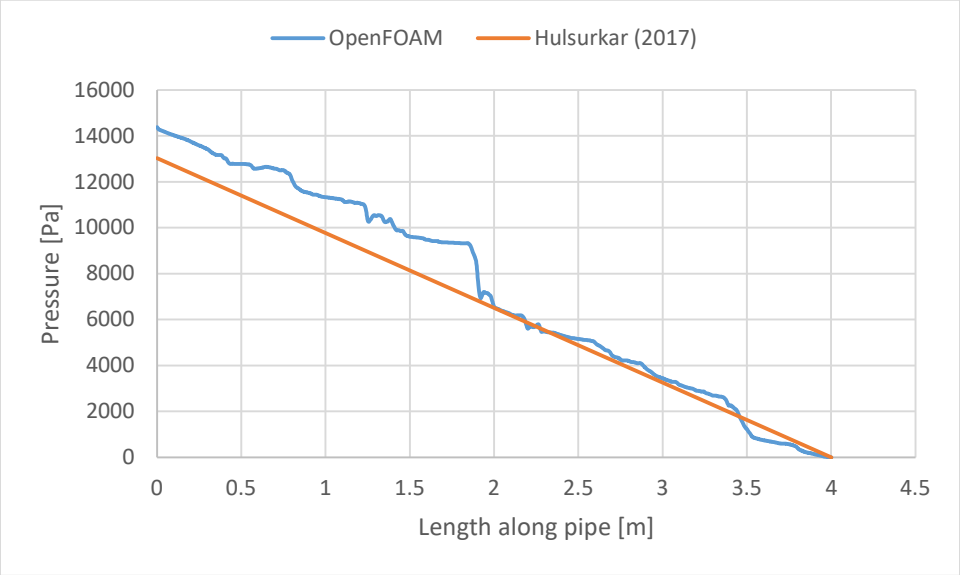

Figure 5.12 Flow velocity combination #7 single time step pressure along pipe

The pressure along the length of the pipe from the simulation is not a steady gradient for the whole length. The simulated values show a somewhat steady decrease in the pressure along approximately the first 2-meters of the pipe and then a large drop. After this drop the steady gradient continues until approximately

3.5-metetrs where another large drop is observed and the steady gradient continues. Figure 5.13 shows a cross section of the pipe and the fluid flow pattern can be observed. This flow pattern shows that at the same spot at approximately 2-meters and 3.5-meters there are peaks in the oil volume fraction forming a blockage in the pipe allowing for a larger pressure drop once the pressure profile is past those points.

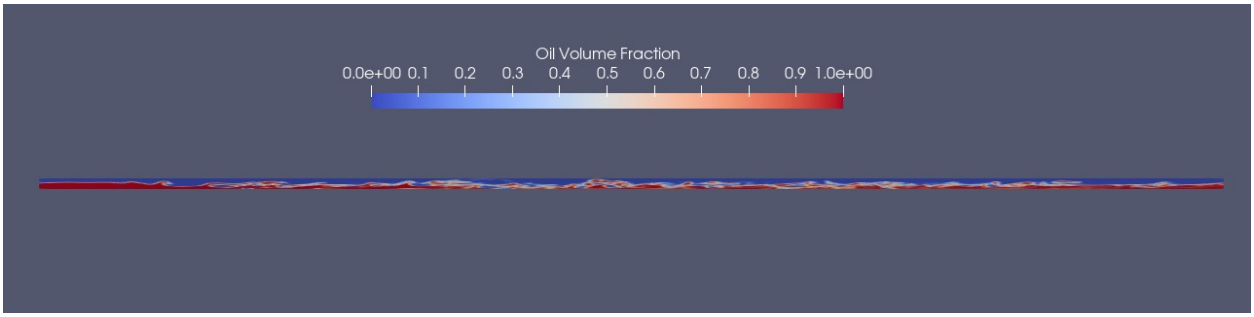

Figure 5.13 Flow velocity combination #7 cross section showing liquid holdup values

It was determined that an average of each of the pressures between 5-seconds and 10-seconds should be used to better show the normalized pressure drop along the length of the pipe. This will eliminate the large jumps when slugs of oil were going through the pipe. If the large jump was an actual feature of the flow it would show in enough of the time steps to show in the average. Figure 5.14 shows flow velocity combination number 7 as an average of all of the pressure profiles for each of the 0.5-second increments from 5-seconds to 10-seconds and the profile shows a much smoother profile than the single time increment shows.

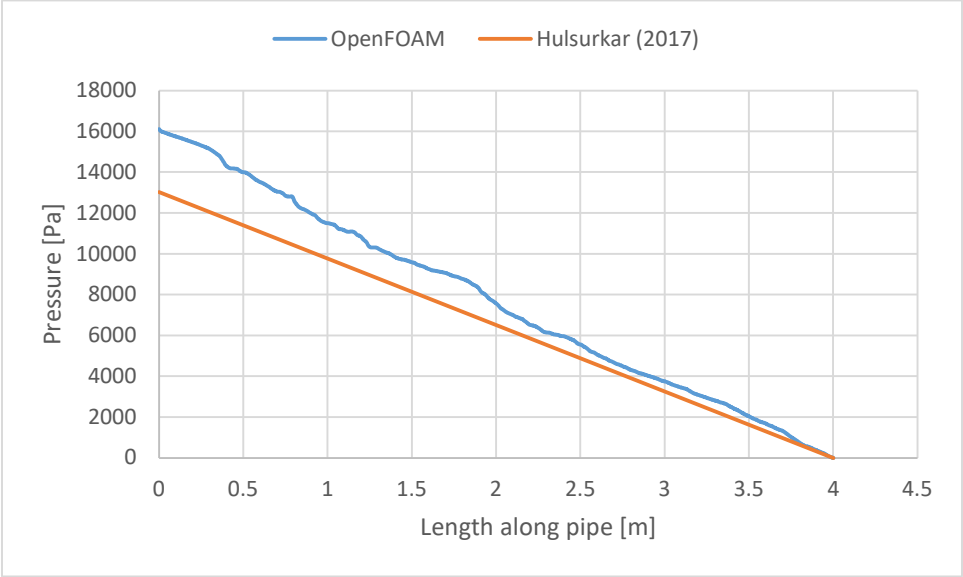

Figure 5.14 Flow velocity combination #7 average pressure along pipe over 5 seconds

The turbulent entry length was calculated in the methodology section and it was determined that the pressure drop would be picked form the 2-meter to the 3-meter section of the pipe to avoid the flow profile being affected by the fluid entry or exit. The pressure drop for flow velocity combination number 8, Figure 5.15, shows that the pressure profile is affected by the entry length for the first 1.5 to 2.0-meters. The pressure profile then levels out and follows a steadier drop from approximately 1.75-meters to 3.25-meters before it drops again. This initial high region of pressure is likely due to the turbulent entry of the

fluid and the formation of the flow pattern while the region at the end of the pipe is most likely due to the exit of the fluid from the pipe.

Not all of the flow combinations show this same pattern or in this drastic of a way but it was an important factor for calculating the correct pressure gradients for each model. For flow velocity combination 8 it changed the pressure drop from 0.095-psi/ft when examining the full length of the pipe to 0.088-psi/ft for just the region that showed steady flow. The allowed for the error between the experimental value and the simulated value to drop from 22.42% to 12.82%.

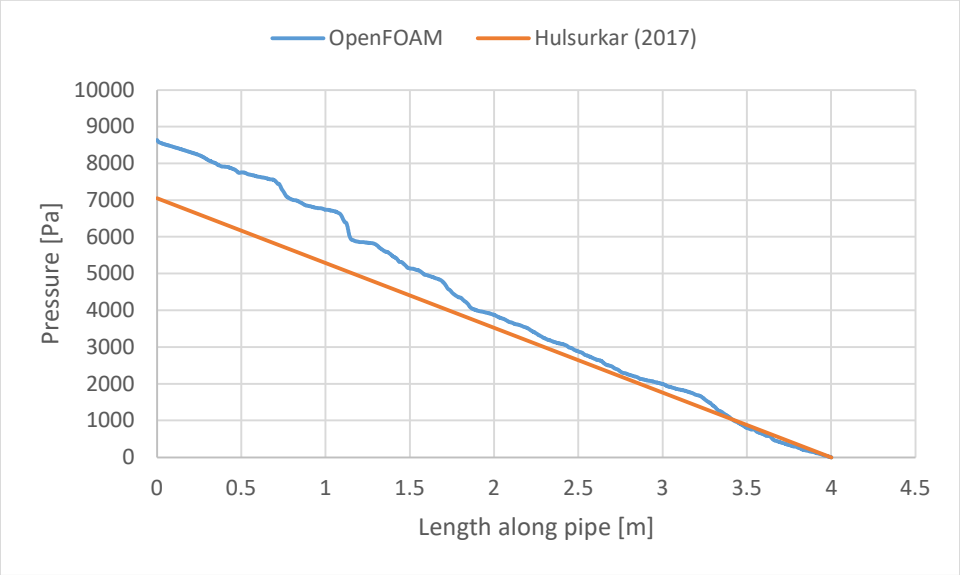

Figure 5.15 Flow velocity combination #8 pressure profile showing turbulent entry length effects

Figure 5.16 shows the results of the mix2 oil simulations compared to the experimental values. The results show there is no easily discernable pattern as to why some of the pressure gradients are close to the experimental values and some are not. For the same gas velocity, 1.66-m/s, the error between the simulated pressure gradients and the experimental pressure gradients ranges from 3.47% to 22.37%.

The liquid velocities associated with these gas velocities show that as the liquid velocity decreases the error percentage decreases as well. This shows that a lower fluid velocity for the same gas velocity is more accurate in the model. The same cannot be said for the flow velocity of 3.31-m/s where the lowest error between the experimental data and the simulated model is for the middle liquid flow velocity of the three. Figure 5.16 shows that the OpenFOAM simulation generally over predicts the experimental pressure drop and under predicts the pressure drop from the Beggs and Brill method. The OpenFOAM simulation is more in line with the results produced by the Beggs and Brill method than the experimental data.

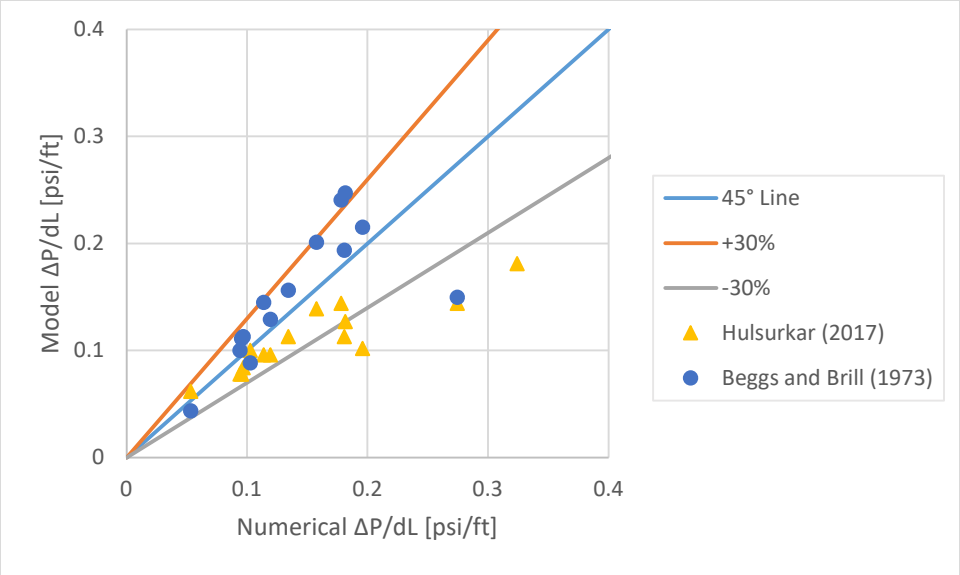

Figure 5.16 Experimental and analytical comparison for pressure drop of mix2-air two-phase flow in 1.5-inch model

The OpenFOAM software calculates the percentage of oil at each time step since it is one of the variables that are used as an initial condition and are presented in the data output. These values were averaged over the last 5-seconds of data to determine the liquid holdup value for each of the simulations. For the most part these values stayed steady or changed slowly over the time steps unless there was a slug of fluid present in the pipe during the time.

The liquid holdup values compared to the experimental liquid hold up and liquid holdup from the Beggs and Brill method, shown in Figure 5.17, shows a similar result. The four best correlating liquid holdup values are for the 1.66-m/s gas flow velocities however the best correlating holdup value is for the least accurate of the pressure gradient for this flow velocity. There is a trend that as the gas flow velocity increases the liquid holdup values becomes smaller. The OpenFOAM simulation does a reasonable job of predicting the liquid holdup for the flow combinations with a lower gas velocity. Overall the OpenFOAM simulations over predict the liquid holdup as compared to the Beggs and Brill method liquid holdup. In general, the OpenFOAM simulation does a poor job in comparison with the Beggs and Brill method for predicting liquid holdup with only one of these flow combinations falling within the ±30% range. The original work by Hulsurkar (2017) showed similar results in that the Beggs and Brill method tended to under predict the liquid holdup over the experimental results.

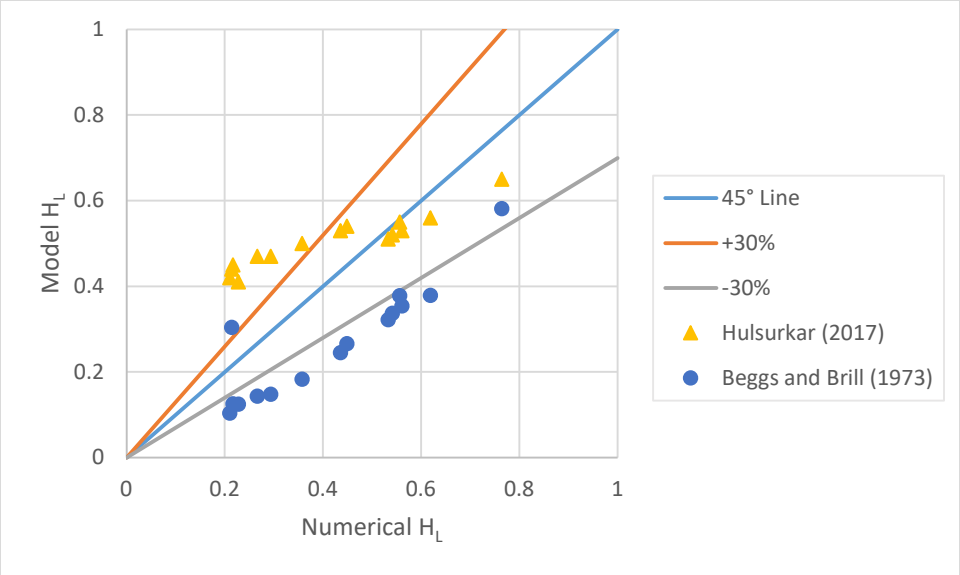

Figure 5.17 Experimental and analytical comparison for liquid holdup of mix2-air two-phase flow in 1.5-inch model

Overall the simulated pressure gradients and liquid holdup values showed a similar correlation to the Beggs and Brill calculated values. Hulsurkar (2017) showed a much as a 49% error between his experimental values and the Beggs and Brill calculated values whereas the simulated values were, on average, closer to the Beggs and Brill values than were Hulsurkar (2017). The liquid holdup values from the simulations showed a much better correlation to the Beggs and Brill calculations for the higher gas flow velocities than did the Original Hulsurkar (2017) experimental data. While these pressure drop and liquid holdup values form the simulation show a larger error it is not uncommon for two-phase flow calculations to be inaccurate compared to the analytical calculated data. It is important to remember that the Beggs and Brill calculations were derived from a 1-inch diameter pipe and air water flow and this experiment and simulation is a 1.5-inch diameter pipe and a much more viscous liquid component.

5.1.3.2 Mix3 Results

The 16 flow combinations were run through the simulation process to arrive at the results in Figure 5.18. These flow conditions show similar results to the pressure drop as did the mix2 simulations. The flow combinations that had a gas velocity of 1.6-m/s showed the best correlation with errors ranging from 3 to 9% for the four different liquid flow velocities that were simulated.

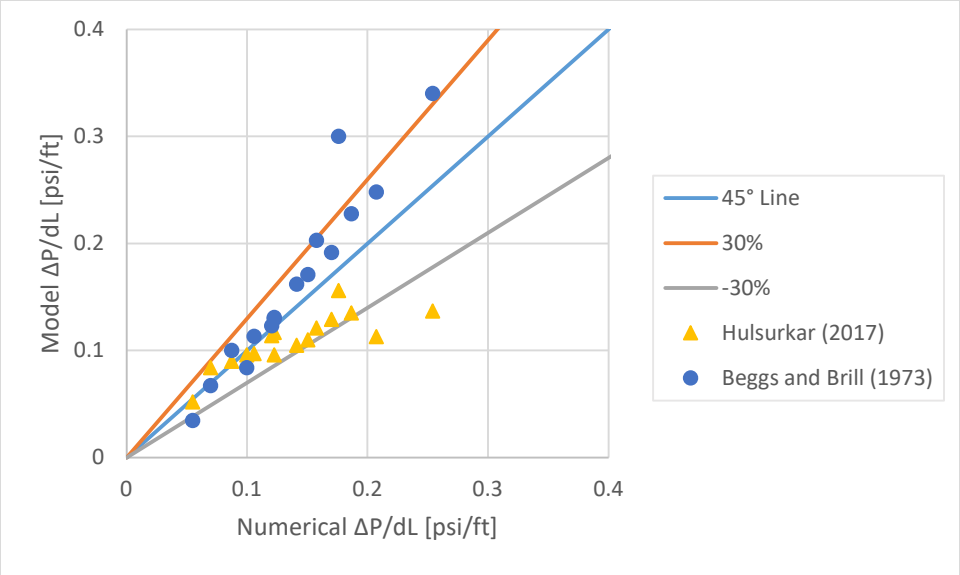

Figure 5.18 Experimental and analytical comparison for pressure drop of mix3-air two-phase flow in 1.5-inch model

Comparing the original work by Hulsurkar (2017) to the Beggs and Brill calculations these flow velocities were the ones that lined up the best. As the gas velocity increased the percent error between the experimental data and the simulations started to get larger as well similar to the mix2 oil simulations. The results for the simulations generally lie between the experimental results and the calculated Beggs and Brill. The original experimental results started to have a larger error from the Beggs and Brill calculations as the gas velocity increased. The same trend was observed for the simulated data from this study but with less growth from the calculated results.

These models were run in the exact same mesh so the results are expected to be similar for each of the two-phase flow combinations. The flow velocity combination of 0.45-m/s liquid velocity and 1.66-m/s gas velocity in the mix2 oil and 0.44-m/s liquid velocity and 1.66/m/s gas velocity in the mix3 oil shows that these two models are not as close as expected. The mix2 pressure drop from the simulation was 0.113-psi/ft and the mix3 pressure drop was 0.123-psi/ft. This 0.01-psi/ft difference is larger than the 0.001-psi/ft difference between the calculated Beggs and Brill results but not as large as the 0.019-psi/ft difference from the experimental data. This shows that the simulations are fairly accurate in predicting the pressure drop and any difference is likely due to the setup of the model or the general mesh density.

Figure 5.19 shows flow combination number 7 and is a plot of the simulated pressure drop compared to the experiment and Beggs and Brill method pressure drop along the length of the pipe. It shows that the simulated pressure drop will bounce between the experimental and Beggs and Brill method values but stays between the two values through the length of the pipe. The original experiment performed by Hulsurkar (2017) only monitored the pressure at the entrance and the exit of the pipe and did not show these variations along the length as different fractions of liquid and gas made their way thought the pipe. Since 1-psi/ft is equal to 22620.6-Pa/m it is important to note that an experimental setup would have to be fairly sensitive to catch a lot of the pressure changes along this profile if it were designed to monitor the pressure along the whole length of the pipe.

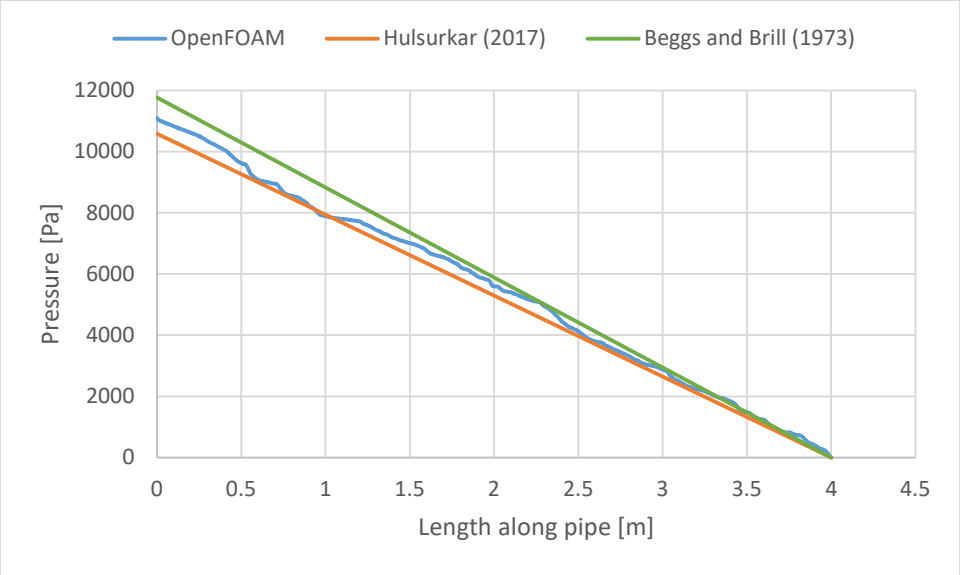

Figure 5.19 Mix3 flow combination #7 pressure profile

Figure 5.20 shows the pressure drop for flow combination 16 and the experimental and Beggs and Brill method pressure drop for comparison. This flow combination shows that the simulated pressure drop is coming in approximately half way between the experimental values and the Beggs and Brill method values. Since the original Beggs and Brill work used a 1-inch diameter pipe and water as the liquid phase it is understandable that the values for a more viscous liquid would not be the same. The pressure drop from the experimental work shows that as the gas velocity increases the pressure drop along the length of the pipe increase. This same behavior is the shown for the Beggs and Brill method pressure drop. The simulated models showed the same trend.

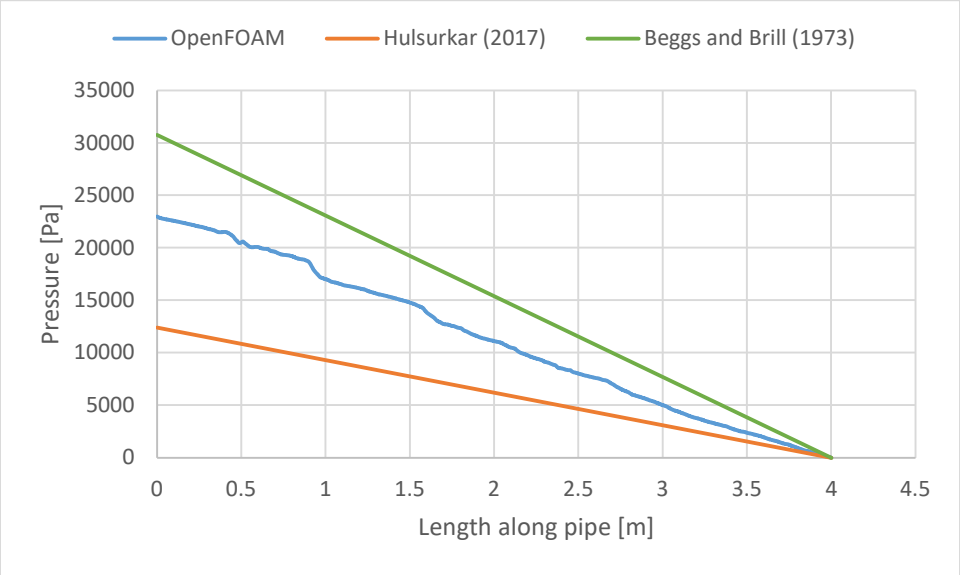

Figure 5.20 Mix3 flow combination 16 pressure profile

The calculated values for water-air flow in the 1.5-inch pipe show that for the same flow velocities the pressure drop is larger than for either of the mix oils. Table 5.7 shows five selected water-air flow conditions and their respective calculated pressure gradients. This data shows that as the gas velocities

increase so does the pressure drop in the pipe which matches well with the experimental and simulated models and the Beggs and Brill method pressure gradients from the oil calculations. What is noticeable is that for the same flow velocities of the water-air system and the oil-air system, the water–air system has a larger pressure drop at higher gas velocities and lower pressure gradients at lower gas velocities. The Beggs and Brill calculations are dependent on both the density and viscosity of the liquids and gasses in the system. The air density and viscosity is the same between the water-air system and the oil-air system so any difference between these two systems would be dependent on the oil density and viscosity as compared to the water properties.

Table 5.7 Beggs and Brill method water-air pressure drop and liquid holdup

V_{sl} [m/s]	V_{sg} [m/s]	ΔP/dL [psi/ft]	Liquid Holdup
0.27	0.41	0.0191	0.514
0.30	0.83	0.0354	0.407
0.42	1.66	0.0915	0.344
0.41	3.31	0.1627	0.237
0.39	8.28	0.3836	0.127

Changing just the density in the calculations results in a lower value for the pressure drop over the water-air system. Changing just the viscosity results in a larger value than in the water-air system. Combining the two results in a value that is similar to the one that is calculated for the air-water system. The big difference between the Beggs and Brill method pressure drop and the experimental and simulated values is that as the gas velocity increases in the system the pressure gradients do not grow as much as they do for the Beggs and Brill method calculations. One reason for this could be due to the viscosity of the fluid, the definition of viscosity includes the shear force required to cause the fluid to move. It is possible that the amount of force that is being applied by the air in the system is not enough to cause the fluid to move along the interface between the oil and the air. This would cause the air to move along the surface of the oil more in the same way that is does along the wall of the pipe as opposed to causing waves to form along the surface of the oil and causing more drag and a higher pressure drop.

The simulated liquid holdup values as compared to those from the original experiment show that the liquid holdup results are similar to the results from the mix2 flow conditions. Figure 5.21 shows the liquid holdup compared to both the experimental and the Beggs and Brill method liquid holdup. The liquid holdup value for the 1.66-m/s flow conditions lines up well with the experimental data. The higher gas flow velocities showed a larger deviation from the experimental data showing that the simulation would under predict the liquid holdup as compared to the experiment. The Beggs and Brill method values showed a much lower liquid holdup throughout the entire range of flow conditions with the higher gas velocities being the lowest liquid holdup.

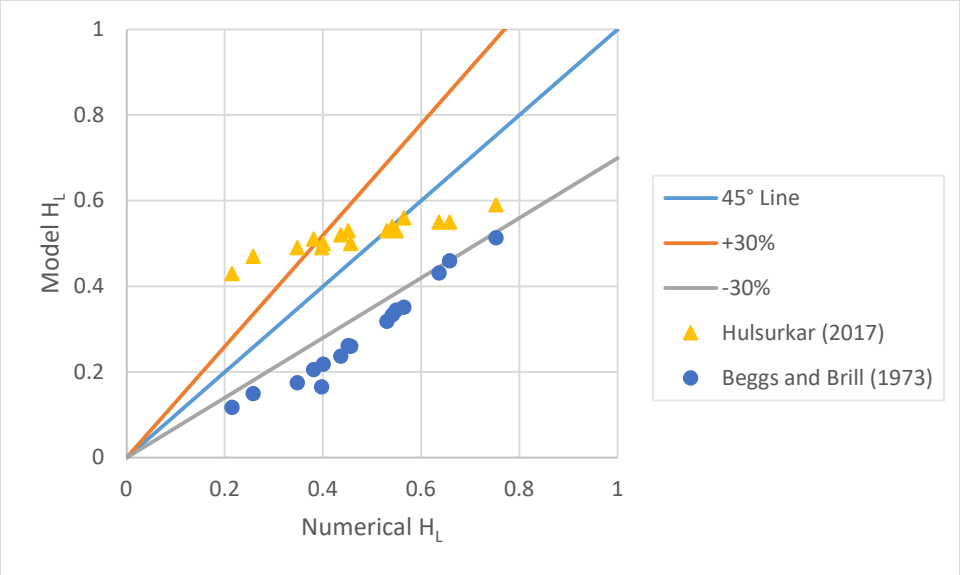

Figure 5.21 Experimental and analytical comparison for liquid holdup of mix3-air two-phase flow in 1.5-inch model

The liquid holdup values calculated in the Beggs and Brill correlation are dependent on the flow pattern within the system and the liquid velocity. The original Beggs and Brill correlation used whether the flow pattern was segregated, transitional, intermittent, or distributed to determine the constants in the equation for liquid holdup. These flow patterns were based on water being in the system instead of oil it is likely the cause of the error in the predicted liquid holdup values. The liquid holdup from the simulation fall between the experimental and calculated liquid holdup much like the pressure drop values. The experimental work stated that a synchronous closure of the valves at either end of the pipe was performed to trap the two-phase flow in the observation section of the experimental setup (Hulsurkar 2017). It is doubtful that there is much error in the liquid holdup values arrived at in the experiment. However, with larger gas velocities there should have been a smaller liquid holdup for the same liquid velocity and this is not shown in the experimental data. The experimental results have a general horizontal trend along Figure 5.21 instead of following the error bars like the Beggs and Brill method liquid holdup values with the same general trend being observed in the mix2 liquid holdup results. It is hard to say whether the experimental or the Beggs and Brill methods are closer to the actual liquid holdup values. It is most likely that the OpenFOAM simulations are over predicting the Beggs and Brill liquid holdup values and under predicting the experimental liquid holdup values.

The fault in the difference between the experimental and simulated liquid holdup values likely falls in the simulation setup and or the calculations. It was noticed that when the model was being developed that the lateral mesh size allowed for the flow pattern to differ based on the size of the mesh node. A larger node resulted in a smoother flow than a smaller node did. In order to accurately depict the flow in the simulation the mesh needs to be sized appropriately. If the flow is a dispersed bubble flow and the node size is larger than the size of the bubbles in the flow, then it will have difficulty modeling the bubbles and getting their size and movement correct. The same is true for a wavy flow in that if the surface of the flow has a feature that is smaller than the node size it will not be modeled correctly. This incorrectly modeled flow will either end up as gas or as oil depending on the calculations for the surrounding nodes. Incorrect lateral node size was also an issue in the work performed by Shuard et al. (2016). The addition of more nodes in a lateral direction of the mesh would result in a more accurate interaction between the fluid and gas in the system and would result in a different liquid holdup. Since the resources were not

available for a mesh to be run that had more nodes the liquid hold up results are a tradeoff that was made for this study.

5.2 2.875-inch Model

5.2.1 Model Construction

The 2.875-inch model was constructed with the same setup as the original 1.5-inch diameter model. The big difference in this model and the original 1.5-inch model is that the model itself does not refer to the internal diameter of the pipe but to the external diameter of the pipe. The 2.875-in diameter model was selected due to the use of this size pipe for casing in multi-lateral horizontal completion type wells that are common on the North Slope of Alaska. The 2.875-inch casing has a weight of 6.4-lbs/ft and an internal diameter of 2.441-inch, or 0.0620-meter. This internal diameter was used as the wall diameter for the model. The model was meshed using the same setting as the original 1.5-inch diameter model and resulted in a mesh with 782,439 total nodes or 1,956 nodes per slice. The y^+ values were not calculated for this size pipe and the first inflation layer size was not adjusted from the original model. Table 5.8 gives the four different flow combinations that were used for the 2.875-inch model two-phase flows. The laminar and turbulent validation were done with the liquid and gas velocities respectively.

Table 5.8 2.875-inch model flow combinations

Model	V_{sl} [m/s]	V_{sg} [m/s]
1	0.3	0.83
2	0.42	1.66
3	0.41	3.31
4	0.39	8.28

5.2.2 Validation

The validation process was the same for the 2.875-inch diameter model as it was for the original models. The laminar flow velocities were modeled with the mix3 oil properties and the turbulent flow velocities were modeled with the air properties. The Reynolds number is directly proportional to the diameter of the pipe. As the pipe gets larger the Reynolds number will increase for the same flow velocity and fluid properties giving the 3.5-inch model the highest Reynolds numbers. This decrease in Reynolds number as the pipe grows will not change the laminar flow characteristics but it will change where the transition from laminar to turbulent flow falls in the flow velocities for the air.

The laminar validation was performed and the results are shown in Figure 5.22. These results show the same exceptional correlation as the 1.5-inch model did with little error present.

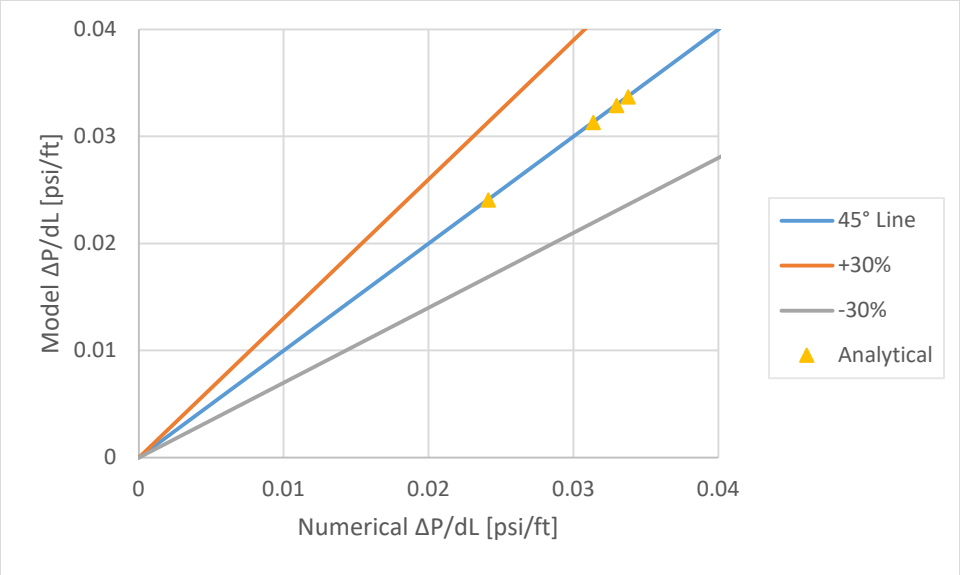

Figure 5.22 Analytical comparison of pressure drop for laminar mix3 fluid in 2.875-inch model

The velocity profile for the laminar flow are all close to the analytical values and the centerline velocities are shown in Figure 5.23. These values all fall 0.21% from the analytical values which is a slight increase over the error in centerline velocity in the 1.5-inch diameter model and is likely the reason the pressure drop calculations are show more error. Figure 5.24 shows the velocity profile for the 0.3-m/s as compared to the analytical profile and it shows that the two profiles match up consistently.

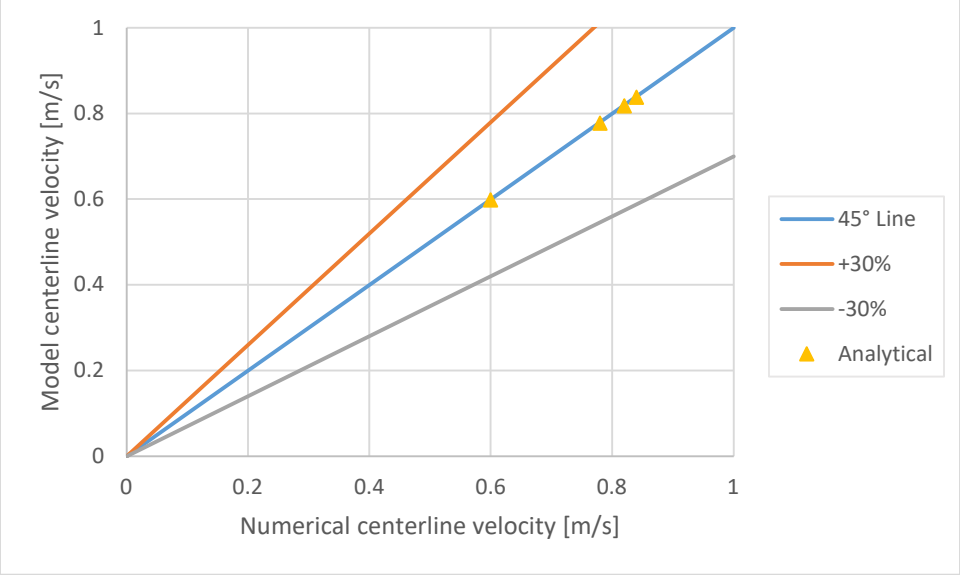

Figure 5.23 Analytical comparison of centerline velocity for laminar mix3 fluid in 2.875-inch model

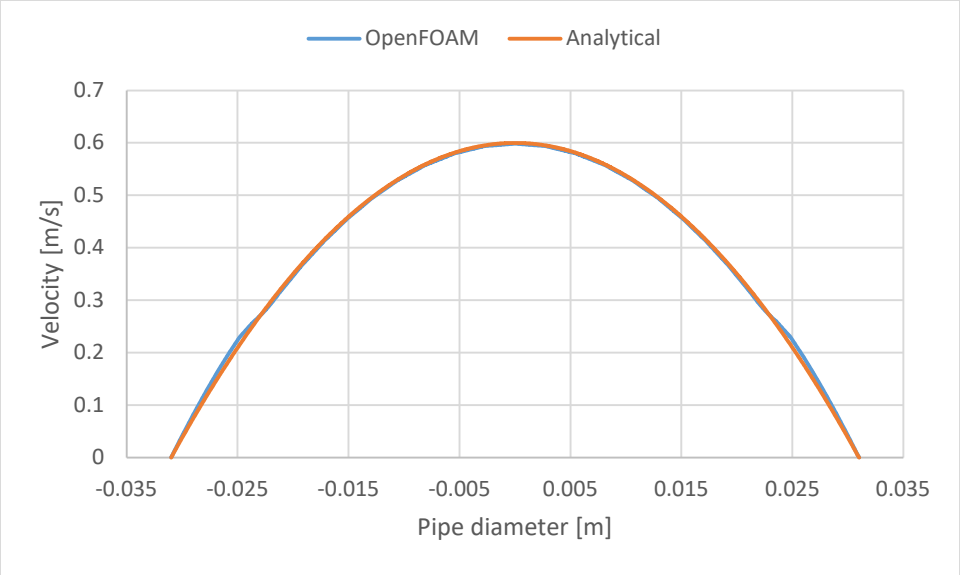

Figure 5.24 2.875-inch model laminar validation flow velocity #1 velocity profile

The turbulent validation was performed for the four given flow velocities and is shown in Figure 5.25. The pressure gradients fall in line with what was observed in the 1.5-inch diameter model. The lowest flow velocity, 0.83-m/s, being in the transition zone between laminar and turbulent flow shows the largest percent of error amongst the group. As the flow velocity increases the percent error in the pressure drop starts to increase similar to the original validation data of the 1.5-inch diameter pipe. This model shows a larger increase in the error for the pressure drop for the same flow velocities at the higher end and is likely due to the larger Reynolds number showing a more turbulent flow.

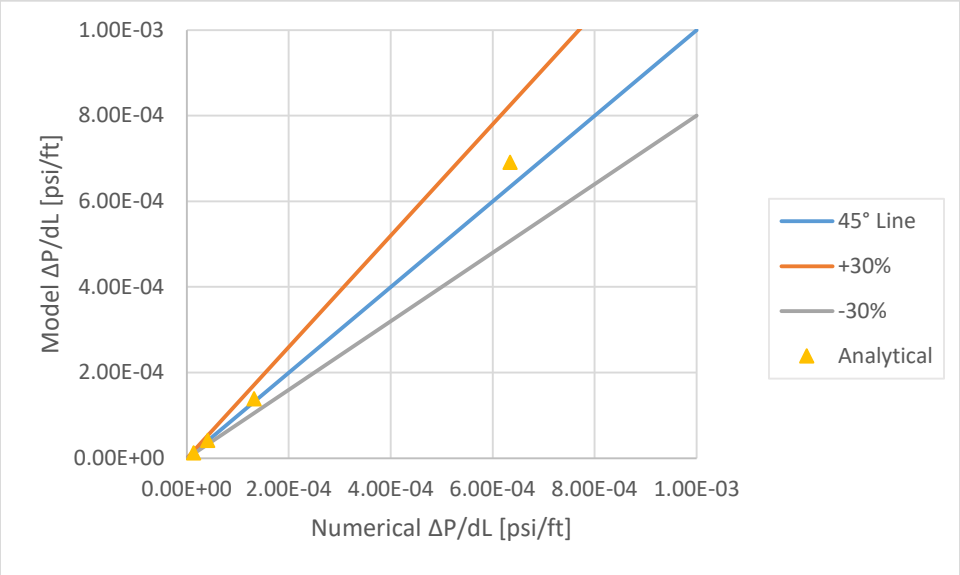

Figure 5.25 Analytical comparison of pressure drop for turbulent air in 2.875-inch model

The velocity profiles show a much better match for the centerline velocity over the 1.5-inch model and the comparison is shown in Figure 5.26. The lowest flow velocity is showing an error of 3.71% in the centerline velocity and is the worst of the four scenarios. Figure 5.27 shows the velocity profile and the analytical velocity profile for flow velocity #1 and shows that overall the simulated centerline velocity is

higher than the analytical centerline velocity and is likely what is leading to the overestimation in the pressure drop for this model.

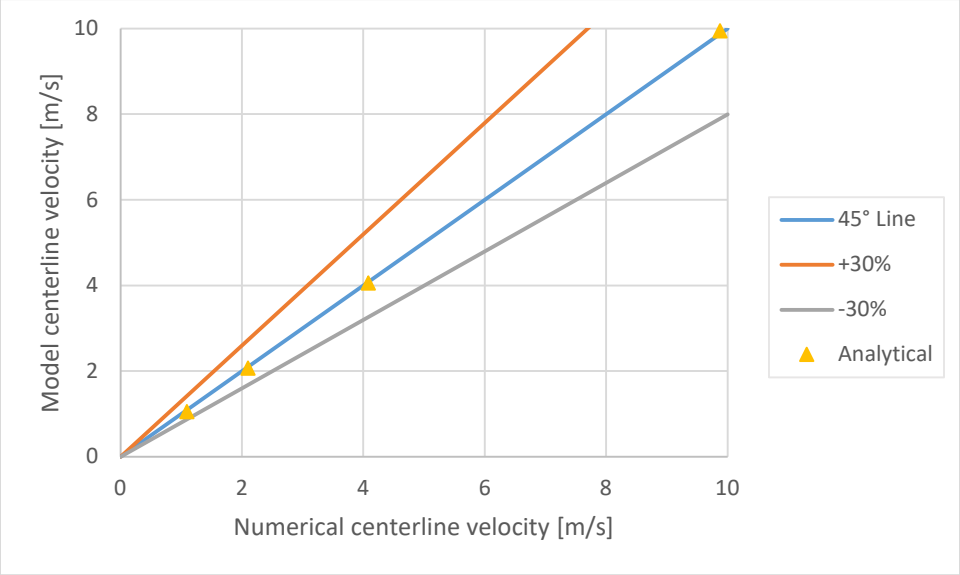

Figure 5.26 Analytical comparison of centerline velocity for turbulent air in 2.875-inch model

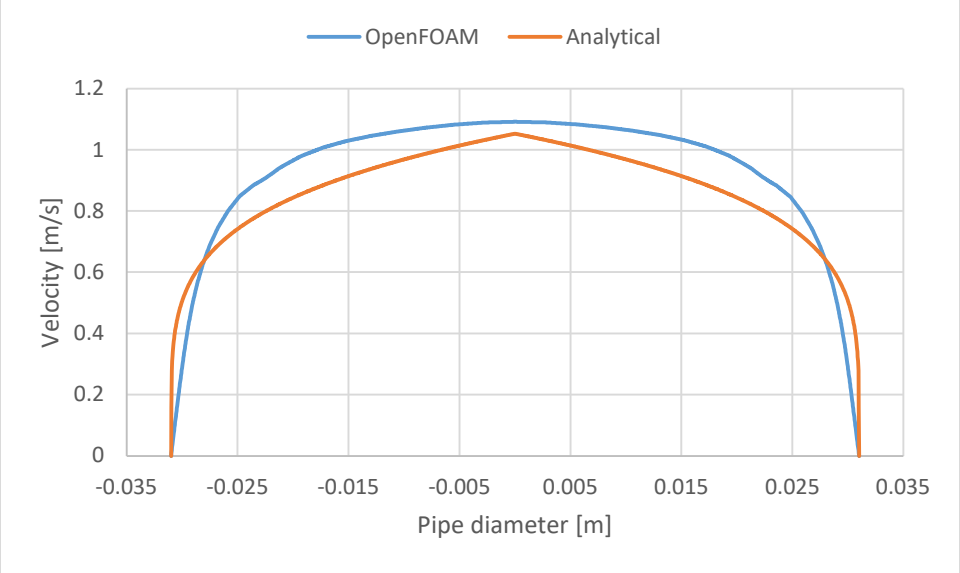

Figure 5.27 2.875-inch model turbulent validation flow velocity #1 velocity profile

5.2.3 Mix2

There was no experimental data from Hulsurkar (2017) for any pipe sizes besides the 1.5-inch diameter pipe so these models were run based on the Beggs and brill correlation for comparison. The four models that were run fall within the ±30% error lines when compared to the Beggs and Brill model as shown in Figure 5.28 with the numerical values given in Table 5.9.

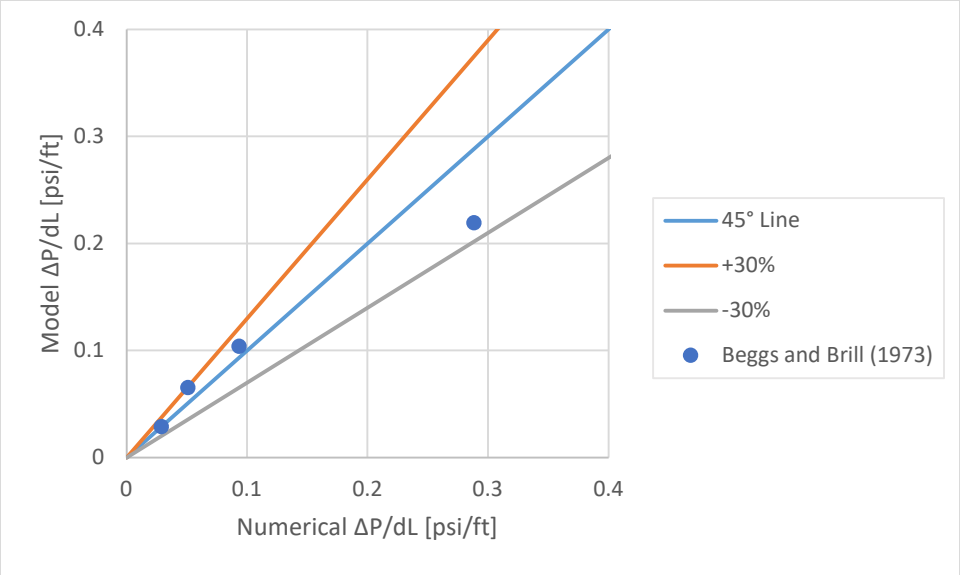

Figure 5.28 Analytical comparison for pressure drop for mix2-air two-phase flow in 2.875-inch model

Table 5.9 2.875-inch model mix2 pressure drop

Flow Velocity Combination	V_{sl} [m/s]	V_{sg} [m/s]	Beggs & Brill (1973) ΔP/dL [psi/ft]	Analytical ΔP/dL [psi/ft]
1	0.30	0.83	0.029	0.029
2	0.42	1.66	0.065	0.051
3	0.41	3.31	0.104	0.093
4	0.39	8.28	0.219	0.288

The simulation shows that flow velocity combination number 1, 0.30-m/s liquid velocity and 0.83-m/s gas velocity, has a 0.88% error between the simulation and the Beggs and Brill model pressure drop. The 1.66-m/s gas flow velocity did not show as good a correlation as with the 1.5-inch diameter pipe as it was 22% lower than the Beggs and Brill model pressure drop in this case. The worst of the flow velocity combinations was number 4 with a 31.42% error over the Beggs and Brill model pressure drop. Overall all four of these simulations do a decent job of predicting the pressure drop along the pipe and all fall within the ±30% range of Figure 5.28.

Since there was no experimental data the liquid holdup at the inlet was assigned the same value as the Beggs and Brill correlation. The simulation was allowed to calculate the liquid holdup based on the flow in the model. The liquid holdup was over estimated for each of the four flow velocity combinations as shown in Figure 5.29 with numerical values given in Table 5.10. These liquid holdups are more in line with the experimental data shown by Hulsurkar (2017) where all of the liquid holdup values were also higher than the Beggs and Brill model liquid holdup values.

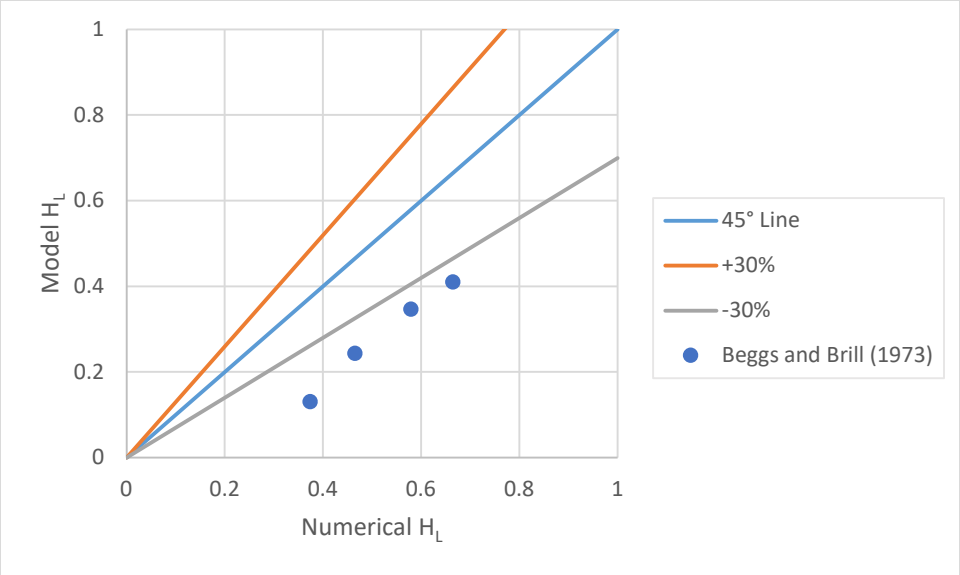

Figure 5.29 Analytical comparison for liquid holdup of mix2-air two-phase flow in 2.875-inch model

Table 5.10 2.875-inch model mix2 liquid holdup

Flow Velocity Combination	V_{sl} [m/s]	V_{sg} [m/s]	Beggs & Brill (1973) Liquid Holdup	Analytical Liquid Holdup
1	0.30	0.83	0.41	0.665
2	0.42	1.66	0.35	0.579
3	0.41	3.31	0.24	0.465
4	0.39	8.28	0.13	0.374

5.2.4 Mix3

The four mix3 flow conditions showed the same correlation with Beggs and Brill model pressure gradients as the mix2 flow conditions. The only difference in this case is that the majority of the pressure gradients showed a larger error as compared to the same mix2 values. The only flow condition that did not show a larger error percentage was flow condition number 2, 0.42-m/s liquid velocity and 1.66-m/s gas velocity, and it showed a marginally less percentage of error over the same mix2 flow condition. Figure 5.30 gives the analytical pressure gradients compared to the Beggs and Brill method pressure gradients for each of the four flow conditions with numerical values given in Table 5.11.

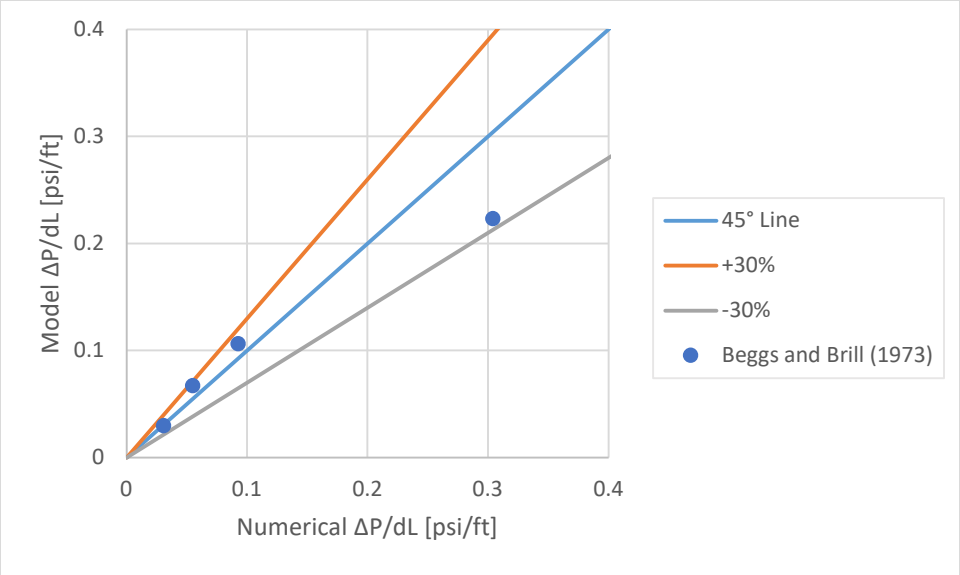

Figure 5.30 Analytical comparison for pressure drop for mix3-air two-phase flow in 2.875-inch model

Table 5.11 2.875-inch model mix3 pressure drop

Flow Velocity Combination	V_{sl} [m/s]	V_{sg} [m/s]	Beggs & Brill (1973) ΔP/dL [psi/ft]	Analytical ΔP/dL [psi/ft]
1	0.30	0.83	0.030	0.031
2	0.42	1.66	0.067	0.055
3	0.41	3.31	0.107	0.093
4	0.39	8.28	0.223	0.304

The liquid holdup values showed the same general trend as the mix2 liquid holdup values. Higher gas velocity generated a larger percentage of error for the liquid holdup as compared to the Beggs and Brill method liquid holdup. The errors in the liquid holdup were roughly the same as the error percentage for the mix2 flow conditions with the largest error being flow condition number 4. Figure 5.31 shows the simulated liquid hold up as compared to the Beggs and Brill method liquid holdup with numerical values given in Table 5.12.

Table 5.12 2.875-inch model mix3 liquid holdup

Flow Velocity Combination	V_{sl} [m/s]	V_{sg} [m/s]	Beggs & Brill (1973) Liquid Holdup	Analytical Liquid Holdup
1	0.30	0.83	0.41	0.668
2	0.42	1.66	0.35	0.585
3	0.41	3.31	0.24	0.483
4	0.39	8.28	0.13	0.373

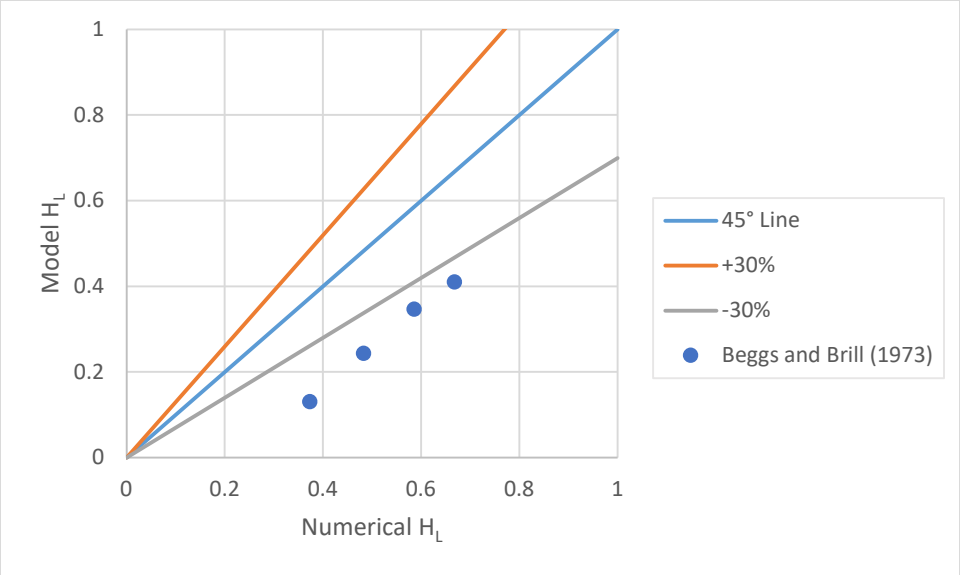

Figure 5.31 Analytical comparison for liquid holdup of mix3-air two-phase flow in 2.875-inch model

5.3 3.5-inch Model

5.3.1 Model Construction

The 3.5-inch model was setup up in the same manner at the 2.875-inch model. This model is based on a 3.5-inch 9.3-lb/ft diameter pipe that is common in wells on the North Slope of Alaska as well as many other places in the world. This pipe is used as both a tubing and/or a liner in wells and has an internal diameter of 2.992-inches or 0.076-meters. Much like the 2.875-inch diameter model this 2.992-inch diameter was used as the wall diameter of the model. The mesh was generated using the same properties for maximum node size, first inflation layer thickness, and lateral node size. This mesh resulted in 977,151 total nodes with 2,442 nodes per slice. Table 5.13 gives the four different flow combinations that were used for the 3.5-inch model two-phase flows. The laminar and turbulent validation were done with the liquid and gas velocities respectively.

Table 5.13 3.5-inch model flow combinations

Model	V_{sl} [m/s]	V_{sg} [m/s]
1	0.3	0.83
2	0.42	1.66
3	0.41	3.31
4	0.39	8.28

5.3.2 Validation

The laminar pressure drop validation data, shown in Figure 5.32, shows the same exceptional correlation with the analytical pressure drop and the previous two models.

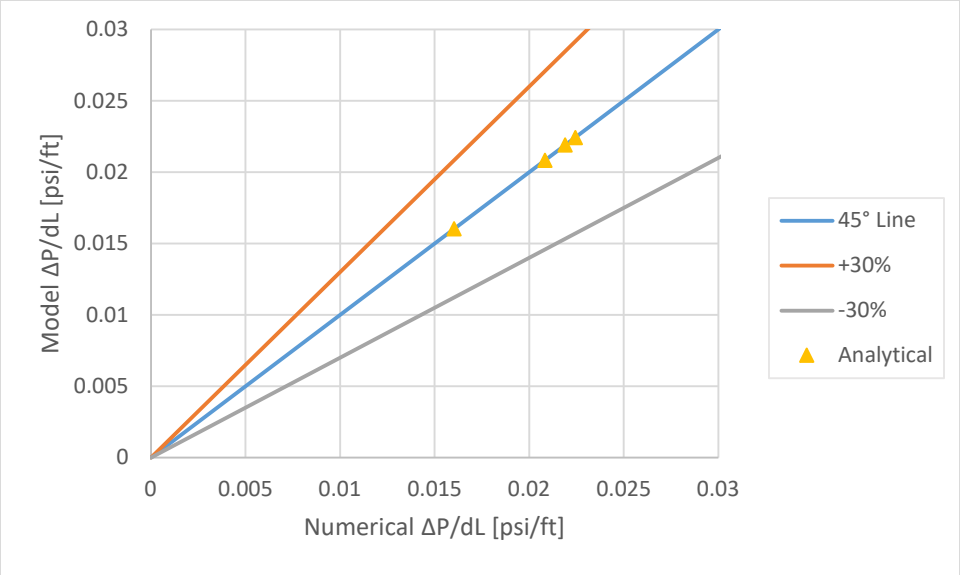

Figure 5.32 Analytical comparison of pressure drop for laminar mix3 fluid in 3.5-inch model

The centerline velocities, shown in Figure 5.33, also have a similar correlation to the analytical centerline velocities as with the previous laminar validation runs. These values show a slightly better correlation to the analytical values than does the 2.87-inch model but not as good as the original 1.5-inch model.

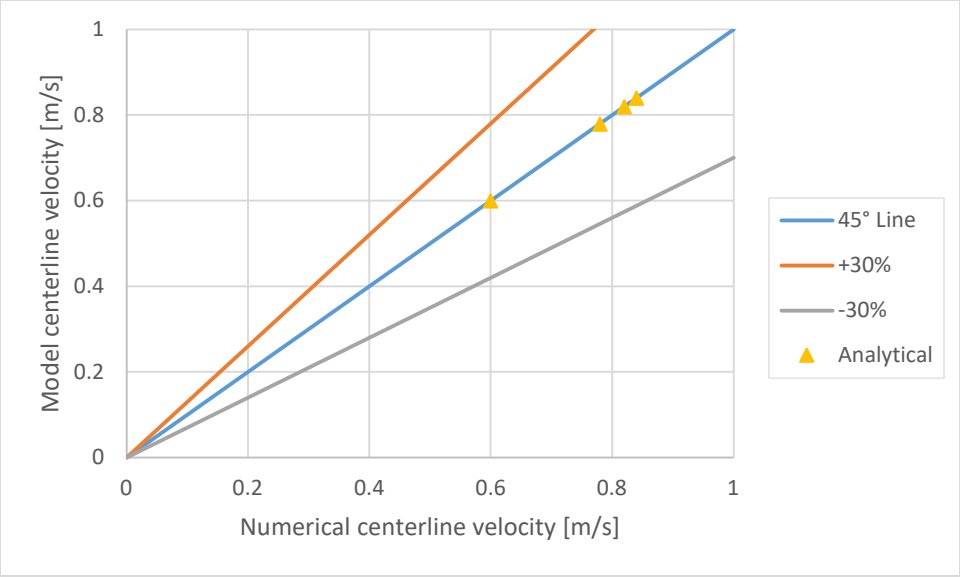

Figure 5.33 Analytical comparison of centerline velocity for laminar mix3 fluid in 3.5-inch model

Figure 5.34 shows the turbulent pressure gradients and the same general trend in correlation as the previous two models. The lowest flow velocity, 0.83-m/s, showed a higher value than any of the other three flow velocities but with it being in the transition zone between turbulent and laminar flow this was expected. This pressure drop shows less of an error than the same flow velocity in either the 2.875-inch or 1.5-inch models.

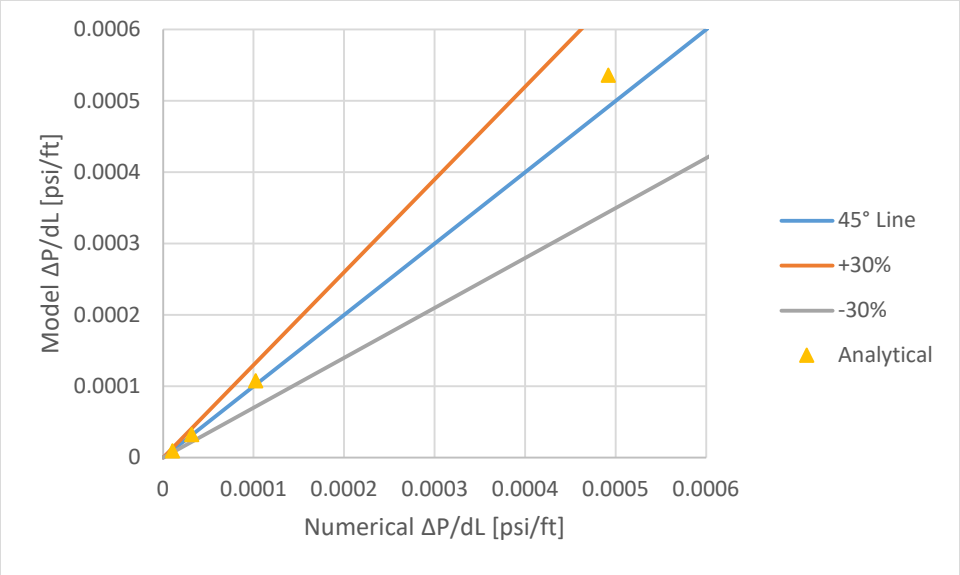

Figure 5.34 Analytical comparison of pressure drop for turbulent air in 3.5-inch model

The centerline velocity for the turbulent models, Figure 5.35, shows a better correlation than the 2.875-inch model. These values are within an acceptable range throughout the four flow velocities modeled with the highest error being 2.56% for the 0.83-m/s flow velocity. The centerline velocities show the same trend as the 2.875-inch model, in that the velocity shows less error for the middle two flow velocities than for the first or last flow velocity. This shows that as the flow becomes more turbulent the simulation has difficulty properly calculating the flow.

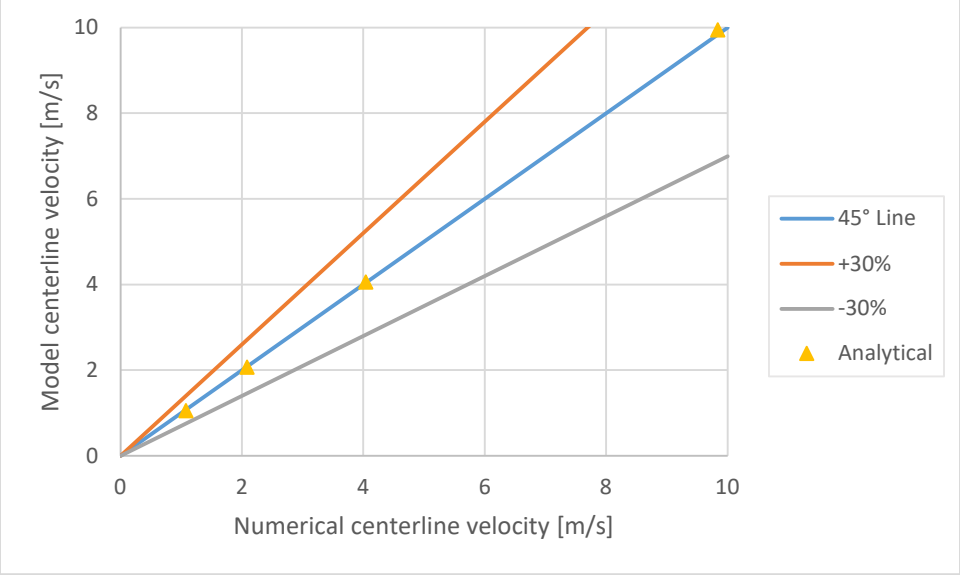

Figure 5.35 Analytical comparison of centerline velocity for turbulent air in 3.5-inch model

5.3.3 Mix2

The mix2 pressure gradients for the 3.5-inch diameter pipe show an odd result as compared to any of the other models in the study. Figure 5.36 gives the pressure gradients from the simulation as compared to the Beggs and Brill model pressure gradients with numerical values given in Table 5.14.

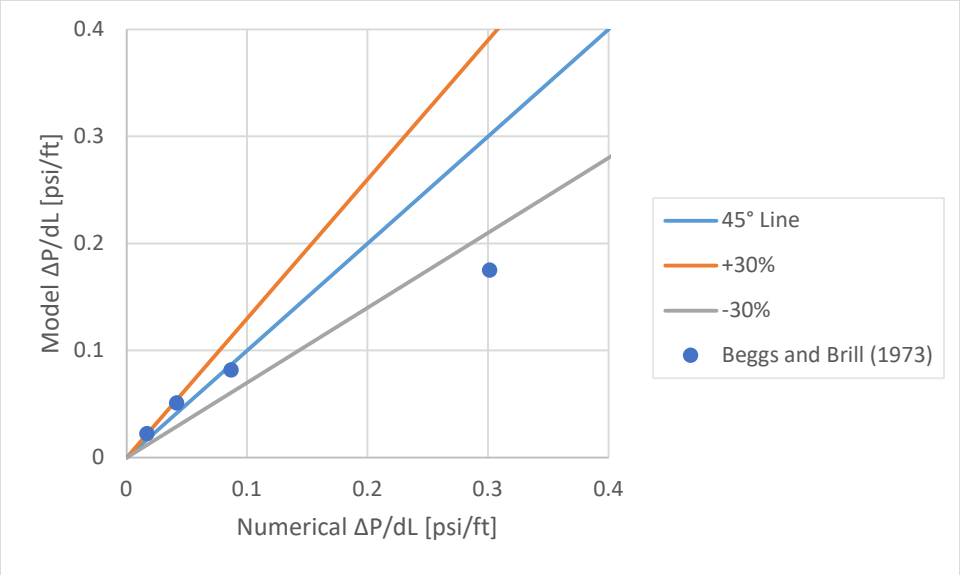

Figure 5.36 Analytical comparison pressure drop of mix2-air two-phase flow in 3.5-inch model

Table 5.14 3.5-inch model mix2 pressure drop

Flow Velocity Combination	V_{sl} [m/s]	V_{sg} [m/s]	Beggs & Brill (1973) ΔP/dL [psi/ft]	Analytical ΔP/dL [psi/ft]
1	0.30	0.83	0.023	0.017
2	0.42	1.66	0.051	0.041
3	0.41	3.31	0.082	0.087
4	0.39	8.28	0.175	0.301

The simulation shows that the best correlation for pressure drop is for flow condition number 3, 0.41-m/s liquid velocity and 3.31-m/s gas velocity. This simulation resulted in a 5.99% error as opposed to the 18+% error that was present in all of the other flow conditions. In general, the two models that were generated beyond the original experimental data showed that as the gas velocity increased in the system the error in the pressure drop also increased. In this case the lowest value is for the third highest gas flow velocity. These models did not show any abnormality when being run and were ran more than once to verify the results with each of these runs showing the same pressure drop along the length of the pipe.

The liquid holdup values showed the same correlation as the 2.875-inch model in that as the gas velocity increased so did the error in the liquid holdup from the Beggs and Brill method value. Figure 5.37 shows these liquid holdup values and shows that they are further outside the -30% line than for the same flow condition in the 2.875-inch model with numerical values given in Table 5.15.

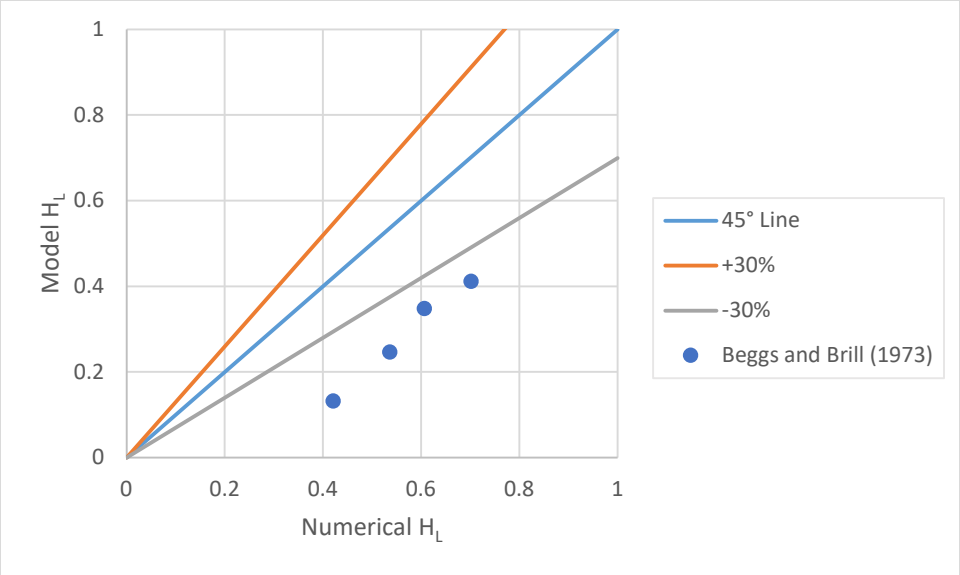

Figure 5.37 Analytical comparison for liquid holdup of mix2-air two-phase flow in 3.5-inch model

Table 5.15 3.5-inch model mix2 liquid holdup

Flow Velocity Combination	V_{sl} [m/s]	V_{sg} [m/s]	Beggs & Brill (1973) Liquid Holdup	Analytical Liquid Holdup
1	0.30	0.83	0.41	0.702
2	0.42	1.66	0.35	0.606
3	0.41	3.31	0.25	0.536
4	0.39	8.28	0.13	0.421

5.3.4 Mix3

The pressure gradients from the mix3 runs in the simulation of the 3.5-inch pipe are shown in Figure 5.38 with numerical values given in Table 5.16. These results match well with the results from mix2 for the 3.5-inch pipe and the results for both oil mixes for the 2.875-inch pipe. The lowest flow velocity combination shows the lowest percent error from the Beggs and Brill method pressure drop and the errors increase as the gas velocity in the system increases. Overall the error in the pressure gradients for the 3.5-inch model are larger than they were for the 2.875-inch model. The fourth flow velocity combination, 0.39-m/s liquid velocity and 8.28-m/s gas velocity, show a rather large 122.25% error from the Beggs and Brill method pressure drop and this is by far the largest error observed in this study.

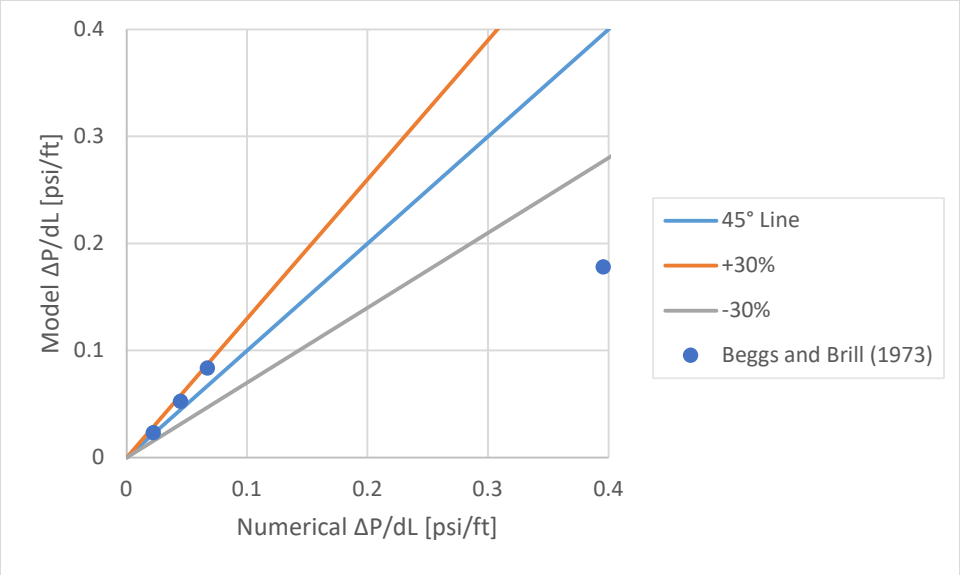

Figure 5.38 Analytical comparison for pressure drop of mix3-air two-phase flow in 3.5-inch model

Table 5.16 3.5-inch model mix3 pressure drop

Flow Velocity Combination	V_{sl} [m/s]	V_{sg} [m/s]	Beggs & Brill (1973) ΔP/dL [psi/ft]	Analytical ΔP/dL [psi/ft]
1	0.30	0.83	0.023	0.022
2	0.42	1.66	0.053	0.045
3	0.41	3.31	0.084	0.067
4	0.39	8.28	0.178	0.396

Figure 5.39 shows the pressure drop compared to the Beggs and Brill method pressure drop for flow combination number 4. There is a large entry length forming that is almost 2-meters from the entrance of the pipe. The pressure drop was taken from the 2-meter to 3-meter section similar to all of the rest of the models but the simulation is still transitioning from the entry length flow to the actual flow in the pipe from 2-meters to 2.5-meters and is causing error in the simulated pressure drop. Obtaining the pressure drop from 2.5-meters to 3.5-meters gives a more accurate 0.284-psi/ft which is a 59.55% error over the Beggs and Brill method value.

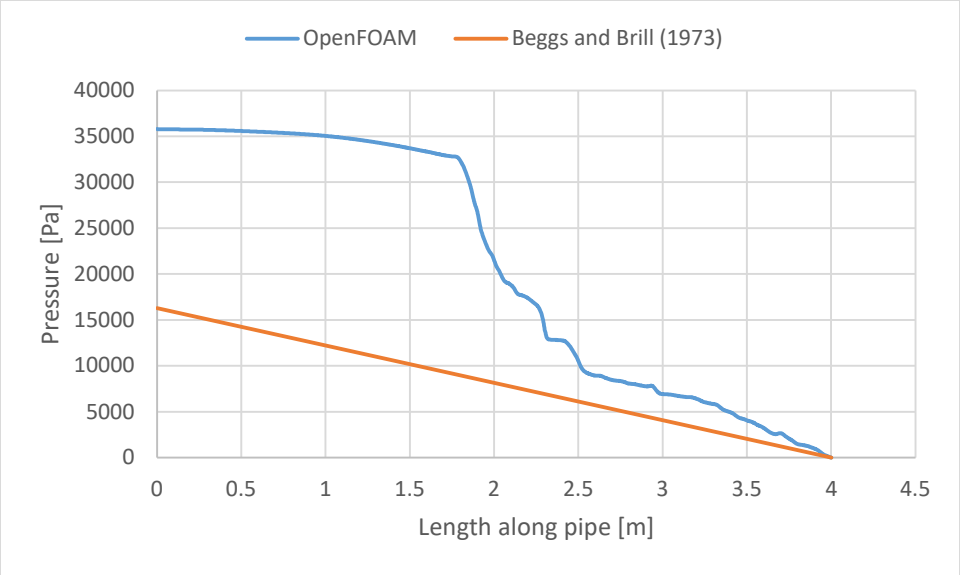

Figure 5.39 3.5-inch flow combination #4 pressure drop

The liquid holdup values show the same trend as in the 2.875-inch model in that as the gas flow velocity increases the error between the simulated liquid holdup and the Beggs and Brill method liquid holdup increases. Figure 5.40 shows the liquid holdup values as compared to the Beggs and Brill method for each of the four models with numerical values given in Table 5.17.

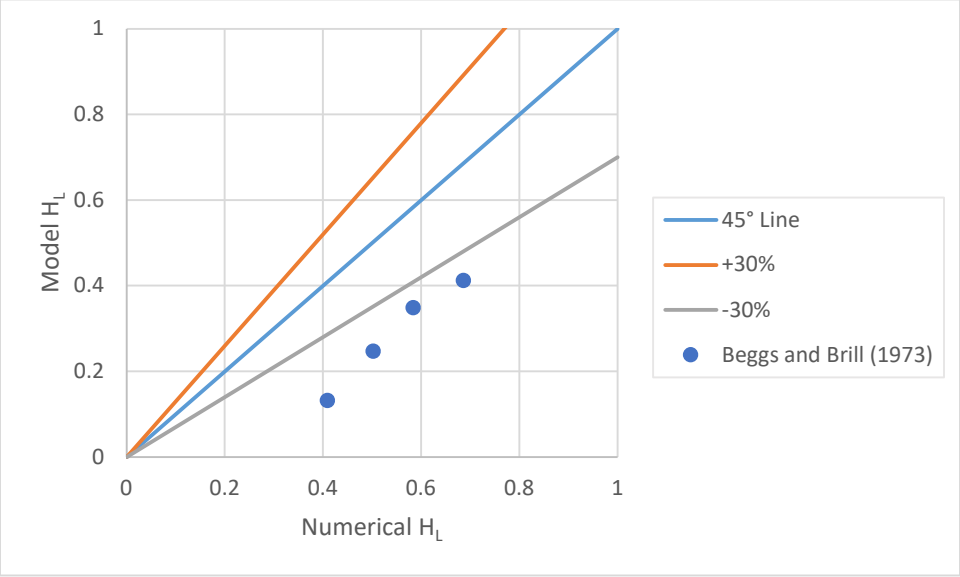

Figure 5.40 Analytical comparison for liquid holdup of mix3-air two-phase flow in 3.5-inch model

Table 5.17 3.5-inch model mix3 liquid holdup

Flow Velocity Combination	V_{sl} [m/s]	V_{sg} [m/s]	Beggs & Brill (1973) Liquid Holdup	Analytical Liquid Holdup
1	0.30	0.83	0.41	0.686
2	0.42	1.66	0.35	0.584
3	0.41	3.31	0.25	0.502
4	0.39	8.28	0.13	0.409

Flow condition 4 shows the largest error in the liquid holdup much like it showed the largest error in the pressure drop. Figure 5.41 shows the entry region of the pipe and there is an easily discernable split between the gas on the top of the pipe and the oil on the bottom of the pipe. At approximately 2-meters along the pipe, half way along the image, the split of the oil and gas layers starts to break up and at around 2.5-meters the flow starts to develop into a much more turbulent flow pattern.

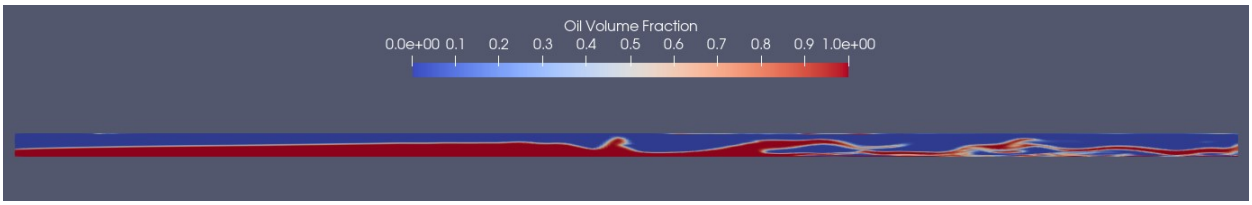

Figure 5.41 3.5-inch model flow combination #4 cross section showing liquid holdup values

What is not known from this data is if the turbulent flow near the exit of the pipe is showing disturbance from the exit of the pipe or if it is showing the desired flow along the pipe. It was shown in the 1.5-inch pipe that a small region forms near the exit of the pipe that is different than the steady flow in the pipe. With how large the entry length shows up in this situation as compared to any of the entry lengths observed in the 1.5–inch pipe, it is possible that the flow in this model is only showing an entry length and an exit length and no actual pipe flow. A longer model would be needed to verify that the flow in the 2.5-meter to 3.5-meter section of the pipe is the actual pipe flow.

6 CHAPTER SIX: CONCLUSIONS AND RECOMMENDATIONS

6.1 Conclusions

This study modeled two-phase heavy oil and gas flow through three different sized pipes. Starting with experimental data collected by Hulsurkar (2017), a model was built to mimic the setup from the original experiment. This model consisted of a 1.5-inch diameter pipe that was 4-meters long and was meshed in a way to allow for the turbulence to be successfully modeled along the wall of the pipe. This mesh was run through a validation process in which the heavy oil was run through the simulation process for a laminar validation and air was run through the simulation process for a turbulent validation. After the validation the two-phase oil-air flow was simulated and compared to the original experimental results and Beggs and Brill method values for pressure drop and liquid holdup. A 2.875-inch and 3.5-inch model was then constructed and the validation process was completed again for each model with two-phase simulations run and the results compared to analytical values for pressure drop and liquid holdup.

The validation simulations showed that the laminar flow for all three model sizes showed an exceptional correlation to the analytical values for both the pressure drop and velocity profiles. The error between the analytical values and the simulated values never exceeding 0.50%. The turbulent flow validation showed that for flow velocities in the transition region between the laminar and fully turbulent flows showed a poorer correlation for pressure drop and velocity profile than did flow velocities that were fully in the turbulent flow regime. Due to the properties of the air being modeled these errors resulted in small errors in the pressure drop over a long length of pipe so they were ignored for this study. The pressure drop calculations and velocity profiles for the flows that are in the fully turbulent zones showed a good correlation across all three model sizes.

The two-phase flow results for the original 1.5-inch model showed varying correlation to the original experimental data. Some flow velocity combinations showed small errors and some showed larger errors. The models showed in general that as the gas velocity increases in the system the error in the pressure drop start to grow. The pressure drop calculated by the simulations was halfway between the experimental data and the Beggs and Brill method values. The liquid holdup from the two-phase flows showed a similar correlation as the pressure drop results in that as the fluid velocity increased the error between the simulated and experimental liquid holdup started to grow. The models were under predicting the liquid holdup in the system from the experimental results but were over predicting the liquid holdup from the Beggs and Brill method values.

The 2.875-inch and 3.5-inch models were run with a small subset of two-phase flow conditions and showed similar results for pressure drop and liquid holdup as the 1.5-inch model. Since there was no experimental data to compare the results from these two models, only the Beggs and Brill method values were used for comparison. These models showed that as the gas velocity increases the pressure drop error start to increase similar to the original 1.5-inch model. The same results were observed for the liquid holdup values between the Beggs and Brill method and simulated values. The higher the gas velocity the more error in the liquid holdup values. It was observed that the as the gas velocity increased in the 3.5-inch model the turbulent entry length started to increase in the pipe taking up almost half of the total length. The results from these higher velocity systems are suspect as it is possible that all that is being model in the turbulent entry and exit from the pipe and no stabilized two-phase flow was observed in the system.

Overall this study showed that a computer model of two-phase heavy oil-gas flow is possible to build. These models showed good correlation with the experimental pressure drop and liquid holdup for the same conditions. The original model was able to be upsized to show pressure drop and liquid holdup from two different larger size pipes with little additional effort. While the pressure drop and liquid

holdup values measured in the simulation does not exactly match the experimental data it is a starting point for future studies.

6.2 Recommendations for Future Work

- Generate a higher density mesh to be used to run the simulations on more computer nodes for longer time
- While some longer models were made during the process of generating the 1.5-inch mesh model they were not employed in this study. Future study could benefit from generating different model lengths to determine if it affects the flow in larger pipe sizes
- The simulated models showed small fluctuations in the pressure in the system during the flow and designing an experimental setup to attempt to capture these fluctuations could prove beneficial to the industry
- Setting up an experiment for larger pipe sizes to obtain data for calibration of future computational simulations

REFERENCES

Anderson, John D. 1995. *Computational Fluid Dynamics The Basics with Applications*.

ANSYS. 2006. *Modeling Turbulent Flows*: Introductory FLUENT Training (Reprint).

ANSYS, Inc. 2013. *ANSYS Fluent Theory Guide*. Canonsburg, Pa: ANSYS, Inc.

Bata, Timothy, Schamel, Steven, Fustic, Milovan et al. 2019. Bitumen and heavy oil committee annual commodity. *AAPG Energy Mineral Division* **Report - May 2019**.

Beal, Carlton. 1945. The viscosity of air, water, natural gas, crude oils and its associated gases at oil field temperatures and pressures.

BP-Alaska. 2011. *Heavy Oil vs. Light Oil* (Reprint). https://www.aoga.org/wp-content/uploads/2011/03/HRES-3.10.11-Lunch-Learn-BP-Heavy-Oil1.pdf.

Byrne, M.T, Jimenez, M.A., Rojas, E.A. et al. 2010. Modelling well inflow potential in three dimensions using computational fluid dynamics. Presented at the SPE International symposium and exhibition on formation damage, Lafayette, Louisiana, USA. 10-12 February 2010. **SPE-128082-MS.** https://doi.org/10.2118/128082-MS.

Byrne, Michaael, Jimenez, Maria Alejandra, and Chavez, Juan Carlos. 2009. Predicting well inflow using computational fluid dynamics - closer to the truth? Presented at the SPE European formation damage conference, Scheveningen, The Netherlands. 27-29 May 2009. **SPE-122351-MS.** https://doi.org/10.2118/122351-MS.

Canada, Government of. Crude Oil Facts, 08/09/2019, https://www.nrcan.gc.ca/science-data/data-analysis/energy-data-analysis/energy-facts/crude-oil-facts/20064 (accessed 02/02/2020.

Cengel, Yunus A. and Cimbala, John M. 2006. *Fluid mechanics fundamentals and applications*. New York, NY: McGraw-Hill.

CFD-Online. 2020. Y plus wall distance estimation, https://www.cfd-online.com/Wiki/Y_plus_wall_distance_estimation (accessed 01/12/2020 2020).

Chinello, Gabriele, Ayati, Anis Awal, McGlinchey, Don et al. 2018. Comparison of Computational Fluid Dynamics Simulations and Experiments for Stratified Air-Water Flow in Pipes. *Journal of Fluids Engineering* **141**.

Chorin, Alexandre Joel. 1968. Numerical Solution of the Navier-Stokes Equations. *Mathematics of Computation* **22** (104): 745-762.

Desseault, Maurice B., a.s., Ormis, and El-Sayed, Samir. 2000. Heavy-oil production enhancement by encouraging sand production. Presented at the SPE/DOE Improved Oil Recovery Symposium, Tulsa Oklahoma. 3-5 April 2000. **SPE-59276-MS.** https://doi.org/10.2118/59276-MS.

Feszty, D. and Jakubik, T. *Grid Generation*: Computational Fluid Dynamics (Reprint).

Ghorai, Subhashini and Nigam, K.D.P. 2005. CFD Modeling of flow profiles and interfacial phenomena in two-phase flow in pipes. *Chemical Engineering and Processing* **45**: 55-65.

Guo, James C.Y. *Theoretical Fluid Mechanics Laminar Flow Velocity Profile* (Reprint).

Henshaw, William D. 1996. *Automatic Grid Generation* (Reprint).

Herreras, Nerea and Izarra, Jon. 2013. *Two-Phase pipeflow simulations with OpenFOAM*, Norwegian University of Science and Technology.

Hinze, J.O. 1975. *Turbulence*: McGraw-Hill.

Hulsurkar, Panav. 2017. *Experimental study of multiphase flow of viscous oil, gas and sand in horizontal pipes*. Master of Science, University of Alaska Fairbanks (March 2017).

Ikoku, Chi U. 1992. *Natural Gas Production Engineering*. Malabar, Florida: Krieger Publishing Company.

Jakobsen, Per Kristen. 2019. *An Introduction to Partial Differential Equations* (Reprint).

Jimenez, Maria-Alejandra and Chavez, Juan Carlos. 2009. Understanding the near-wellbore phenomena for hydraulically fractured wells: A comprehensive inflow performance numerical model. Presented at the SPE European formation damage conference, Scheveningen, The Netherlands. 27-29 May 2009. **SPE-122361-MS.** https://doi.org/10.2118/122361-MS.

Kalitzin, Georgi, Medic, Gorazd, Iaccarino, Gianluca et al. 2005. Near-wall behavior of RANS turbulence models and implications for wall functions. *Journal of Computational Physics* **204**: 265-291.

Karakas, Mentin and Tariq, S.M. 1991. Semianalytical Productivity Models for Perforated Completions. *SPE Production engineering* **6** (01): 73-82.

Li, L.J., Zhang, H., Davis, G.R. et al. 2005. Improving the closing characteristics of subsurface safety valve with combined FEA and CFD modeling/numerical analysis. Presented at the SPE Western regional meeting, Irvine CA, USA. 30 March - 1 April 2005. **SPE-93941-MS.** https://doi.org/10.2118/93941-MS.

Longfellow, Neil and Green, David. 2014. Computational fluid dynamics for horizontal well plunger lift system design. Presented at the SPE Western North America and Rocky Mountain joint regional meeting, Denver Colorado, USA. 16-18 April 2014. **SPE-169585-MS.** https://doi.org/10.2118/169585-MS.

M.O.R. 2020. Area of a Circular Segment given its height, https://www.mathopenref.com/segmentareaht.html (accessed 1/12/2020 2020).

Mathur, Bakul, Dandekar, Abhijit Y., Khataniar, Santanu et al. 2017. Life After CHOPS: Alaskan Heavy Oil Perspective. Presented at the SPE Western Regional Meeting, Bakersfield California, USA. 23 April 2017. **SPE-185704-MS.** https://doi.org/10.2118/185704-MS.

Meyer, Richard F. and Attanasi, Emil D. 2003. Heavy oil and natural bitumen -- strategic petroleum resources. *US Geological Survey* **Fact Sheet 70-03**.

Minish, Travis and Yule, David. 2012. Low production gains from CHOPS wells with extremely viscous oils. Presented at the SPE Heavy Oil Conference Canada, Calgary Alberta, Canada. 12-14 June 2012. **SPE-157913-MS.** https://doi.org/10.2118/157913-MS.

Molina, Oscar Mauricio. 2015. *Application of computational fluid dynamics to near-wellbore modeling of a gas well*. Master of Science, Louisiana State University and Agricultural and Mechanical College.

Moukalled, F., Mangani, L., and Darwish, M. 2016. *The Finite Volume Method in Computational Fluid Dynamics*, Vol. 113. Switzerland: Springer International Publishing.

Munson, Bruce R., Young, Donald F., Okiishi, Theodore H. et al. 2009. *Fundamentals of Fluid Mechanics*.

NEXTfoam. 2017. *Boundary Conditions - OpenFOAM-4.1* (Reprint).

Nichols, R. H. *Turbulence Models and Their Application to Complex Flows* (Reprint).

OPENFoam-Wiki. 2020. Contrib/groovyBC, http://openfoamwiki.net/index.php/Contrib/groovyBC (accessed 1/12/2020 2020).

Peters, Pim Thomas. 2016. *CFD of multiphase pipe flow: A Comparison of solvers*. Master of Science, Delft University of Technology.

Shoham, Ovadia. 2006. *Mechanistic modeling of gas-liquid two-phase flow in pipes*. Richardson, TX: Society of Petroleum Engineers

Shuard, Adrian M, Mahmud, Hisham B, and King, Andrew J. 2016. Comparison of Two-Phase Pipe Flow in OpenFOAM with a Mechanistic Model. Presented at the IOP Conference Series: Materials Science and Engineering. 2016https://doi.org/10.1088/1757-899X/121/1/012018.

Shuard, Adrian M, Mahmud, Hisham B, and King, Andrew J. 2018. Comparison of two-phase pipe flow in OpenFOAM with a mechanistic model. Presented at the IOP Conference series: Materials Science and Engineering

Sun, Datong, Li, Baoyan, Gladkikh, Mikhail et al. 2011. Comparison of skin factors for perforated completions calculated with computational-fluid-dynamics software and the Karakas-Tariq semianalytical model. Presented at the SPE European formation damage conference, Noordwijk, The Netherlands. 7-10 June 2011. **SPE-143663-MS.** https://doi.org/10.2118/143663-MS.

Tennekes, H. and Lumley, J. L. 1972. *A First Course in Turbulence*. Cambridge, Massachusetts: The MIT Press.

Theppornprapakorn, Viriyah. 2013. *Computational fluid dynamics flow comparison between openhole sleeve and plug-and-perf completion in a hydraulic fractured horizontal well*. Master of Science, Missouri University of Science and Technology.
Tocci, F., Bos, F., and Henkes, R. 2017. CFD for multiphase flow in vertical risers. *BHR Group*.
Tu, Jiyuan, Yeoh, Guan, and Liu, Chaoqun. 2013. *Computational Fluid Dynamics a Practical Approach*. Waltham, Ma: Butterworth-Heinemann.
Versteeg, H K and Malalasekera, W. 2007. *An Introduction to Computational Fluid Dynamics*. Essex, England: Pearson Education Limited.
Zhou, Y. and Shah, S.N. 2003. Fluid flow in coiled tubing: CFD simulation. Presented at the International petroleum conference, Calgary Alberta, Canada. 10-12 June 2003. **Paper-2003-212.**